UNIVERSITÀ
DEGLI STUDI
DI PADOVA

Head Office: Università degli Studi di Padova

Department of Geosciences

Ph.D. COURSE IN: EARTH SCIENCES
SERIES XXX

REACTIVATED FAULT ZONES: KINEMATIC COMPLEXITY AND FAULT ROCK SPECTRAL CHARACTERIZATION

Coordinator: Prof. Frabrizio Nestola
Supervisor: Prof. Dario Zampieri
Co-Supervisor: Prof. Matteo Massironi
Prof. Giulio di Toro

Ph.D. student: Anna Traforti

DIPARTIMENTO
DI GEOSCIENZE

UNIVERSITÀ
DEGLI STUDI
DI PADOVA

Reactivated Fault Zones: Kinematic Complexity and Fault Rock Spectral Characterization

Ph.D. Candidate:
Anna Traforti
Matricola 1107887

Thesis advisor:
Prof. Dario Zampieri
Thesis co-advisors:
Prof. Matteo Massironi
Prof. Giulio di Toro

Contents

Abstract

In the present work three main factors contributing to the overall complexity of reactivated fault zones have been investigated: i) the problematic reconstruction of polyphase brittle tectonic evolution accommodated by fault zones dissecting lithologically heterogeneous rock domains; ii) the estimate of the mechanical anisotropy associated with pre-existing planar discontinuities (i.e., metamorphic foliations and inherited faults) steering their brittle reactivation process; iii) the spectral characterization of fault zone rocks in complex fault architectures aimed at inferring the distribution of fault zone domains by means of remote sensing techniques.

In order to achieve the goal of improving current understanding of these factors defining reactivated fault zone complexity, different methodologies have been applied: i) a paleostress inversion analysis that carefully considers each analyzed fault zones and the different mechanical behavior of the lithological domains they deform; ii) a bootstrapping statistical approach aimed at evaluating the homogeneity between the resulting stress tensors and identifying possible local stress perturbations; iii) a normalised slip tendency analysis that, integrated with paleostress reconstructions and detailed meso- and micro-structural observations, allows constraining the mechanical properties of pre-existing planar discontinuities; iv) a spectral features analysis of fault zone rock reflectance spectra, aimed at highlighting the correlation between variations in fault rock spectral signatures and grain size reduction related to fault comminution processes.

The main results of this work highlighted that: i) polyphase brittle tectonics within lithologically heterogeneous rock domains can be efficiently unrevealed by applying a paleostress inversion combined with bootstrapping statistical analysis of the resulting reduced stress tensors; ii) normalised slip tendency analysis can be considered a reliable method to investigate and constrain the weakness of pre-existing anisotropies at a regional scale (10^4-10^3 m); iii) the grain size reduction resulting from fault-related comminution processes on mineralogically homogenous bedrocks (carbonates in this case) influences the spectral signatures of fault rock samples, which absorption feature parameters vary

systematically with the grain size in the VNIR and SWIR wavelength ranges; iv) consequently, remote sensing analysis, based on fault rock reflectance spectrum variabilities due to comminution processes, has a good potential in the identification of the spatial distribution and extent of fault core and damage zone domains (i.e., characterized by different grain sizes) on mineralogically homogenous bedrocks (carbonates in this case).

Sommario

Nel presente lavoro sono stati investigati tre fattori che contribuiscono alla definizione della complessità delle zone di faglia riattivate: i) la ricostruzione dell'evoluzione tettonica polifasica accomodata da zone di faglia che interessano litologie eterogenee; ii) la stima del grado di anisotropia meccanica associata alla presenza di discontinuità planari pre-esistenti (i.e., foliazioni metamorfiche e faglie), il quale influenza i meccanismi di riattivazione lungo tali piani; iii) la caratterizzazione spettrale delle rocce di faglia, finalizzata all' identificazione della distribuzione delle zone di danno e di core tramite tecniche di remote sensing, con particolare riguardo a zone di faglie mature aventi un'architettura complessa. Al fine di dare un nuovo contributo alla comprensione dei fattori che definiscono le complessità insite nelle zone di faglia riattivate, sono state applicate diverse metodologie che comprendono: i) l'inversione del campo di paleostress, applicata considerando il comportamento meccanico dei domini litologici interessati da ogni differente zona di faglia; ii) l'approccio statistico di tipo 'bootstrapping' applicato al fine di valutare l'omogeneità tra i tensori di stress ricavati e di identificare possibili perturbazioni locali del campo di paleostress; iii) la 'normalised slip tendensy analysis' che, integrata alla ricostruzione del campo di paleostress e ad una caratterizzazione di tipo micro- e meso-strutturale, permette di stimare quantitativamente le proprietà meccaniche di discontinuità planari pre-esistenti; iv) l'analisi delle bande di assorbimento osservate negli spettri di riflettenza di diverse rocce di faglia, al fine di evidenziare il rapporto esistente tra le variazioni osservate nei parametri spettrali e i processi di comminuzione dovuti all'evolversi della zona di faglia stessa.

I principali risultati di questo lavoro evidenziano come: i) tettoniche polifasiche che si sviluppano in domini rocciosi altamente eterogenei possono essere efficacemente ricostruite applicando in maniera integrata l'inversione del campo di paleostress e l'analisi statistica di tipo 'bootstrapping'; ii) la 'normalised slip tendency analysis' permette di investigare la debolezza di anisotropie pre-esistenti a scala regionale (10^4-10^3 m); iii) la riduzione granulometrica connessa ai processi di comminuzione dovuti all'evolversi di una zona di faglia in rocce incassanti omogenee dal punto di vista mineralogico (carbonati in

questo caso) influenza la firma spettrale delle rocce di faglia, le cui bande di assorbimento hanno caratteristiche che variano sistematicamente con la diminuzione della granulometria; iv) di conseguenza, l'analisi in remoto, basata sugli effetti della comminuzione sulle firme spettrali delle rocce di faglia, dimostra un buon potenziale nell'identificazione della distribuzione spaziale delle zone di danno e di core di una faglia in rocce incassanti omogenee dal punto di vista mineralogico.

1. Introduction

1.1 Overview

Most of the intracontinental deformation within the upper crust is accommodated by the reactivation of existing discontinuities rather than by the nucleation of new faults (e.g., Sibson 1985). Indeed, the majority of natural fault systems, once formed, tend to become zones of mechanical weakness that can easily accommodate later strain increments (e.g., Holdsworth et al., 1997; Rutter et al., 2001). The internal architecture of upper crustal faults, their rheological properties and the mechanisms that localize strain therein are the main factors characterizing the complexity of reactivated fault systems and are principally investigated because of their influence on seismogenesis (e.g., Rutter et al., 2001; Wibberley et al., 2008; Faulkner et al., 2010; Collettini, 2011; Fondriest et al., 2012; Smith et al., 2013).

This thesis is aimed at refining our understanding of how the following factors contribute to the overall complexity of reactivated fault systems.

i. Reactivated fault zones often show complicated and partially obliterated deformational histories. This makes the reconstruction of their brittle evolution particularly challenging (e.g., Viola et al., 2009, 2013; Torgensen et al., 2014).
ii. Several mechanisms are invoked to explain the strain localization along pre-existing faults and mechanical discontinuities. The assessment of the relative vs absolute weakness (e.g., Rice, 1992) of these structures is an important factor to account for the nucleation/reactivation of misoriented faults instead of Andersonian faults.
iii. Fault zones localizing several strain increments present a significant structural thickness (i.e., involving meter-thick cataclastic layers, Chambon et al., 2006) and usually bear complex fault zone architecture (e.g., Wibberley et al., 2008). This makes fault core and damage zone characterization difficult and time consuming.

The Chapters from 2 to 4 represent a collection of three original research papers focused on each of the above factors.

Chapter 2 (paper submitted to the *Journal of Structural Geology*) represents the first paleostress inversion analysis aimed at unraveling the evolution of the Sierras de Córdoba of central Argentina from the Early Triassic to the Present. The applied stress inversion procedure takes into account both the anisotropic and isotropic nature of the rocks outcropping in the area. A statistical and comparative analysis of the resulting stress tensors (i.e., bootstrapping method) is used to exclude the presence of significant local stress perturbations due to inherited anisotropies. Based on these results, we draw some conclusions on the importance of pervasive anisotropies in a region when aiming at stress inversion studies.

Chapter 3 (paper submitted to the *Journal of Structural Geology*) contains a detailed description of the brittle reactivation mechanisms that interested pre-existing planar discontinuities (i.e., metamorphic foliations and inherited faults) during the polyphase tectonic evolution of the Sierras de Córdoba (central Argentina). In particular, the mechanical strength of pre-existing discontinuities has been constrained by combining normalized slip tendency analysis (Lisle and Srivastava, 2004), paleostress analysis and meso- to microscale characterization of brittle failure modes observed in different phyllosilicate-bearing rocks.

Chapter 4 (paper to be submitted to *Remote Sensing* journal) represents a pioneering work aimed at investigating how the grain size reduction associated to fault zone development produces reflectance variations in rock and mineral spectral signatures, in order to assess the potential of remote sensing analysis in the identification of fault core and damage zone domains, with particular regards in defining complex fault zone architecture. The research needed to be focused on a well-studied mature fault zone affecting host rock bearing a simple and homogeneous composition. This condition ensures to evaluate the spectral signature variations solely due to fault-related comminution processes. In this regards, the Sierras de Córdoba of central Argentina do not represent a proper case study because the related mature fault zones, are not yet well-characterized, cross-cut highly polymineralic rocks and show enrichment in synkinematic authigenic clay

minerals (Bense et al., 2013a). For this purpose, we consider the Vado di Corno Fault Zone (Italian Central Apennines) representing a well-studied mature fault zone (Demurtas et al., 2016) affecting homogeneous carbonate rocks (basically composed by dolomite).

1.2 Theoretical background

1.2.1 Paleostress inversion unrevealing polyphase brittle evolution

The stress field causing slip on a fault plane can be constrained by means of stress inversion techniques (e.g., Angelier, 1979; Angelier, 1984; Etchecopar et al., 1981; Yamaji, 2000; Delvaux and Sperner, 2003; Zalohar and Vrabec, 2007; Lacombe, 2012), which require knowing the fault-slip data parameters. Fault plane orientation, slip direction and sense of movement are the parameters that are collectively referred to as "Fault-slip datum" (Marrett and Allmendinger, 1990) and the inversion of these kinematic data allows the reconstruction of a reduced stress tensor, which is defined by: the directions of principal stress axes σ1, σ2 and σ3 (maximum, intermediate and least compression, respectively) and the Stress Ratio defined as $R = (\sigma2 - \sigma3)/ (\sigma1 - \sigma3)$.

All fault-slip inversion methods developed in the past are based on a few, common theoretical assumptions (e.g., Lacombe, 2012 for a review):

1. Slip on a fault plane occurs along the direction of the maximum resolved shear stress (Wallace, 1951; Bott, 1959).
2. The faulted volume of rock is physically homogeneous and isotropic and, even if prefractured, it remains mechanically isotropic.
3. The rock volume affected by deformation behaves as a material with rheological linear stress-strain relationship.
4. The analyzed rock volume should be large compared to the dimension of the local faults, such that the stress imposed over this volume can be considered homogeneous for a given faulting event.
5. Slip on a given fault plane is independent from slip along other fault planes.

6. No block rotation occurs during or after the deformation.

Nevertheless, it should be noted how the above assumptions represent for some authors important oversimplifications introducing relevant uncertainties in the paleostress analysis (Twiss and Unruh, 1998; Marrett and Peacock, 1999; Pollard, 2000; Lacombe, 2012; Lacombe et al., 2013).

Stress inversion techniques based on these principles are either direct inversion methods using least square minimization (e.g., Angelier 1991; Sperner et al., 1993) or iterative algorithms. The latter test a wide range of possible tensors in order to search for the state of stress that explain a given fault-slip dataset by minimizing a specific misfit function (e.g., Angelier, 1979; Angelier, 1984; Etchecopar et al., 1981; Delvaux and Sperner, 2003). In most cases, the success of the iterative procedure is given by the fit of the theoretical slip vectors with those observed at the outcrop that is expressed as α misfit angle (i.e., acute angle between the resolved shear stress and the measured slip vector for an individual fault plane).

In the case of multiple and superimposed brittle deformational events the application of stress inversion techniques must be driven by careful criteria in order to overcome some possible shortcomings, such as the heterogeneous character of fault-slip datasets, the possible reactivation of even highly misoriented pre-existing structures and the related local reorientation of retrieved paleostress axes. The challenge in these scenarios is to gather sufficient fault-slip data identifying internally consistent fault and fracture subsets associated with distinct stress states. This can be done on the basis of field structural observations, geometric and kinematic compatibility, coating mineralogy of striated fault planes and chronologic data (Saintot et al., 2011; Viola et al., 2012; Mattila and Viola, 2014).

Existing stress inversion techniques have been successfully applied to decipher the past tectonic evolution in a wide range of geological frameworks. Nevertheless, the application of these methods to strongly anisotropic rocks (i.e., foliated metamorphic rocks and, secondly, sedimentary rocks characterized by pervasive bedding and fractures) is

complex and the influence of pre-existing weak anisotropies on later brittle faulting (e.g., Peacock et al.,1992; Crider, 2015) and on the possible local reorientation of related paleostress axes needs to be further investigated (e.g., Lacombe, 2012; Mattila and Viola, 2014); this especially in the framework of polyphase deformation histories reactivating the same pre-existing anisotropies (Tricart et al., 2004; Mehl et al., 2005; Viola et al., 2009, 2012; Saintot et al., 2011).

Chapter 2 is aimed at assessing these issues by developing a methodological workflow, wherein: i) paleostress inversion is carried out carefully considering the degree of anisotropy of the lithological domains deformed by the inverted fault-slip data and ii) the homogeneity of the resulting stress tensors is statistically evaluated.

1.2.2 Fault weakening mechanisms and mechanical anisotropy

The majority of natural faults can be considered zones of mechanical weakness that easily accommodate several strain increments interesting the upper crust (e.g., Sibson, 1985; Holdsworth et al., 1997). Faults can be defined 'weak' in a *relative sense*, if they are weaker than the surrounding crust (Rice, 1992), or in an *absolute sense*, such as faults characterized by highly weak material on the fault core, showing a lower resistance with respect to the standard brittle crust (i.e., empirical Byerlee law, Byerlee 1978; Rice, 1992). In addition, a fault can be defined optimally oriented, if its orientation coincides with the one expected for neo-formed faults developed under a given stress field (i.e., Andersonian faults according to the theory of faulting by Anderson, 1951); or 'misoriented' (e.g., Sibson, 1985), if it is characterized by an unfavorable tangential to normal stress ratio on the fault plane. Misoriented faults that undergo slip, even if unfavorably oriented with respect to the regional stress field, are relatively weak faults. Hence, slip along pre-existing misoriented faults imply a weakling mechanism, which can be related to: i) the presence of layers of extremely weak fault gouge, containing minerals with low friction coefficients (e.g. Moore and Rymer, 2007; Collettini et al., 2009; Smith and Faulkner, 2010); ii) the elevated fluid pressure within the fault zone (e.g. Rice, 1992; Byerlee, 1992; Axen and Selverstone, 1994;

Faulkner and Rutter, 2001; Collettini et al., 2006); iii) the rotation of principal stress axes that favor slip within the fault zone (e.g. Rice, 1992); iv) the mechanical anisotropy of foliated phyllosilicate-rich rocks (Massironi et al., 2011; Bistacchi et al., 2012; Bolognesi et al., 2016). The last mechanism would account also for the nucleation of misoriented faults instead of an Andersonian faults (Massironi et al., 2011; Bistacchi et al., 2012).

In chapter 3, this thesis refines the understanding of this weakening mechanism by presenting an analysis of the mechanical strength of pre-existing planar discontinuities in the Sierras de Cordoba basement rocks (central Argentina). In particular, the friction coefficients for slip along inherited discontinuities (i.e., metamorphic foliations and inherited faults) have been quantitatively investigated by using a modified slip tendency analysis (see Morris et al., 1996 for the original slip tendency analysis), which allows estimating if phyllosilicate-bearing rocks of the Sierras de Cordoba also account for an absolute weakness mechanism (i.e., failure along their inherited mechanical discontinuities develops at lower differential stresses than those required to reach the Andersonian faulting).

1.2.3 Fault zone architecture

Over the past 30 years, the established conceptual model for fault zone architecture involves three domains: (i) a fault core, where most of the displacement is accumulated; (ii) a damage zone, which represents a distributed zone of fractures and faulting surrounding the core and (iii) a protolith that might be characterized by deformation intensity not directly connected to the fault activity (Chester et al., 1993; Antonellini and Aydin, 1994, Caine et al., 1996; Childs et al., 2009; Agosta and Aydin, 2006; Wibberley et al., 2008; Faulkner et al., 2010).

Damage zones involve large volumes (up to 1km thick) at the margins of the fault zone and contain fractures (i.e., from microfractures to macrofractures, occasionally accommodating small shear offsets), which are relatively more frequent than in the protolith. In the damage zone the protolith fabric is not entirely obliterated, whereas

fracturing becomes more intense toward the fault core. The fault core refers to localized horizons (up to a several meters thick) of intense deformation, where much of the displacement is accumulated along a single or on multiple high-strain levels (e.g., Faulkner et al., 2010). The fault core is characterized by intense comminution processes producing fault rocks reduced at variable clast size: gouges, cataclasites–ultracataclasites and breccias (e.g., Sibson, 1977).

Within the fault core the grain size reduction can be associated with cataclasis, which involves the brittle fragmentation of mineral grains with rotation of grain fragments accompanied by frictional grain boundary sliding and dilatancy (e.g., Sibson, 1977). This kind of comminution along with pressure-solution and other mechanical and chemical processes obliterate the original fabric of the protolith. In addition fault cores can be interested by fault zone rock pulverization, which is typically characterized by a lack of shear strain and typically shows in situ “shatter” textures (Brune, 2001). Pulverized Fault Zone Rocks (PFZRs) display extremely fine grain size (i.e. ≤ 1 mm on average), exploded clasts with radial fracture pattern and preserved primary protolith features (Dor et al., 2006a, 2006b; Fondriest et al., 2015; Schröckenfuchs et al., 2015). The PFZRs are widely interpreted as the product of dynamic, high-strain rate deformation related to earthquake rupture propagation along large faults (Dor et al., 2006; Yuan et al., 2011).

Fault zone structure, described in terms of type, grain size and distribution of fault rocks, reflects the combination of several factors, such as: strain rate, magnitude of displacement, presence of fluids, confining pressure, temperature, and protolith characteristics (Tullis and Yund, 1980; Handy, 1989; Schmid and Handy, 1991; Faulkner et al., 2010). In particular, mature faults, which localized several strain increments, show fault zones of significant thickness bearing complex distribution of fault cores and of fault rocks (e.g., Chambon et al., 2006; Torgensen er al., 2014). In the past years, many efforts have been invested into the characterization of mature fault zones at various scale, with meso- to micro-scale detailed field analysis (Billi et al., 2003; Faulkner et al., 2003; Tesei et al., 2013; Fondriest et al. 2012; Demurtas et al., 2016), direct drilling of active fault zones at

seismogenic depth (e.g., San Andreas Fault Observatory at Depth - SAFOD) and reconstruction of 3D high-resolution models (e.g., Bistacchi et al., 2010).

Chapter 4 assesses the potential of a new method aimed at characterizing fault zone architecture on the basis of fault rock reflectance spectrum variabilities due to fault comminution processes. Knowing the correlation between the grain size reduction associated to fault zone development and the variations in fault rock spectral signatures might consistently enhance the potential of remote sensing applications for the analysis of distribution and extent of fault cores and damage zones of mature faults.

References

Agosta, F., Aydin, A., 2006. Architecture and deformation mechanism of a basin – bounding normal fault in Mesozoic platform carbonates, central Italy. Journal of Structural Geology 28 (2006) 1445–1467.

Anderson, E.M., 1905. The dynamics of faulting. Transactions of the Edinburgh Geological Society 8, 387–402, doi:10.1144/transed.8.3.387.

Angelier, J., 1979. Determination of the mean principal directions of stresses for a given fault population. Tectonophysics 56, T17–T26.

Angelier, J., 1984. Tectonic analysis of fault-slip data sets. Journal of Geophysical Research 89 (B7), 5835–5848.

Angelier, J., 1991. Inversion directe et recherche 4-D: comparaison physique et mathematique de deux methodes de determination des tenseurs des paleocon-traintes en tectonique de failles. Comptes Rendus de l'Academie des Sciences de Paris, 312(11), 1213-1218.

Antonellini, M., Aydin, A., 1994. Effect of faulting on fluid flow in porous sandstones: petrophysical properties. American Association of the Petroleum Geologists Bulletin 78, 355-377

Axen, G.J., Selverstone, J., 1994. Stress state and fluid-pressure level along the Whipple detachment fault, California. Geology 22, 835, doi:10.1130/0091-7613(1994)022<0835:SSAFPL>2.3.CO;2

Bense, F.A., Wemmer, K., Löbens, S., Siegesmund, S., 2013a. Fault gouge analyses: K–Ar illite dating, clay mineralogy and tectonic significance–a study from the Sierras Pampeanas, Argentina. International Journal of Earth Sciences 103, 189–218, doi:10.1007/s00531-013-0956-7

Billi, A., Salvini, F., Storti, F., 2003. The damage zone-fault core transition in carbonate rocks: implications for fault growth, structure and permeability. Journal of Structural Geology 25 (11), 1779–1794.

Bistacchi, A., Massironi, M., Menegon, L., 2010. Three-dimensional characterization of a crustal-scale fault zone: The Pusteria and Sprechenstein fault system (Eastern Alps). Journal of Structural Geology 32, 2022–2041, doi: 10.1016/j.jsg.2010.06.003

Bistacchi, A., Massironi, M., Menegon, L., Bolognesi, F., Donghi, V., 2012. On the nucleation of non-Andersonian faults along phyllosilicate-rich mylonite belts. Geological Society London Special Publications 367, 185–199, doi:10.1144/SP367.13

Bolognesi, F., Bistacchi, A., 2016. Weakness and mechanical anisotropy of phyllosilicate-rich cataclasites developed after mylonites of a low-angle normal fault (Simplon Line, Western Alps). Journal of Structural Geology 83, 1–12, doi:10.1016/j.jsg.2015.11.009

Bott, M.H.P., 1959. The mechanics of oblique slip faulting. Geological Magazine 96, 109–117.

Brune, J.N., 2001. Fault normal dynamic loading and unloading: an explanation for ‘‘non-gouge’’rock powder and lack of fault-parallel shear bands along the San Andreas fault. Eos Trans. American Geophysical Union 82 (47). Fall Meet. Suppl., Abstract S22B-0655.

Byerlee, J.D., 1978. Friction of rocks. Pure and Applied Geophysics PAGEOPH 116, 615–626. doi:10.1007/BF00876528

Byerlee, J.D., 1992. The change in orientation of subsidiary shears near faults con- taining pore fluid under high pressure. Tectonophysics 211, 295–303, doi:10.1016/0040-1951(92)90066-F.

Caine, J.S., Evans, J.P., Forster, C.B., 1996. Fault zone architecture and permeability structure. Geology 24, 1025–1028.

Chambon, G., Schmittbuhl, J., Corfdir, A., Orellana, N., Diraison, M., Géraud, Y., 2006. The thickness of faults: From laboratory experiments to field scale observations. Tectonophysics 426, 77–94, doi: 10.1016/j.tecto.2006.02.014

Chester, F.M., Evans, J.P., Biegel, R.L., 1993. Internal structure and weakening mechanisms of the San Andreas fault. Journal Geophysical Research 98, 771–786.

Childs, C., Manzocchi, T., Walsh, J.J., Bonson, C.G., Nicol, A., Schöpfer, M.P., 2009. A geometric model of fault zone and fault rock thickness variations. Journal of Structural Geology 31(2), 117–127.

Collettini, C., De Paola, N., Holdsworth, R.E., Barchi, M.R., 2006. The development and behaviour of low-angle normal faults during Cenozoic asymmetric exten- sion in the Northern Apennines, Italy. Journal of Structural Geology 28, 333–352, doi:10.1016/j.jsg.2005.10.003

Collettini, C., Niemeijer, A., Viti, C., Marone, C., 2009. Fault zone fabric and fault weakness. Nature 462, 907–911.

Collettini, C., Niemeijer, A., Viti, C., Smith, S.A.F., Marone, C., 2011. Fault structure, frictional properties and mixed-mode fault slip behavior. Earth and Planetary Science Letters 311, 316–327, doi:10.1016/j.epsl.2011.09.020.

Crider, J.G. 2015. The initiation of brittle faults in crystalline rock. Journal of Structural Geology 77, 159–174, doi: 10.1016/j.jsg.2015.05.001

Demurtas, M., Fondriest, M., Balsamo, F., Clemenzi, L., Storti, F., Bistacchi, A., Di Toro, G., 2016. Structure of a normal seismogenic fault zone in carbonates: The Vado di Corno Fault, Campo Imperatore, Central Apennines (Italy). Journal of Structural Geology, 90(August), 185–206, doi:10.1016/j.jsg.2016.08.004

Di Toro, G., Goldsby, D.L., Tullis, T.E., 2004. Friction falls towards zero in quartz rock as slip velocity approaches seismic rates. Nature 427, 436–439.

Delvaux, D., Sperner, B., 2003. New aspects of tectonic stress inversion with reference to the TENSOR program. In: Nieuwland, D.A. (ed.), New Insights into Structural Interpretation and Modelling. Geological Society of London, Special Publication 212, 75–100, doi:10.1144/GSL.SP.2003.212.01.06

Dor, O., Rockwell, T.K., Ben-Zion, Y., 2006a. Geological Observations of Damage Asymmetry in the Structure of the San Jacinto, San Andreas and Punchbowl Faults in Southern California: A Possible Indicator for Preferred Rupture Propagation Direction. Pure and Applied Geophysics, doi: 10.1007/s00024-005-0023-9

Dor, O., Ben-Zion, Y., Rockwell, T.K., Brune, J., 2006b. Pulverized rocks in the Mojave section of the San Andreas fault zone, Earth and Planetary Science Letters 245, 642–654.

Dor, O., Chester, J.S., Ben-Zion, Y., Brune, J.N., Rockwell, T.K., 2009. Damage characterization in sandstones along the Mojave section of the San Andreas fault with a new method: implications for the depth and mechanism of rock pulverization. Pure and Applied Geophysics 166 (10–11), 1747–1773.

Etchecopar, A., Vasseur, G., Daignieres, M., 1981. An inverse problem in micro- tectonics for the determination of stress tensors from fault striation analysis Journal of Structural Geology 3, 51–65.

Faulkner, D.R., Rutter, E.H., 2001. Can the maintenance of overpressured fluids in large strike-slip fault zones explain their apparent weakness? Geology 29, 503, doi:10.1130/0091-7613(2001)029<0503:CTMOOF>2.0.CO;2

Faulkner, D.R., Lewis, A.C., Rutter, E.H., 2003. On the internal structure and mechanics of large strike-slip fault zones: field observations of the Carboneras fault in southeastern Spain. Tectonophysics 367 (3), 235–251, doi:10.1016/S0040-1951(03)00134-3

Faulkner, D., Jackson, C., Lunn, R., Schlische, R., Shipton, Z., Wibberley, C., Withjack, M., 2010. A review of recent development concerning the structure, mechanics and fluid flow properties of fault zones. Journal of Structural Geology 32 (11), 1557–1575.

Fondriest, M., Smith, S.A.F., Di Toro, G., Zampieri, D., Mittempergher, S., 2012. Fault zone structure and seismic slip localization in dolostones, an example from the Southern Alps, Italy. Journal of Structural Geology 45, 52–67, doi:10.1016/j.jsg.2012.06.014

Fondriest, M., Aretusini, S., Di Toro, G., Smith, S.A.F., 2015. Fracturing and rock pulverization along an exhumed seismogenetic fault zone in dolostones: The Foiana Fault Zone (Southern Alps, Italy).Tectonophysics 654, 56–74.

Handy, M. R. (1989), Deformation regimes and the rheological evolution of fault zones in the lithosphere: The effects of pressure, temperature, grain size and time, Tectonophysics, 163, 119–152.

Holdsworth, R.E., van Diggelen, E.W.E., Spiers, C.J., de Bresser, J.H.P., Walker, R.J., Bowen, L., 2011. Fault rocks from the SAFOD core samples: Implications for weakening at shallow depths along the San Andreas Fault, California. Journal of Structural Geology 33, 132-144, doi: 10.1016/j.jsg.2010.11.010

Lacombe, O., 2012. Do fault slip data inversions actually yield “paleostresses” that can be compared with contemporary stresses? A critical discussion. Comptes Rendus Geoscience 344(3–4), 159–173, doi:10.1016/j.crte.2012.01.006

Lacombe, O., Jolivet, L., Le Pourhiet, L., Lecomte, E., Mehl, C., 2013. Initiation, geometry and mechanics of brittle faulting in exhuming metamorphic rocks: insights from the northern Cycladic islands (Aegean, Greece). Bulletin de la Société Géologique de France 184 (4–5), 383–403.

Lisle, R.J., Srivastava, D.C., 2004. Test of the frictional reactivation theory for faults and validity of fault-slip analysis. Geology 32, 569, doi:10.1130/ G20408.1.

Marrett, R.A., Allmendinger, R.W., 1990. Kinematic analysis of fault-slip data. Journal of Structural Geology 12, 973–986.

Marrett, R., Peacock, D.C.P., 1999. Strain and stress. Journal of Structural Geology 21, 1057–1063.

Massironi, M., Bistacchi, A., Menegon, L., 2011. Misoriented faults in exhumed metamorphic complexes : Rule or exception? Earth and Planetary Science Letters, 307(1–2), 233–239, doi:10.1016/j.epsl.2011.04.041

Mattila, J., Viola, G., 2014. New constraints on 1.7 Gyr of brittle tectonic evolution in southwestern Finland derived from a structural study at the site of a potential nuclear waste repository (Olkiluoto Island). Journal of Structural Geology 67, 50–74, doi:10.1016/j.jsg.2014.07.003

Mehl, C., Jolivet, L., Lacombe, O., 2005. From ductile to brittle: Evolution and localization of deformation below a crustal detachment (Tinos, Cyclades, Greece). Tectonics 24(4), 1–23, doi: 10.1029/2004TC001767

Moore, D.E., Rymer, M.J., 2007. Talc-bearing serpentinite and the creeping section of the San Andreas fault. Nature 448, 795–797, doi:10.1038/ nature06064.

Morris, A.P., Ferrill, D.A., Henderson, D.B., 1996. Slip-tendency analysis and fault reactivation. Geology 24, 275, doi:10.1130/0091-7613(1996)

Peacock, D.C.P., Sanderson, D.J., 1992. Effects of layering and anisotropy on fault geometry. Journal of the Geological Society, London 149(5), 793–802, doi: 10.1144/gsjgs.149.5.0793

Pollard, D.D., 2000. Strain and stress: discussion. Journal of Structural Geology 22, 1359–1367.

Rice, J.R., 1992. Fault stress states, pore pressure distributions, and the weakness of the San Andreas Fault. In: Wong, T. (Ed.), Fault Mechanics and Transport Properties of Rocks. Academic Press, San Diego 475–503.

Rutter, E.H., Holdsworth, R.E., Knipe, R.J., 2001. The nature and tectonic significance of fault-zone weakening: an introduction. In: Holdsworth, R.E., Strachan, R.A., Magloughlin, J.F., Knipe, R.J. (Eds.), The Nature and Tectonic Significance of Fault Zone Weakening. Geological Society, London, 1–11.

Saintot, A., Stephens, M.B., Viola, G., Nordgulen, Ø., 2011. Brittle tectonic evolution and paleostress field reconstruction in the southwestern part of the Fennoscandian Shield, Forsmark, Sweden. Tectonics 30, 1–36, doi:10.1029/2010TC002781

Schmid, S.M., Handy, M.R., 1991. Towards a genetic classification of fault rocks: Geological usage and tectonophysical implications. In: Mueller, D.W., McKenzie, J. A., Weissert, H. (Eds.), Controversies in Modern Geology: Evolution of Geological Theories in Sedimentology, Earth History and Tectonics. Academic, San Diego, California, 339–361.

Schröckenfuchs, T., Bauer, H., Grasemann, B., Decker, K., 2015. Rock pulverization and localization of a strike – slip fault zone in dolomite rocks (Salzach – Ennstal – Mariazelle – Puchberg fault, Austria).Journal of Structural Geology 78 (2015) 67–85.

Sibson, R., 1977. Fault rocks and fault mechanisms, Journal of the Geological Society, London 133, 191–213.

Smith, S.A.F., Faulkner, D.R., 2010. Laboratory measurements of the frictional properties of the Zuccale low-angle normal fault, Elba Island, Italy. Journal of Geophysical Research 115, B02407, doi:10.1029/2008JB006274

Smith, S.A.F., Bistacchi, A., Mitchell, T.M., Mittempergher, S., Di Toro, G., 2013. The structure of an exhumed intraplate seismogenic fault in crystalline basement. Tectonophysics 599, 29–44, doi:10.1016/j.tecto.2013.03.031

Sperner, B., Ratschbacher, L., Ott, R., 1993. Fault- Striae analysis: A Turbo-Pascal program package for graphical presentation and reduced stress tensor calcu- lation. Computer & Geosciences, 19(9), 1361–1388.

Tesei, T., Collettini, C., Viti, C., Barchi, M.R., 2013. Fault architecture and deformation mechanisms in exhumed analogues of seismogenic carbonate-bearing thrusts. Journal of Structural Geology 55, 167–181.

Torgersen, E., Viola, G., 2014. Structural and temporal evolution of a reactivated brittle-ductile fault - Part I: Fault architecture, strain localization mechanisms and deformation history: Earth and Planetary Science Letters 407, 205–220, doi: 10.1016/j.epsl.2014.09.019

Tricart, P., Schwartz, S., Sue, C., Lardeaux, J.M., 2004. Evidence of synextension tilting and doming during final exhumation from analysis of multistage faults (Queyras Schistes lustrés, Western Alps). Journal of Structural Geology 26(9), 1633–1645, doi: 10.1016/j.jsg.2004.02.002

Tullis, J., Yund, R.A., 1980. Hydrolytic weakening of experimentally deformed Westerly granite and Hale albite rock. Journal of Structural Geology 2, 439–451.

Twiss, R.J., Unruh, J.R., 1998. Analysis of fault slip inversions: do they constrain stress or strain rate? Journal of Geophysical Research 103, 12205–12222.

Viola, G., Venvik Ganerød, G., Wahlgren, C.-H., 2009. Unraveling 1.5 Ga of brittle deformation history in the Laxemar-Simpevarp area, southeast Sweden: A contribution to the Swedish site investigation study for the disposal of highly radioactive nuclear waste. Tectonics 28, TC5007, doi:10.1029/2009TC002461

Viola, G., Kounov, A., Andreoli, M.A.G., Mattila, J., 2012. Brittle tectonic evolution along the western margin of South Africa: More than 500Myr of continued reactivation. Tectonophysics 514–517, 93–114, doi:10.1016/j.tecto.2011.10.009

Viola, G., Zwingmann, H., Mattila, J., Kapyaho, A., 2013. K–Ar illite age constraints on the Proterozoic formation and reactivation history of a brittle fault in Fennoscandia. Terra Nova 25, 236–244, doi:10.1111/Ter.12031

Wallace, R.E. 1951. Geometry of shearing stress and relation to faulting. Journal of Geology 59, 118–130.

Wibberley, C.A., Yielding, G., Di Toro, G., 2008. Recent advances in the under- standing of fault zone internal structure: a review. Geological Society London Special Publications 299 (1), 5–33.

Yamaji, A., 2000. The multiple inverse method: a new technique to separate stresses from heterogeneous fault-slip data. Journal of Structural Geology 22, 441–452.

Yuan, F., Prakash, V., Tullis, T., 2011. Origin of pulverized rocks during earthquake fault rupture. Journal of Geophysical Research, 116, B06309, doi:10.1029/2010JB007721

Zalohar, J., Vrabec, M., 2007. Paleostress analysis of heterogeneous fault-slip data: the Gauss method. Journal of Structural Geology 29, 1798–1810.

2. Unravelling polyphase brittle deformation histories - Part I: A critical approach to paleostress inversion within lithologically heterogeneous domains: The example of the Sierras de Córdoba (Argentina)

A. Traforti[a*], D. Zampieri[a], M. Massironi[a], A. Bistacchi[b] and G. Viola[c]

[a] Dipartimento di Geoscienze, Università degli Studi di Padova, via Gradenigo, 6, 35131 Padova, Italy.

[b] Dipartimento di Scienze Geologiche e Geotecnologie, Università degli Studi di Milano Bicocca, Piazza della Scienza 4, 20126 Milano, Italy.

[c] Dipartimento di Scienze Biologiche, Geologiche ed Ambientali, Università degli Studi di Bologna, Via Zamboni 67, 40126 Bologna, Italy.

Abstract

The basement ranges of the Sierras de Córdoba of central Argentina (SDC) show compelling evidence of brittle deformation starting in the Early Carboniferous, with three deformational events. Each event caused significant reactivation of inherited structures and rheological anisotropies. We unraveled this regional polyphase brittle evolution by means of field structural analysis and paleostress inversion. The obtained reduced stress tensors constrain a conceptual evolutionary model that we integrate with published regional and geochronological constraints. The SDC contain both highly anisotropic basement rocks (phyllite and gneiss) and isotropic granite. Local potential stress perturbations have been assessed by means of a methodological workflow, wherein paleostress inversion was carried out carefully considering the degree of anisotropy of the lithological domains deformed by the inverted fault-slip data, and the homogeneity of the resulting stress tensors was statistically evaluated. The obtained stress tensors are generally homogeneous and representative of all the analyzed data, and constrain two Early Triassic to Early Cretaceous extensional episodes oriented NE and NW, followed by a compressional ENE paleostress field compatible with the present-day Andean convergence.

1 Introduction

The Sierras Pampeanas of central Argentina are an active thick-skinned belt that deforms the Andean foreland between 27° and 33° S (*Figure 2.1*). The uplift of this range is traditionally attributed to enhaned crustal shortening caused by the flat-slab subduction of the Nazca plate starting between 18 and 12 Ma ago (e.g., Jordan and Allmendinger, 1986; Kay and Abbruzzi, 1996; Ramos et al., 2002). According to this model, the Eastern Sierras Pampeanas (ESP) are the easternmost expression of crustal shortening in the central Andean foreland. The Sierras Pampeanas consist in turn of a series of north-south trending ranges located c. 700 km east of the Chilean trench (*Figure 2.1A*). More in detail, the ESP include the Sierras de San Luis to the southwest and the Sierras de Córdoba (SDC) to the northeast (*Figure 2.1B*). The SDC are the target of our study. They were characterized by volcanic activity (*Figure 2.1B*) during Miocene to Pleistocene times (Hiecke-Merlin and Piccoli, 1961; Gordillo and Linares, 1981; Kay and Gordillo, 1994; Ramos et al., 1991; Urbina et al., 1997; Kay and Mpodozis, 2002; Ramos et al., 2002), and are presently affected by neotectonic activity and active seismicity (Kraemer et al., 1993; Costa et al., 2000, 2001, 2014; Massabie et al., 2003; Alvarado et al., 2005a, 2005b; Richardson et al., 2012, 2013). Recently, some studies contributed to a better characterization of the uplift of the ranges by thermochronological investigations (zircon and apatite (UeTh)/He and apatite fission-track dating), which reveal that a positive topography existed in this region already before the Neogene (Bense et al., 2013b; Richardson et al., 2013). Punctuated episodes of brittle faulting therein are generally believed to span from the Early Carboniferous to present (e.g., Bense et al., 2013a). Each brittle deformation phase within this time span resulted in additional strain increments that were predominantly accommodated by the reactivation of inherited structures and rheological anisotropies (e.g., Ramos et al., 2002; Bense et al., 2013a; Marino et al., 2016), leading to a long history of structural reactivation.

The SDC were chosen for our study because they represent an excellent natural laboratory to investigate the polyphase brittle evolution of these ranges by means of paleostress inversion, due to the modest intensity of brittle deformation, especially during

the Andean compression (Bellahsen et al., 2016), and to the good number of outcropping faults affecting a variety of isotropic and anisotropic lithologies.

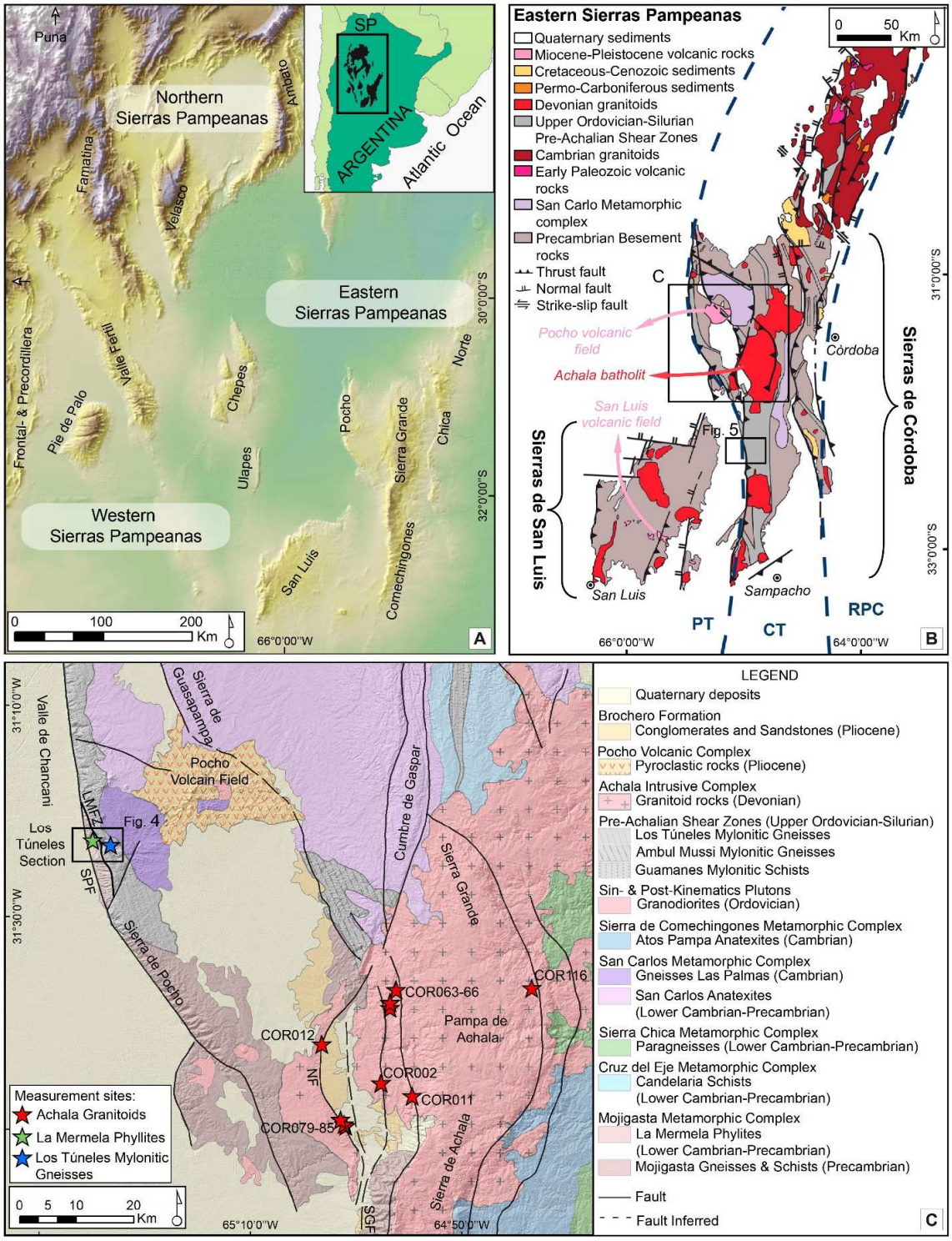

Figure 2.1: *(A) Shaded relief map of the Sierras Pampeanas showing the relative location of the Northern, Western and Eastern Sierras Pampeanas. Inset shows the location of the Sierras Pampeanas (SP) in Argentina. Labels indicate the main ranges. (B) General geological map of the Eastern Sierras Pampeans, modified from Martino (2003) and Richardson et al. (2013), with the internal geographic divisions of the area (black curly brackets). Blue dashed lines indicate the locations of terrane boundaries after Ramos et al. (2002), Rapela et al. (2007) and Richardson et al. (2013): Pampia Terrane (PT), Córdoba Terrane (CT) and Rio de la Plata Craton (RPC). Black squares outline the study area reported in (c) and the location of Merlo section (Figure 2.1). (C) Geological map of the Sierras de Córdoba based on Bonalumi et al. (1999), with major fault systems displayed: Sierra de Pocho fault (SPF), La Mermela fault zone (LMFZ), Sierra Grande fault (SGF) and Nono fault (NF).*

Existing stress inversion techniques have been extensively applied to decipher the past tectonic evolution in a wide range of geological frameworks. Nevertheless, the application of these methods to anisotropic rocks, such as foliated rocks, is complex and the influence of pervasive pre-existing weak anisotropies on later brittle faulting (e.g., Peacock et al.,1992; Crider, 2015) and on the possible local reorientation of related paleostress axes, needs to be further investigated (e.g., Lacombe, 2012; Mattila and Viola, 2014). This need becomes even more compelling if there is evidence pointing to several deformation events reactivating the same pre-existing anisotropies, which can make the reconstruction of paleostress tensors challenging (Tricart et al., 2004; Mehl et al., 2005; Viola et al., 2009, 2012; Saintot et al., 2011).

This is so because regional stress fields might be significantly perturbed at the local scale, thus generating second-order and greatly misaligned tensors, in response to, for example, extreme partitioning and localization on inherited structures and rheological anisotropies.

To further investigate these issues, we have therefore developed a methodological workflow, which allowed us to assess how homogeneous might be the stress field that is reconstructed from the inversion of data derived from rock domains characterized by a complex reactivation history. The proposed approach relies on the separate application of stress inversion procedures to the analyzed fault zones, carefully considering the different

mechanical behavior of the affected lithological units of the SDC (*Figure 2.1C*), and on the systematic comparison of the resulting tensors.

The mechanical aspects of brittle reactivation of pre-existing planar discontinuities such as metamorphic foliation planes and inherited faults are dealt with in detail through a Slip Tendency approach in the companion paper of this study (Traforti et al., Chapter 3).

1.1 Geological setting

1.1.1 Regional tectonic evolution

The ESP have accommodated a long deformation history. During the Early to Middle Paleozoic, a series of allochthonous and parautochthonous terranes (i.e., Pampean, Cuyania, and Chilenia terranes; *Figure 2.1B*) are believed to have been accreated onto the Rio de la Plata craton due to east-directed subduction along the western margin of Gondwana, resulting in a series of orogenies: the Cambrian Pampean cycle, the Ordovician-Silurian Famatinian cycle and the final Achalian cycle in the Devonian (e.g., Ramos et al., 1986, 2002; Ramos, 1988a, 1988b; Sims et al., 1998; Steenken et al., 2004).

Inter-terrane suture zones and intra-terrane shear zones formed during the Paleozoic orogenies strongly influenced the subsequent localization and geometry of faults associated with the Late Permian to Mesozoic extensional deformation events (e.g., Uliana et al., 1989; Schmidt et al., 1995; Ramos et al., 2002). The late Paleozoic deposition of non-marine strata has been connected to the formation of the intracratonic Paganzo basin (Salfity and Gorustovich, 1984), which was associated with orogenic collapse processes following the Early Paleozoic mountain building (Mpodozis and Ramos, 1990; Ramos et al., 2002). Subsequently, extensional deformation developed Triassic to Early Jurassic rift basins (e.g., Ramos and Kay, 1991; Ramos et al., 2002) leading to the formation of NNW-trending depocenters localized along the inherited terrane suture zones (i.e., Cuyo, Beazley, Las Salinas, Ischigualasto, and Marayes basins; for basin locations see *Figure 2.3* in Ramos et al. (2002)). A last phase of crustal extension occurred in the Early Cretaceous and is related to

the opening of the South Atlantic Ocean at these latitudes (Schmidt et al., 1995; Rossello and Mozetic, 1999). Major, narrow rift basins developed along the eastern and western borders of the Pampean terrane, e.g., along the western side of the Sierra Chica (Schmidt et al., 1995).

Andean deformation began in the Late Cretaceous with subduction of the Farallon Plate beneath the South American plate. Between 18 Ma and 12 Ma, subduction of the Juan Fernandez Ridge caused a flattening of the slab between 27° and 33° S (Ramos et al., 2002; Yañez et al., 2001), which resulted in a strong mechanical coupling between the subducting Nazca Plate and the upper South American Plate, and caused propagation toward the Andean foreland of Cenozoic magmatism (e.g., Pocho volcanic field) and crustal shortening. Consequently, the extensional fault systems of the ESP were reactivated and inverted during the Cenozoic Andean compression.

1.1.2 Geological setting of the Sierras de Córdoba (SDC)

The SDC are the easternmost range of the ESP and, from east to west, include the Sierra Norte, Sierra Chica, Sierra Grande, Sierra de Comechingones, and Sierra de Pocho (*Figure 2.1*). They comprise multiply deformed late Neoproterozoic to early Paleozoic metamorphic rocks, predominantly composed of large migmatitic bodies and Paleozoic granitoids, minor gneisses, amphibolites and marbles. High temperature moderate pressure metamorphism occurred during the continental collision between the Rio de la Plata craton and the Pampean terrane related to the Cambrian Pampean orogeny (e.g., Rapela et al., 1998b; Sims et al., 1998; Simpson et al., 2003) and was associated with the development of a highly penetrative east-dipping metamorphic foliation. At this time, pressure and temperature conditions reached granulite facies with widespread anatexis of basement rocks under conditions of 7–8 kb and 700–800 °C (e.g., San Carlos Metamorphic Complex in *Figure 2.1D* (Guereschi and Martino, 2014)). Low-grade rocks (i.e., La Mermela phyllite) crop out only locally in the western Sierra de Pocho, where they are overthrusted on Carboniferous-Permian continental sedimentary rocks (probably as a result of the

Andean compression). The Pampean orogeny was followed by the Ordovician-Silurian Famatinian cycle, during which the basement was deformed by east-dipping, greenschist-grade mylonitic to ultramilonitic shear zones referred to as Pre-Achalian Shear Zones that exploited the pre-existing penetrative metamorphic foliation (Martino, 2003; Simpson et al., 2003; Whitmeyer and Simpson, 2003). The shear zones (*Figure 2.1B* and *C*) were reactivated in Devonian-Carboniferous times (Martino, 2003; Steenken et al., 2010) during the Achalian orogeny, which was accompanied by the intrusion of Devonian granitoids (e.g., Achala batholith in *Figure 2.1C*, for which Dorais et al. (1997) provided U-Pb zircon intrusion age at 368 ± 2 Ma). By the Early Carboniferous, the tectono-metamorphic evolution and associated ductile deformation of the SDC had ceased (e.g., Whitmeyer, 2008; Bense et al., 2013a, 2013b). Subsequently the SDC underwent the Late Permian to Mesozoic extensional deformation with the development of important rift-related structures frequently reactiving the ductile anisotropies of the metamorphic basement. Cretaceous continental sedimentary rocks associated with the subsequent Early Cretaceous extension are preserved only in the Sierra Chica, where they are associated with dated basaltic flows and dykes (Stipanicic and Linares, 1975; Gordillo and Lencinas, 1967b).

The north-south trending ranges belonging to the SDC on their western flank are mostly bounded by east-dipping high-angle reverse faults (reactivating Mesozoic rift structures) and/or low-angle thrust faults. This results in an asymmetric range morphology (Jordan and Allmendinger, 1986; Ramos et al., 2002), with steeper western flanks and gentler eastern slopes (*Figure 2.1A*). From east to west, the Pampean elevation, Sierra Chica, Cumbre de Gaspar, Sierra Grande-Sierra de Comechingones, Nono, Ciénaga del Coro-La Sierrita, La Mermela and Pocho faults (e.g., Martino et al., 2016) are the master reverse faults that uplifted the basement in the Sierras de Córdoba. Between these major structures, Cumbre de Gaspar and Nono faults dip to the west. The Sierra Chica, Sierra de Comechingones and Nono faults show evidence of neotectonic activities affecting Late Cenozoic to Quaternary rocks (Costa et al., 2000, 2001, 2014). In fact, the intermountain valleys separating the SDC ranges are filled by Mesozoic to Late Cenozoic sedimentary rocks

and by younger Quaternary plain sediments. The Late Cenozoic to Quaternary continental sedimentation was connected to the Andean uplift pulse, which also accounts for the Neogene volcanic and pyroclastic activity producing the Pocho Volcanic Complex in the northwestern area (e.g., Kay and Gordillo, 1994).

2 Structural analysis and fault-slip data collection

Fault plane orientation, slip direction and sense of movement are the parameters that allow the full kinematic characterization of a brittle fault and are collectively referred to as "fault-slip datum" (Marrett and Allmendinger, 1990). Fault-slip data represent the input parameters to stress inversion (described in section 3), aimed to reconstruct the variation in time and space of the stress state.

During our mesostructural analysis, 285 fault-slip data were collected at 26 outcrops from along the major fault systems of the central and western Sierras de Córdoba, including the La Mermela, Sierra Grande and Nono faults (*Figure 2.1C*). Striations and small-scale frictional kinematic indicators, such as slickensides, grooves, steps, etc. (e.g., Petit, 1987; Doblas, 1998) reveal slip direction and slip sense on a fault plane, respectively. Fault kinematics were confirmed also through secondary shear (R, R', P) and tension (T) fractures (Tchalenko, 1970; Petit, 1987) whenever possible. In addition to fault-slip analysis, at each site mineral fault coating, fault plane size and gouge style were also systematically recorded to assist during sorting of the complex and heterogeneous fault-slip dataset.

In the following sections, a few key and representative field localities are described and discussed separately according to the dominant lithology. Indeed, the observed lithological domains demonstrate remarkable differences in the style of deformation, which we interpret as reflecting primarily the original mechanical anisotropy of the studied outcrops (i.e., Traforti et al., Chapter 3) linked to the foliated character of basement rocks versus the homogeneous nature of granites.

The field observations reported below were used to divide the measured fault and fracture dataset into internally consistent subsets associated with distinct stress states. The entire and unsorted field dataset measured at each outcrops, before data separation into internally consistent subsets, is reported in Appendix A (*Figure A.1*), along with the coordinates of all the measurement stations (*Table A.1*).

2.1 Achala granite

2.1.1 The Sierra Grande fault

123 fault-slip data were collected at four sites situated along the eastern and western margins of the Sierra Grande, which represents the central range of the SDC and affects the southern portion of the Achala batholith (*Figure 2.1C*). In particular, the western margin of this range is cut by the Sierra Grande fault, which is a major, N-striking tectonic lineament extending for more than 250 km and continuing to the south in the Sierra de Comechingones (*Figure 2.1*). The Sierra Grande fault is typically described as a high-angle reverse fault (dipping 45–55° to the east), which controlled the formation of a steep, 1800–2000 m high escarpment (e.g., Martino et al., 2016, Richardson et al., 2013). The latter is characterized by a series of parallel fault strands forming minor morphotectonic steps. Our mesostructural analysis along two of these morphotectonic scarps revealed two important ~ N-striking normal faults (*Figure 2.2*).

One of these extensional structures was studied in detail at the base of the Sierra Grande western scarp (1079 MASL) at site COR002. The main fault plane trends 196° (Right Hand Rule, RHR), dips 65° W and its core is between 4 to 5 m thick, consisting of highly brecciated granite intercalated with 10 to 20 cm thick clay gouge bands with red or white color (*Figure 2.2A*). Kinematic indicators (mainly slickenfibers) reveal the westward normal slip of the fault, as also confirmed by numerous secondary shear fractures (*Figure 2.2A* and *Figure 2.6A*). Striae on the fault planes display two different orientation clusters: the first is associated with a well-defined, top-to-the SW movement, whereas the second is

characterized by an overall top-to the-NW kinematics (*Figure 2.2A*). This suggests a probable activation of the fault plane during two distinct extensional phases.

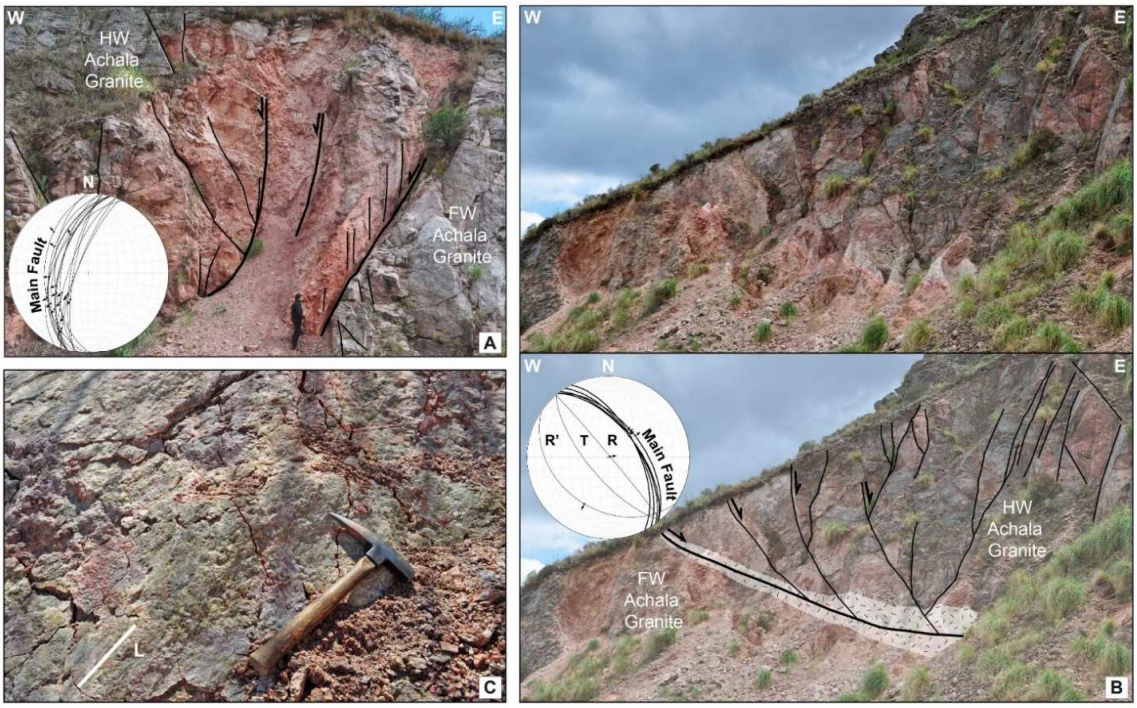

Figure 2.2: *Examples of meso-structural analysis of normal faults across the Sierra Grande western margins. (A) Normal fault zone outcropping at site COR002. (B) Normal fault measured at site COR011 and associated horsetail geometry. The shaded area represents the fault core. (C) Epidote, chlorite and quartz coating the normal fault planes.*

The second normal fault measured along the Sierra Grande western scarp trends 324° and dips 60° E (site COR011, 1432 MASL). The fault zone attains a maximum thickness of 7 m and contains brecciated and cataclastic granite with up to 10 cm thick clay red gouge bands. The mesoscopic fault structure reveals a typical horsetail geometry commonly associated with normal faults (*Figure 2.2B*), in accordance with the observed normal kinematics.

It is noteworthy that in both fault zones, numerous fractures and striated surfaces exhibit epidote, chlorite and quartz mineral coating (*Figure 2.2C*), which invariably

characterize all the extensional fault zones affecting the Achala granite. The mesostructural analysis along these two prominent faults does not reveal evidence of structural inversion due to the Andean compression (see the unsorted field dataset in *Figure A.1*, Appendix A). Hence, the main reverse fault (i.e., the Sierra Grande fault in the interpretation of Martino et al., (2016)), that was proposed for the uplift of the Sierra Grande range, is probably buried at the base of the escarpment and might result from the Neogene and Quaternary activity of E-dipping reverse faults inverting Mesozoic normal faults (i.e., similar to the example studied at site COR011).

In the following sections, we will refer to the structures measured along the western margin of the Sierra Grande (i.e., at sites COR002, COR011 and COR063-66) as the Western Sierra Grande fault zone, while the Eastern Sierra Grande fault zone is represented by the structures measured at site COR116.

2.1.2 The Nono fault

The southwestern portion of the Achala batholith is transected by the Nono fault, which has been described by Kraemer et al. (1993), Richardson et al. (2013) and Martino et al. (2016) as a well-exposed west-dipping thrust that superimposes the Devonian Achala batholith over Cenozoic fluvial sediments (Pliocene to late Pleistocene sandstone and late Pleistocene conglomerate). In map view, the Nono fault, which bounds the western margin of the Nono basin and defines a tens of meter high scarp, displays a curvilinear shape concave towards the east (*Figure 2.1C*). Meso-structural analysis along the Nono fault was carried out at two sites, COR012 and COR079-85, in the northern and southern sectors of the fault, respectively. An excellent fault exposure was analyzed along the river Los Saucetes (COR079-85, *Figure 2.3*), where the main thrust fault is defined by a 20 cm-thick brownish gouge with anastomosed structure. The fault zone trends 170°, dips 51° SW, and bears dip-slip striae (*Figure 2.3D*). The hanging-wall consists of highly brecciated granite whereas the footwall is formed by coarse sandstone with abundant carbonatic concretions.

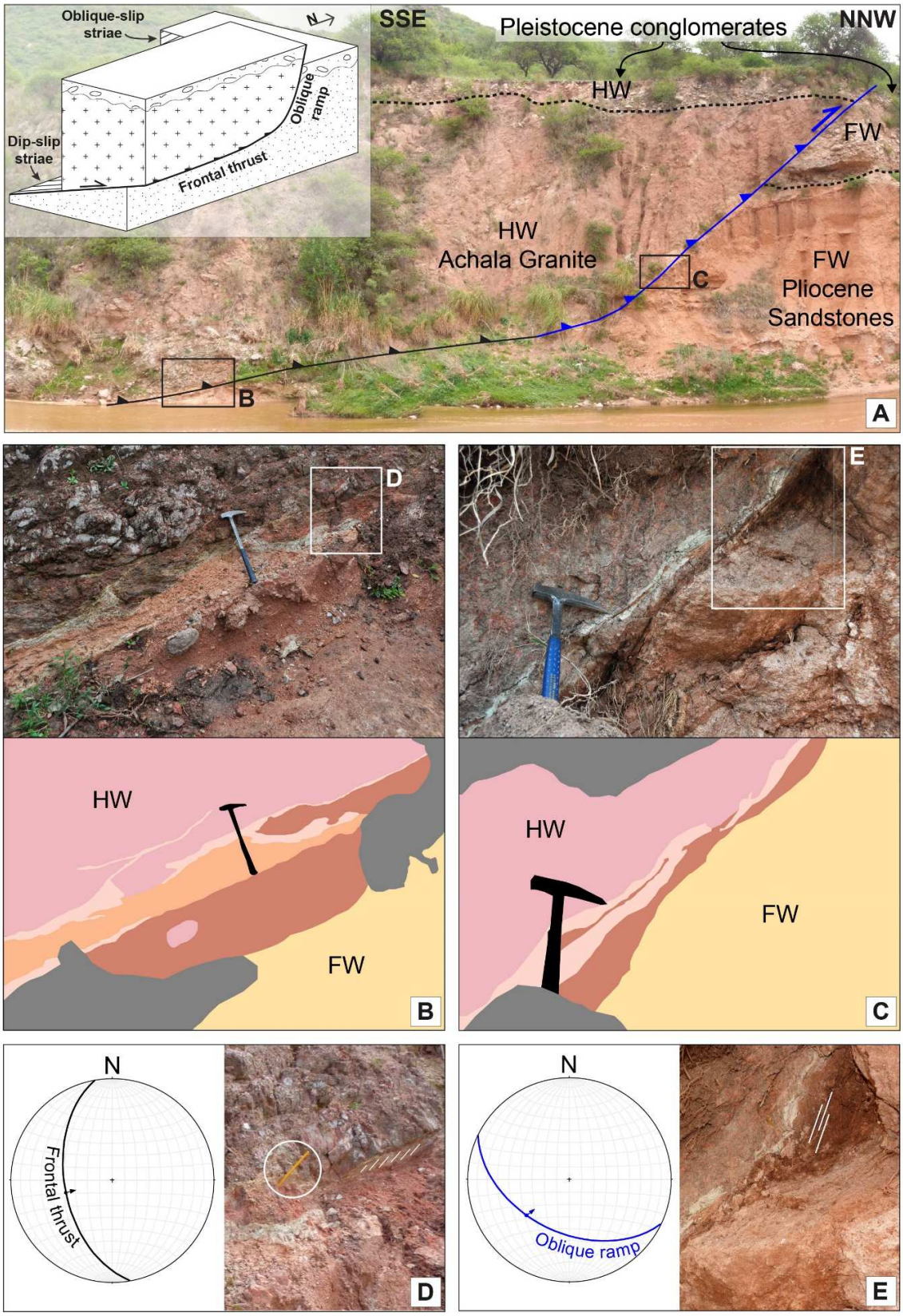
Oblique-slip striae
N
Dip-slip striae
Oblique ramp
Frontal thrust
SSE
Pleistocene conglomerates
NNW
HW
FW
HW
Achala Granite
C
FW
Pliocene
Sandstones
B
A
D
E
HW
FW
B
HW
FW
C
N
Frontal thrust
D
N
Oblique ramp
E

Figure 2.3: *Meso-structural analysis of the Nono fault. (A) Nono fault exposure along the river Los Saucetes (site COR079-85), with frontal thrust in black and oblique ramp in blue. Conceptual fault block diagram in the top left corner. (B, C) Upper pictures show details of the fault gouge associated to the frontal thrust (B) and to the oblique ramp (C), respectively, whereas the lower figures sketch the fault zone internal architecture with Achala granite in pink, Pliocene sandstones in yellow, fault core in beige, orange or okra according to the original gouge color and non-outcropping areas in grey. (D, E) Dip-slip and oblique slip striae characterizing the frontal thrust (D) and oblique ramp (E), respectively.*

To the north, the main thrust passes sideway into an oblique ramp. A grey to red 5 cm-thick gouge (*Figure 2.3C*) defines the ramp fault plane that trends 115° and dips 50° SW, bearing oblique sinistral striae (trend 231° and plunge 44°) compatible with the dip-slip reverse movement along the main fault.

The oblique thrust ramp defines the fault exposure shown in *Figure 2.3A*, which constrains two fault movements of late Pliocene and late Pleistocene-Holocene age on the basis of the displacements of Cenozoic formations (see Kraemer et al. (1993) for the description of Tertiary sequences).

Previous authors referred to this oblique ramp as to the main Nono fault (i.e., according to Richardson et al. (2013), the Nono fault trends 101° and dips 45° SW). However, thanks to our observations and structural analysis (*Figure 2.3*), we suggest to distinguish between a main fault (i.e., the true frontal thrust) and an oblique ramp (i.e., the fault which was previously interpreted by Richardson et al. (2013) as the main fault plain). Indeed, the trend of the oblique ramp is incompatible with the Nono fault trace in map view, which, in its southern sector, strikes NNW-SSE.

2.2 Los Túneles section

The northwestern margin of the SDC exposes a major reverse N-S trending fault zone, the “La Mermela fault zone”, which is associated with significant westward displacement accommodated by overall brittle-ductile deformation. The fault zone was studied at nineteen localities along the Los Túneles road cut, which provides easy access to excellent exposures (*Figure 2.4A*). In the Los Túneles area, Simpson et al. (2001, 2003) and Whitmeyer

and Simpson (2003) described this major, east-dipping reverse fault zone, which places the hanging wall sillimanite-grade Las Palmas gneiss in the east (Gordillo, 1984) over chlorite-facies phyllites of La Mermela to the west (Hünicken and Pensa, 1980). Those authors described this thrust zone as accommodating semi-brittle faulting, whereby the Las Palmas gneiss is retrogressed and transposed into a 2 km thick zone of west-directed shear bands, referred to as Los Túneles ductile shear zone by Martino (2003) and Los Túneles mylonitic gneiss by Bonalumi et al. (1999). Sheared rocks immediately above the fault contact with the underlying phyllites contain cm-scale pseudotachylyte veins that are younger than the shear bands and represent a semi-brittle reactivation of the ductile shear zone (Simpson et al., 2001). Pseudotachylite veins in Los Túneles gneiss were dated by Whitmeyer (2008) at 345 ± 5 Ma and 348 ± 2 Ma ($^{40}Ar/^{39}Ar$ laser ablation analysis on pseudotachylite).

Martino et al. (2016) described in the Los Túneles section a rejoining splay, in the terminology of Boyer and Elliot (1982), formed by two main thrust faults: (i) the Sierra de Pocho fault, which bounds the western flank of the Sierra de Pocho and juxtaposes Cambrian metamorphic rocks (i.e., La Mermela phyllite and mylonitic rocks of the Los Túneles shear zone) against Permian-Carboniferous sedimentary rocks, (ii) and the La Mermela fault zone, which thrusts the Las Palmas gneiss onto the La Mermela phyllites (*Figure 2.4A*). According to Martino et al. (2016), both faults are reverse faults and their main activity, which is characterized by brecciation and gouge development, is probably linked to the Cenozoic deformation that accommodated the uplift of the Sierras of Guasapampa and Pocho (*Figure 2.1C*).

2.2.1 La Mermela phyllites

The La Mermela phyllites represent an Early Cambrian (Late Neoproterozoic?) succession of low-grade metasedimentary rocks (Simpson et al., 2003), which might be associated with the accretionary prism of the destructive Early Cambrian margin of Gondwana. These rocks consist of chloritic phyllites characterized by solution cleavage, kink bands and small-scale chevron folds. Their mesostructural analysis was carried out at twelve

outcrops along the Los Túneles road cut (*Figure 2.4A*). As reported in Traforti et al. (Chapter 3), the phyllites are characterized by a sub-horizontal metamorphic foliation commonly cut by numerous fault planes (*Figure 2.4B*). The latter are characterized by tabular, decimetric cataclastic/brecciated bands, which are usually associated with centimeter to millimeter thick clay gouges. Two main conjugated fault sets strike NNW and NNE and dip steeply to moderately. Minor conjugated fault sets trending WNW and ENE are also present (see the unsorted field dataset in *Figure A.1*, Appendix A). The kinematics of these faults appear to be either direct or inverse (occasionally both kinematics characterize the same fault plane), and are indicated by clear kinematic indicators on the fault planes, secondary shear or tension fractures (*Figure 2.4B and E*) and drag folds deflecting the metamorphic foliation (*Figure 2.4C*). In some cases, the sub-horizontal foliation of the phyllites appears to be reactivated during brittle deformation, as revealed by the formation of centimeter to decimeter thick sub-horizontal cataclasite or breccia levels along the foliation planes (*Figure 2.4D and E*), showing reverse kinematics, similar to what reported by Bellahsen et al. (2016) in the Western Sierras Pampeanas.

2.2.2 Las Palmas gneiss and Los Túneles mylonitic gneiss

The Las Palmas gneiss is defined by a banded texture formed by Qtz–Pl–Bt–Grt–Sil–Kfs levels intercalated with veins of granitic composition (Qtz–Pl ± Grt ± Bt ± Kfs) in a biotitic matrix with Grt– Sil ± Pl ± Qtz (Siegesmund et al., 2010). Locally this texture is replaced by diatexites with garnet and cordierite (Gordillo, 1984). Towards the La Mermela fault zone, the high grade weakly sheared Las Palmas gneiss is retrogressed and transposed into a 2 km thick shear zone. The rocks associated with this shear zone are referred to as Los Túneles mylonitic gneiss (Bonalumi et al., 1999), which consists of coarse-grained augen gneiss deformed by mid- to upper-greenschist-grade protomylonites and mylonites. Mylonites become more common down section toward the tectonic contact with the underlying phyllites and are frequently overprinted by cataclasites and ultracataclasites. Protomylonites and mylonites reactivated during the later brittle episodes are characterized by decimeteric breccia bands, commonly interleaved with centimetric

cataclasite and gouge levels (*Figure 2.4F*). The analyzed faults develop either tabular cataclasite-breccia bands or anastomosed geometries associated with both ramp and flat segments (*Figures 2.4F and Figure 2.4G*). The Los Túneles mylonitic gneiss contains a rather consistent NNW trending gneissic foliation, with an average dip of 42° towards the northeast, and is affected by a main fault set striking NNW to NW, with a dip of ~ 40° towards the northeast (see the unsorted field dataset in *Figure A.1, Appendix A*). This proves that inherited ductile structures steered the localization of subsequent brittle deformation (Traforti et al., Chapter 3).

2.3 Merlo section

Our structural analysis also includes the Merlo section in the Sierra de Comechingones (*Figure 2.1* and *Figure 2.5*) despite the fact that it is geographically distant. The Merlo area (*Figure 2.5)* was studied to validate the results from the Los Túneles section. This Merlo area exposes the Tres Arboles fault zone (Whitmeyer and Simpson, 2003) that represents an important early Paleozoic ductile shear zone formed by amphibolite to upper greenschist facies mylonites and ultramylonites, which juxtapose sillimanite grade gneisses, migmatites and schists in the east against lower-grade biotite to chlorite grade phyllites in the west. As reported by Whitmeyer and Simpson, (2003) and Simpson et al. (2003), this structure might represent the southern and deepest termination of a major, terrane-bounding fault zone, which is exposed at shallower crustal level in the northernmost Los Túneles area. The analyzed brittle features and the measured fault slip data (see the unsorted field dataset in *Figure A.1*, Appendix A) are derived from the hanging wall of the Tres Arbores fault zone that consists of biotite + sillimanite + garnet ± cordierite schists and gneisses with large areas of interfingered migmatite (Whitmeyer and Simpson, 2003). The metamorphic foliation therein dips moderately to steeply toward the east (Simpson et al., 2003).The analyzed section in the Merlo area (*Figure 2.5*) is characterized by a N to NNE striking foliation, with an average dip of 30° towards the east, which appears to be reactivated, with both normal and reverse kinematics, or cut by well-developed NW-SE conjugate faults.

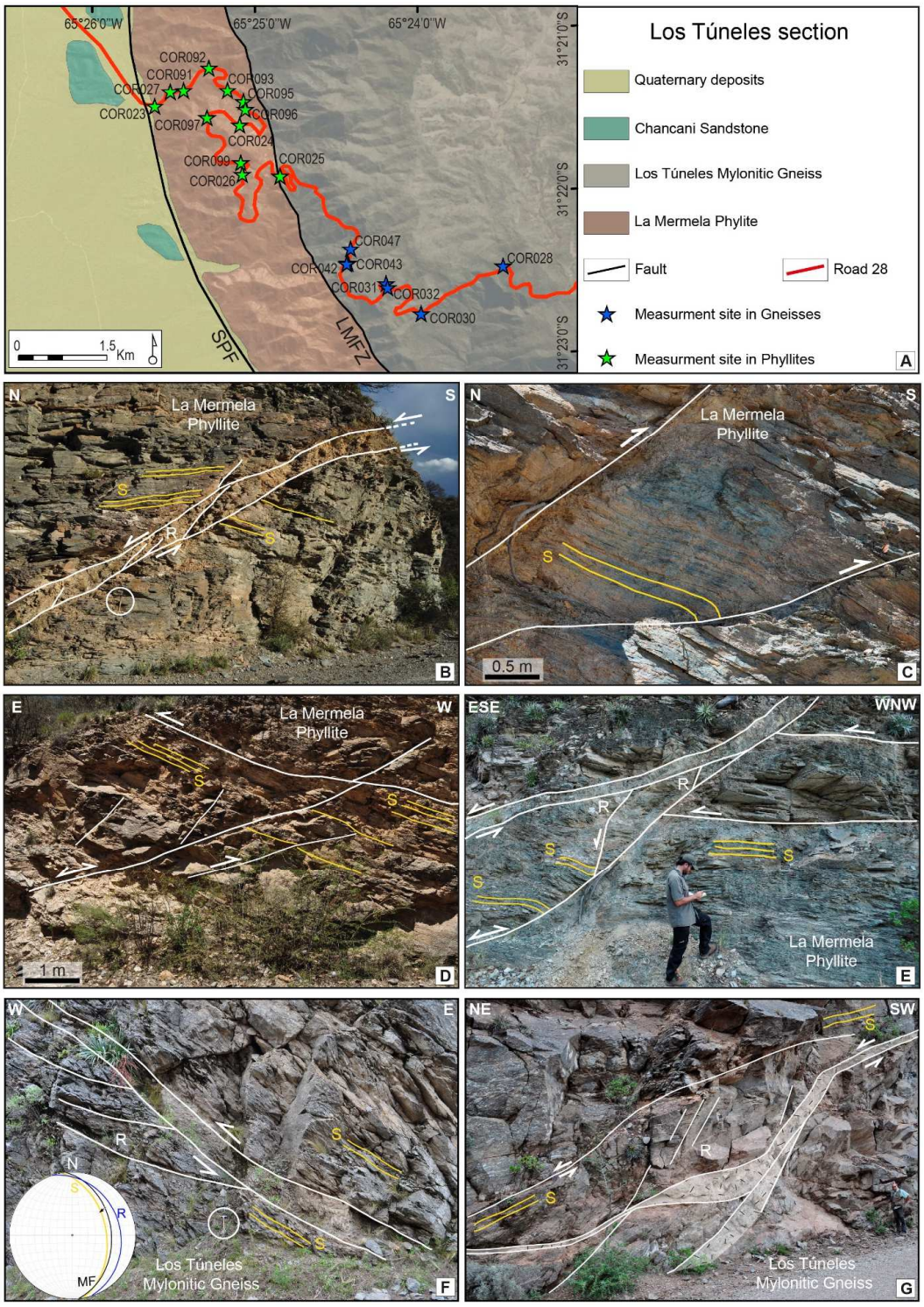
65°26'0"W
65°25'0"W
65°24'0"W
31°21'0"S
31°22'0"S
31°23'0"S
COR092
COR091
COR093
COR027
COR095
COR023
COR096
COR097
COR024
COR099
COR025
COR026
COR047
COR042
COR043
COR028
COR031
COR032
COR030
SPF
LMFZ
0
1,5 Km
Los Túneles section
Quaternary deposits
Chancani Sandstone
Los Túneles Mylonitic Gneiss
La Mermela Phylite
Fault
Road 28
Measurment site in Gneisses
Measurment site in Phyllites
A
N
S
La Mermela Phyllite
S
R
B
0.5 m
C
E
W
1 m
D
ESE
WNW
E
W
N
MF
Los Túneles Mylonitic Gneiss
F
NE
SW
G

Figure 2.4: *Examples of meso-structural analysis along the Los Túneles road cut. (A) Location of the nineteen studied sites. (B) Normal fault cutting sub-horizontal metamorphic foliation in the La Mermela phyllite and associated secondary shear fractures. (C) Drag fold deflecting the metamorphic foliation in the La Mermela phyllite. (D, E) Brittle thrust faults reactivating the sub-horizontal foliation of the La Mermela phyllite. (F) Thrust fault reactivating the mylonitic foliation in the Los Túneles mylonitic gneiss. (G) Anastomosed fault structure associated with ramp and flat fault morphology in the Los Túneles mylonitic*

3 Methods

3.1 Stress inversion from fault-slip data

The stress field causing slip on a fault plane can be constrained by means of stress inversion techniques, which require knowing the fault-slip data parameters. The inversion of these data allows the reconstruction of a reduced stress tensor, which is defined by: the directions of principal stress axes σ1, σ2 and σ3 (maximum, intermediate and least compression, respectively) and the Stress Ratio (R) calculated as the ratio of relative stress magnitudes (i.e., R = [σ2 - σ3]/[σ1 - σ3]). The reduced stress tensor, as defined above, will be hereafter referred to as “stress tensor” for simplicity.

All fault-slip inversion methods developed in the past are based on a few, common theoretical assumptions (e.g., Lacombe, 2012 for a review):

1. Slip on a fault plane occurs along the direction of the maximum resolved shear stress (Wallace, 1951; Bott, 1959).
2. The faulted volume of rock is physically homogeneous and isotropic and, even if prefractured, it remains mechanically isotropic.
3. The rock volume affected by deformation behaves as a rheologically linear material.
4. The analyzed rock volume should be large compared to the dimension of the local faults, such that the stress imposed over this volume can be considered homogeneous for a given faulting event.

5. Slip on a given fault plane is independent from slip along other fault planes.
6. No block rotation occurs during or after the deformation.

Stress inversion was performed using the Win_Tensor program (Delvaux, 2011), with which the best fitting stress tensor for a given fault-slip data set is computed following a two-step procedure (Delvaux and Sperner, 2003; Zain Eldeen et al., 2002): (i) Initial application of the Improved Right-Dihedron method, with which a first, suitable stress tensor is estimated; (ii) Subsequent iterative Rotational Optimization (Appendix A), during which the stress tensor derived by the Right- Dihedron method is tested and further refined by a 4D grid search involving successive rotations of the tensor around the three principal stress axes (σ_1, σ_2 and σ_3) together with the equivalent testing of the stress ratio R. Rotation around each stress axis is aimed at minimizing the value of a specific misfit function. The composite misfit function implemented in Win_Tensor tends to reduce the misfit angle α between the theoretically resolved shear stress and the measured slip, to minimize the normal stress and maximize the shear stress on faults (so as to favor slip) and to minimize the shear stress and normal stress magnitudes on extension fractures (to favor opening) (Delvaux and Sperner, 2003).

The quality of the resulting stress tensors reflects several factors, such as the number of input data, the type of data and the slip deviation. Win_Tensor produces two quality indexes, both ranging from A (best) to E (worst): QRw (World Stress Map quality rank) and QRt (Tensor Quality Rank); for a full description of the quality criteria we refer the reader to Delvaux and Sperner (2003).

The use of Win_Tensor allows efficient fault data separation when handling heterogeneous datasets (i.e., composed of structures that can be ascribed to more than one single slip event) and combined stress tensor determinations.

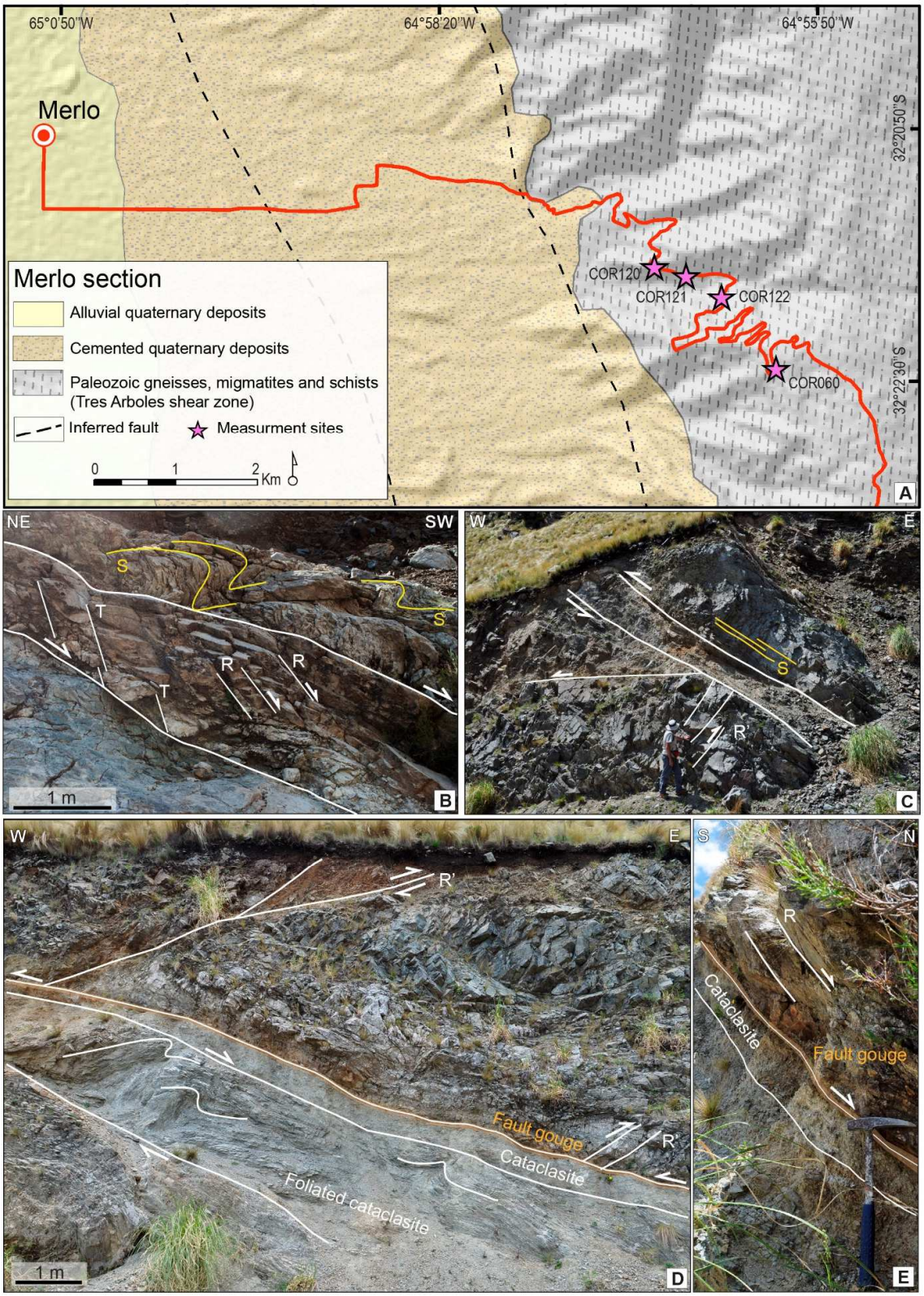
65°0'50"W
64°58'20"W
64°55'50"W
32°20'50"S
32°22'30"S
Merlo
COR120
COR121
COR122
COR060
Merlo section
Alluvial quaternary deposits
Cemented quaternary deposits
Paleozoic gneisses, migmatites and schists
(Tres Arboles shear zone)
Inferred fault
Measurment sites
0
1
2
Km
A
NE
SW
S
T
R
R
T
S
1 m
B
W
E
S
R'
C
W
E
R'
Fault gouge
Cataclasite
R'
Foliated cataclasite
1 m
D
S
N
R
Cataclasite
Fault gouge
E

Figure 2.5: *Examples of meso-structural analysis at the Merlo section. (A) Location of the studied sites. (B) Normal fault deflecting the metamorphic foliation and associated secondary shear fractures (R). (C) Reverse fault reactivating the metamorphic foliation and associated secondary shear fractures (R'). (D, E) Brittle fault characterized by a well-developed fault zone (foliated cataclasite, cataclasite and reddish fault gouge) showing both normal and reverse kinematics.*

This is done in an iterative way, wherein data separation into subset and stress tensor optimization for that subset are intimately related (Delvaux and Sperner, 2003). The first filtering of compatible fault-slip data is produced during the application of the Improved Right Dihedron method and is subsequently refined during the Rotational Optimization procedure. During the latter phase, fault-slip data that were found to be incompatible with the tested stress tensor (slip deviation $\alpha > 30°$) were assigned to different subsets or removed. Following the recommendations of Sperner and Zweigel (2010), fault data separation was manually checked based on field structural observations, geometric and kinematic compatibility criteria, coating mineralogy of striated fault planes and chronologic data, in order to produce internally consistent fault and fracture subsets associated with distinct stress states. This careful approach overcomes possible shortcomings, such as the heterogeneous character of fault-slip datasets and the possible reactivation of even highly misoriented pre-existing structures, which are frequent in the case of polyphase brittle tectonics affecting highly anisotropic basement rocks (i.e., the case of La Mermela phyllite and Los Túneles Mylonitic gneiss described in Traforti et al., Chapter 3). In these cases, the required mechanical isotropy of the faulted rock volume might be rarely met and the application of stress inversion techniques needs therefore to be carried out very carefully. Traforti et al. (Chapter 3) demonstrate how pre-existing planar discontinuities in the La Mermela phyllite and Los Túneles Mylonitic gneiss are absolute weak (sensu Rice, 1992) due to the low friction coefficient estimated for slip along foliation planes (c. 0.3-0.2) and pre-existing faults (c. 0.4) in these phyllosilicate-bearing rocks. As a matter of fact, fault zones affecting highly anisotropic basement rocks (i.e., La Mermela fault zone) are frequently localized along pre-existing mechanical weak anisotropies and carry evidence of multiple

fault activity producing wide damage zones where slip is preferentially partitioned along pre-existing foliation planes. The differences in the elastic properties of the damaged material with respect to the country rock can cause the local disturbance of the regional stress fields (e.g., stress rotation, Famin et al., 2014). Therefore, in order to assess possible local stress perturbations, paleostress inversion has been applied separately to fault-slip data from fault zones affecting different lithological domains (i.e., granites, phyllites and gneisses) and the resulting stress tensors have been systematically compared, and their homogeneity statistically evaluated, assuming that the individual lithological domains were subjected simultaneously to the same regional stress fields.

The final aim of our paleostress analysis was to reconstruct the sequence of brittle deformation events that has affected the study area. The obtained stress tensors were thus assigned to the different brittle deformation phases known to have affected the region according to geometric, mechanic and chronologic criteria. Similarly oriented paleostress tensors were associated with the same deformation event, while the value of the stress ratio was only subsequently taken into account, considering its high sensitivity to the slip dispersion of the data and its variability in space (e.g., Saintot et al., 2011). The brittle events reconstructed in this way can be considered of regional significance if defined by similar local stress tensors, which should be spatially well distributed over the whole area. In this study the stress regime associated with the calculated stress tensors is expressed numerically by the stress regime index R', defined in Delvaux et al. (1997). This index ranges from 0 to 3 and expresses a continuous progression from 0 (radial extension = flattening) to 3 (radial compression = constriction), assuming values of 0.5 for pure extension (R' = R, when σ_1 is vertical), 1.5 for pure strike-slip (R' = 2 – R, when σ_2 is vertical) and 2.5 for pure compression (R' = 2 + R, when σ_3 is vertical). Transtensive regimes correspond to R’ values between 0.75 and 1.25, while transpressive regimes to values between 1.75 and 2.25.

The paleostress inversion procedure discussed above was implemented on a merged dataset in the case of Los Túneles section, generated out of fault-slip data from sites that are geographically close and structurally related to the La Mermela fault zone (*Figure 2.4A*).

A similar approach was applied for the fault-slip data collected at the Tres Arboles fault zone. On the contrary, fault-slip data belonging to the Achala granite lithological domain were inverted site-by-site, reflecting the remarkably higher number of measurements at each location. Additionally, fault-slip data collected in the Achala granite were also inverted by a fault by fault approach (i.e., Nono fault, Eastern Sierra Grande fault zone, Western Sierra Grande fault zone, *Figure 2.6B*). Fault-slip data from several outcrops evenly distributed over large areas can potentially be merged into a single dataset to reconstruct regional paleostress fields (Gushtenko, 1975, 1979; Saintot et al., 2011). However, it is worth to note that the use of merged datasets is reliable only if the stress field can be considered homogeneous at the scale of the study area. Moreover, this approach may preclude the identification of potential stress perturbations related to local structural anisotropies (Saintot et al., 2011). To avoid this problem we merged only fault-slip data that are ascribable to clearly internally coherent sectors of the analyzed fault zones.

4 Results of the paleostress inversion

The obtained stress tensors are reported in terms of principal paleostress axis orientation and Stress Ratio value in *Figure 2.6* (full graphical results are available in Appendix A). Additionally, in order to assess the potential R' value variability for each phase, we compiled a diagram plotting the calculated stress regime index (R') against the corresponding tectonic phase (*Figure 2.7*).

4.1 Inversion of fault-slip data from Achala granite

Inversion of fault-slip data from the faulted Devonian Achala granite produced eleven stress tensors that were grouped into three distinct tectonic phases (*Figure 2.6A*). At this stage, we decided to include also tensors retrieved from only a limited number of data if they exhibited coherent kinematics with respect to the overall tectonic evolution (i.e., NE extensional phase for COR063-66).

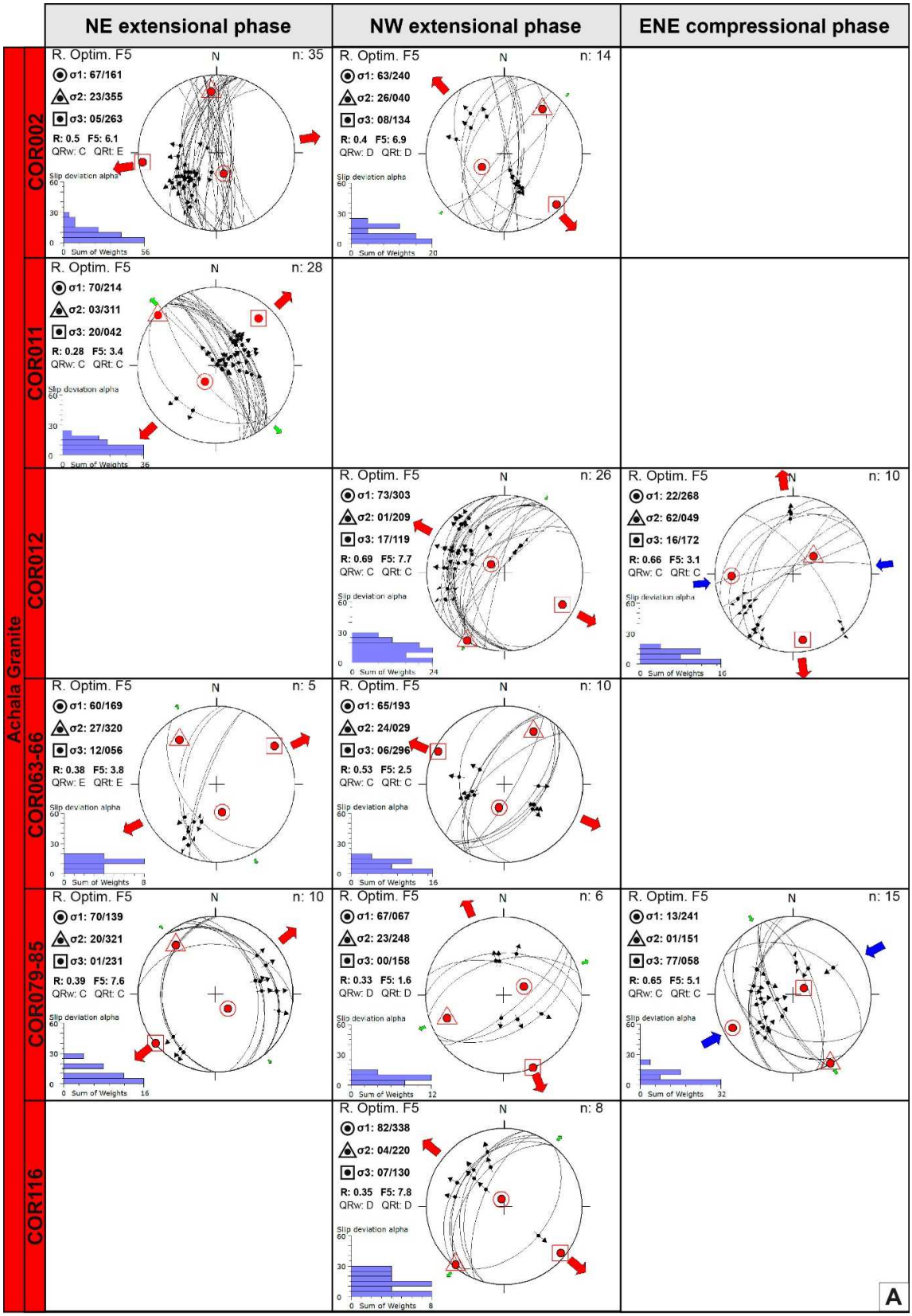
NE extensional phase
NW extensional phase
ENE compressional phase
Achala Granite
COR002
COR011
COR012
COR063-66
COR079-85
COR116
R. Optim. F5
N
n: 35
σ1: 67/161
σ2: 23/355
σ3: 05/263
R: 0.5 F5: 6.1
QRw: C QRt: E
Slip deviation alpha
Sum of Weights 56
n: 14
σ1: 63/240
σ2: 26/040
σ3: 08/134
R: 0.4 F5: 6.9
QRw: D QRt: D
Sum of Weights 20
n: 28
σ1: 70/214
σ2: 03/311
σ3: 20/042
R: 0.28 F5: 3.4
QRw: C QRt: C
Sum of Weights 36
n: 26
σ1: 73/303
σ2: 01/209
σ3: 17/119
R: 0.69 F5: 7.7
QRw: C QRt: C
Sum of Weights 24
n: 10
σ1: 22/268
σ2: 62/049
σ3: 16/172
R: 0.66 F5: 3.1
QRw: C QRt: C
Sum of Weights 16
n: 5
σ1: 60/169
σ2: 27/320
σ3: 12/056
R: 0.38 F5: 3.8
QRw: E QRt: E
Sum of Weights 8
n: 10
σ1: 65/193
σ2: 24/029
σ3: 06/296
R: 0.53 F5: 2.5
QRw: C QRt: C
Sum of Weights 16
n: 10
σ1: 70/139
σ2: 20/321
σ3: 01/231
R: 0.39 F5: 7.6
QRw: C QRt: C
Sum of Weights 16
n: 6
σ1: 67/067
σ2: 23/248
σ3: 00/158
R: 0.33 F5: 1.6
QRw: D QRt: D
Sum of Weights 12
n: 15
σ1: 13/241
σ2: 01/151
σ3: 77/058
R: 0.65 F5: 5.1
QRw: C QRt: C
Sum of Weights 32
n: 8
σ1: 82/338
σ2: 04/220
σ3: 07/130
R: 0.35 F5: 7.8
QRw: D QRt: D
Sum of Weights 8
A

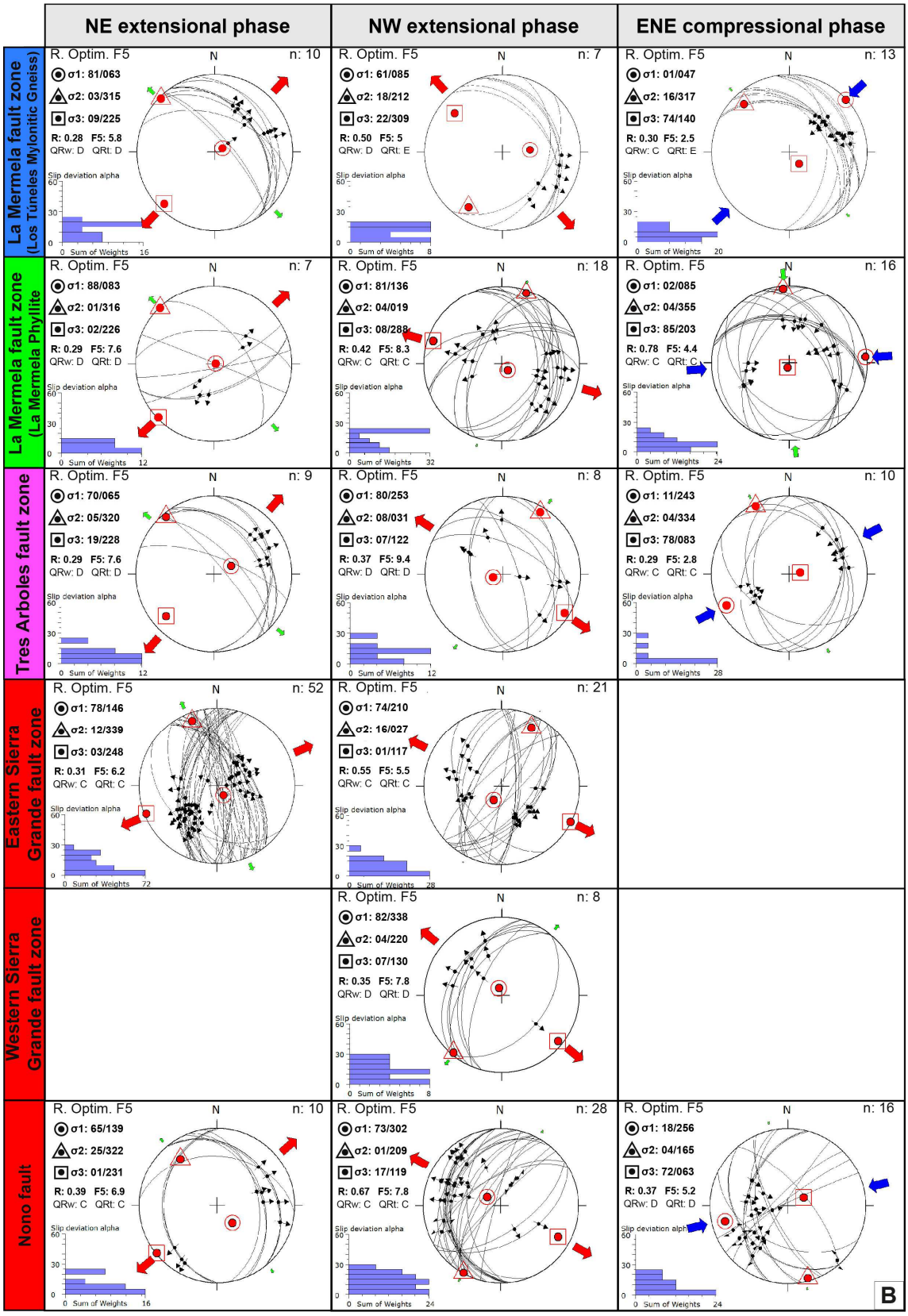
NE extensional phase
NW extensional phase
ENE compressional phase
La Mermela fault zone (Los Túneles Mylonitic Gneiss)
La Mermela fault zone (La Mermela Phyllite
Tres Arboles fault zone
Eastern Sierra Grande fault zone
Western Sierra Grande fault zone
Nono fault
R. Optim. F5
N
n: 10
σ1: 81/063
σ2: 03/315
σ3: 09/225
R: 0.28 F5: 5.8
QRw: D QRt: D
Slip deviation alpha
Sum of Weights
n: 7
σ1: 61/085
σ2: 18/212
σ3: 22/309
R: 0.50 F5: 5
QRw: D QRt: E
n: 13
σ1: 01/047
σ2: 16/317
σ3: 74/140
R: 0.30 F5: 2.5
QRw: C QRt: E
n: 7
σ1: 88/083
σ2: 01/316
σ3: 02/226
R: 0.29 F5: 7.6
QRw: D QRt: D
n: 18
σ1: 81/136
σ2: 04/019
σ3: 08/288
R: 0.42 F5: 8.3
QRw: C QRt: C
n: 16
σ1: 02/085
σ2: 04/355
σ3: 85/203
R: 0.78 F5: 4.4
QRw: C QRt: C
n: 9
σ1: 70/065
σ2: 05/320
σ3: 19/228
R: 0.29 F5: 7.6
QRw: D QRt: D
n: 8
σ1: 80/253
σ2: 08/031
σ3: 07/122
R: 0.37 F5: 9.4
QRw: D QRt: D
n: 10
σ1: 11/243
σ2: 04/334
σ3: 78/083
R: 0.29 F5: 2.8
QRw: C QRt: C
n: 52
σ1: 78/146
σ2: 12/339
σ3: 03/248
R: 0.31 F5: 6.2
QRw: C QRt: C
n: 21
σ1: 74/210
σ2: 16/027
σ3: 01/117
R: 0.55 F5: 5.5
QRw: C QRt: C
n: 8
σ1: 82/338
σ2: 04/220
σ3: 07/130
R: 0.35 F5: 7.8
QRw: D QRt: D
n: 10
σ1: 65/139
σ2: 25/322
σ3: 01/231
R: 0.39 F5: 6.9
QRw: C QRt: C
n: 28
σ1: 73/302
σ2: 01/209
σ3: 17/119
R: 0.67 F5: 7.8
QRw: C QRt: C
n: 16
σ1: 18/256
σ2: 04/165
σ3: 72/063
R: 0.37 F5: 5.2
QRw: D QRt: D
B

Figure 2.6: *Table with the results of paleostress inversion; each column identifies an individual tectonic event defined by tensors with similar principal stress axis orientations and similar stress ratio value. (A) Reduced stress tensors calculated site-by-site for the Achala Granite. (B) Reduced stress tensors calculated by inverting separately all fault-slip data belonging to the same fault zone: Nono fault, Eastern Sierra Grande fault zone and Western Sierra Grande fault zone for the Achala Granite (red), La Mermela fault zone affecting gneisses (blue) and phyllites (green), respectively, and Tres Arboles fault zone (purple).*

The stress tensors calculated from sites COR002, COR011, COR063-66 and COR079-85 (*Figure 2.6A*) were grouped to define a single extensional stress regime with a sub-horizontal σ_3 axis oriented NE/ENE. The individual stress tensors are mainly derived from the inversion of NW-SE conjugate, dip-slip normal faults in addition to W-dipping N-S to NNE-SSW normal faults with dip- to oblique-slip top-to-the SW kinematics and associated sub-vertical Riedel (R) and tension (T) fractures. The stress regime index (R') for the stress tensors associated to this first phase varies between about 0.5 and 0.3 (*Figure 2.6A*), indicating overall extensional conditions with some radial component. The inversion of fault-slip data from site COR002 constrains ENE-WSW-oriented extension, while the other stress tensors document a constant NE-SW σ_3. This should be ascribed to the fact that the stress tensor calculated at site COR002 is poorly constrained because derived from the inversion of fault-slip data with no variability in terms of strike. In fact, if we incorporate in a unique dataset all the data belonging to the Western Sierra Grande fault zone (i.e., COR002, COR011 and COR066-63, *Figure 2.1C*), the resulting stress tensor is better constrained by variably oriented fault sets (*Figure 2.6B*) and also shows a coherent NE-SW extension.

A second stress regime was identified by grouping five stress tensors from sites COR002, COR012, COR063-66, COR079-58 and COR116. It is characterized by a sub-horizontal NW/NNW σ_3 (*Figure 2.6A*). The R' value varies between 0.69 and 0.33, an indication of overall pure extension (*Figure 2.7*). The stress tensors defining this regime were based on the inversion of NE-SW and ENE-WSW conjugate dip-slip normal faults, W-

dipping N-S/NNE-SSW normal faults with oblique (top to the NE) movement and associated sub-vertical

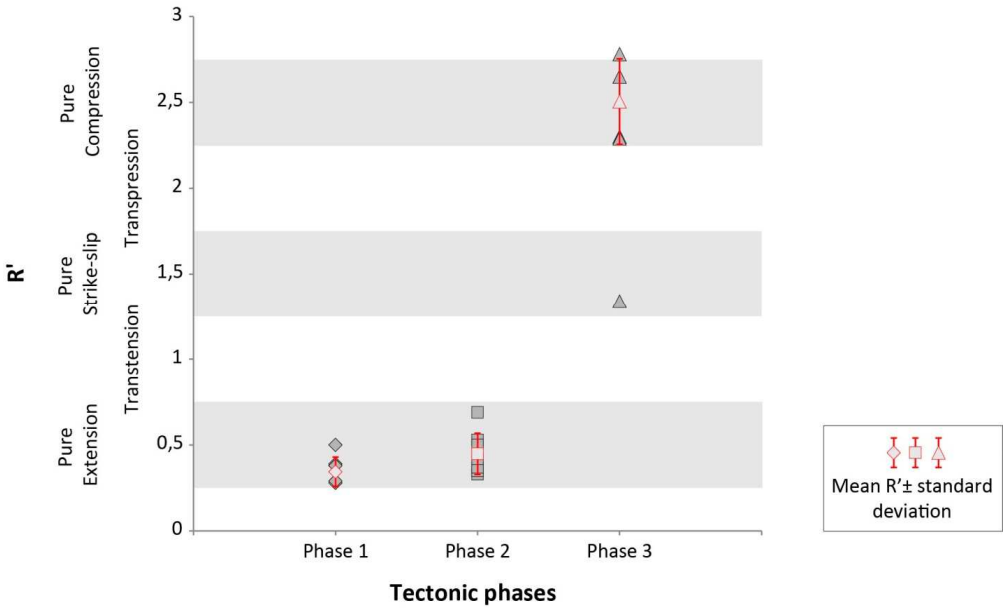

Figure 2.7: *R'value variability for each of the three brittle deformation phases reconstructed in this study.*

Riedel shear (R) and tension (T) fractures. This NW/NNW extensional phase is believed to postdate the NE-SW extension discussed above, as some tensional fractures associated with the first episode can be observed to be reactivated as shear fractures during NW/NNW extension (e.g., COR002, *Figure 2.6A*). σ_3 orientation appears to be stable for all solutions. Only the stress tensor calculated at site COR079-85 shows a NNW-SSE direction of extension, which might be reasonably considered as being affected by the limited available dataset. The importance of this tensor has been evaluated by applying paleostress inversion to a merged dataset containing all the data belonging to the Nono fault (i.e., COR012 and COR079-85, *Figure 2.1C*). Results (*Figure 2.6B*) show a NW-SE σ_3 axis orientation, which is coherent with the general direction of extension of the second tectonic phase in the Achala granite.

Finally, a compressional event is suggested by two stress tensors, which express a compressional and strike-slip regime (R' values of 2.65 and 1.34 respectively,*Figure 2.7)*, and were grouped to define a unique event as both are characterized by a sub-horizontal ENE-trending σ_1. The fault-slip data defining the compressional stress tensor were measured on NNW-SSE and NW-SE conjugate dip-slip reverse and thrust faults, some of which formed through reactivation of older normal faults. On the other hand, the strike-slip tensor was produced by the inversion of NE-SW oblique-slip reverse faults and NE-SW sub-vertical faults, originally generated as tension fractures (T) during the NW-SE extensional phase and then reactivated with a dextral strike-slip movement during a ENE compression (*Figure 2.6*). The compressional stress tensor can be associated with Neogene to Quaternary activity, as it is related to faults offsetting Pliocene to late Pleistocene sandstones and late Pleistocene conglomerates (site COR079-85, *Figure 2.3*). The strike-slip stress tensor, instead, cannot be constrained chronologically, but its genetic connection to Neogene compression is reasonable as it reactivates the NW/NNW extensional structures (*Figure 2.6A*). Given that these two tensors were generated from the same fault zone (i.e., the Nono fault, *Figure 2.1C*), to assess their compatibility we incorporated all the data in a unique dataset and run stress inversion. The resulting stress tensor (*Figure 2.6B*) shows an horizontal ENE-trending σ_1.

4.2 Inversion of fault-slip data from Los Túneles section

Paleostress analysis in Los Túneles section was carried out on eightytwo fault-slip data measured at nineteen different sites along the los Túneles road cut (*Figure 2.4A*). The stress inversion procedure was applied on merged datasets separately for Los Túneles mylonitic gneiss and La Mermela phyllite that represent respectively the hanging wall and footwall of the La Mermela fault zone.

In the case of Los Túneles section, no evidence of neotectonic activity have been observed and therefore no age constraints on recent brittle deformations can be provided

by stratigraphic cross-cutting relationships. Age constraints given by thermocronological data and K–Ar illite ages of fault gouges are described in section 5.2.

4.2.1 La Mermela phyllites

The paleostress inversion procedure applied to La Mermela fault-slip dataset produced three stress tensors (*Figure 2.6*).

An extensional stress regime with a sub-horizontal σ_3 axis striking WNW was constrained by inversion of NNE-SSW conjugate normal faults and NNW-dipping normal faults; both fault sets show an approximate dip-slip kinematics. The resulting stress regime index (R') value of 0.42 (R'= R ≈ 0.5) suggests a pure extensional regime.

In addition to this well constrained WNW extension, a stress tensor generated by the inversion of a small number of data accounts for a more radial extension (R'= R ≈ 0.3) with a sub-horizontal σ_3 axis striking NE-SW (*Figure 2.6B and Figure 2.7*). These extensional phases match the two extensional episode derived for the Achala granite, in terms of both stress axis orientation and R' values (*Figure 2.6 and Figure 2.7*).

The third tensor constrains a compressional regime characterized by a sub-horizontal ENE σ_1 and was derived from the inversion of NNE/NNW conjugate reverse dip-slip faults. A second set of NNW-dipping reverse faults, with top-to-the SSE kinematics, better constrains the tensor. Most of the inverted reverse faults dip moderately (40° to 60°) because they reactivated older normal faults. R' is 2.78, thus falling between a pure and a radial compressional regime (R' equal to 2.5 and 3 respectively). This R' value is slightly higher than the overall values retrieved for the compressional regime (*Figure 2.7*), possibly an effect of merging sites affected by local perturbation effects. This result should thus be treated with caution.

4.2.2 Los Túneles mylonitic gneiss

The stress tensors calculated during the inversion of Los Túneles mylonitic gneiss fault-slip dataset constrain three distinct tectonic phases, which fit the orientation of the three paleostress events reconstructed for the Achala granite and La Mermela phyllite.

A stress tensor, generated by the inversion of NE-dipping normal faults (*Figure 2.6B*), expresses an extensional stress regime with a sub-horizontal, NE-SW striking σ_3. The inverted NW-SE fault set is characterized by dip-slip, top-to-the NE kinematics. The R' value associated with this stress tensor is about 0.3, which indicates an extensional regime with some radial component.

The second tensor derives from the inversion of NE-dipping normal faults (representing the same fault set inverted to compute the first extensional tensor) with oblique (top-to-the SE) movement and SE-dipping, dip-slip normal faults. This tensor constrains an extensional stress regime with a NW-SE striking σ_3 plunging 22° towards NW, associated with an R' value of 0.5.

Finally, a compressional paleostress event with a sub-horizontal NE σ_1 is determined by the inversion of NE-dipping thrust faults (top-to-the SW) and E-dipping thrusts and reverse faults with top-to-the WSW kinematics. In this case, R' is 2.30, which reflects a compressive regime with a transpressive component.

It is noteworthy that the low quality (QRt = E) of the computed stress tensors likely reflects the low dispersion of the data in orientation (*Figure 2.6*). This condition is due to the pervasive reactivation of the ductile foliation during the brittle deformation of Los Túneles mylonitic gneiss, which steered brittle localization thus preventing the formation of fault sets with more varied planar attitudes.

4.3 Inversion of fault-slip data from Merlo section

The paleostress inversion procedure applied to the fifty-six fault-slip data measured in the Merlo area produced three stress tensors that corroborate the results from the Los Túneles section.

An extensional stress tensor with a sub-horizontal σ_3 striking NE-SW was generated by the inversion of NE-dipping normal faults and associated T fractures (*Figure 2.6B*) and N-S trending east-dipping normal faults representing the brittly reactivated foliation. The R' value associated with this stress tensor is about 0.3, perfectly coherent with the values obtained for this phase in the Los Túneles area (*Figure 2.7*).

The second tensor, which constrains an extensional stress regime (R' value of about 0.4) with a NW-SE striking sub-horizontal σ_3, derives from the inversion of the NE-dipping normal faults, reactivated with oblique (top-to-the NW) movement, and ~ NS trending conjugate normal faults that represent the east-dipping reactivated metamorphic foliation.

A stress tensor with a sub-horizontal ENE σ_1 constrains the compressional event. It is obtained from the inversion of two main conjugated reverse fault sets striking NW and N/NNE. The obtained R' value is 2.3, which expresses a transpressive events, in accordance to the Los Túneles area results (i.e., Los Túneles mylonitic gneiss, *Figure 2.7*).

4.4 Statistic analysis of the reduced stress tensors

In this study a paleostress inversion procedure is applied to mechanically anisotropic basement rocks and isotropic granitic bodies in different locations (*Figure 2.1*). Stress inversion results are summarized in *Figure 2.8A*, where the considered stress tensors (i.e., tensors computed for each fault zone affecting the different lithological domains) are plotted according to the tectonic phase. The stress inversion results show some differences both in terms of principal axis orientations and stress ratio R. We might wonder whether these differences should be taken as an indication of a true heterogeneity in the regional

stress field, due to some tectonic-mechanical process, or if the differences are not statistically significative and are just due to random errors.

For this purpose we have calculated the mean value and dispersion of all the stress parameters with a *bootstrap* approach (e.g., Borradaile 2003). The bootstrap method is a non-parametric approach (i.e. it does not rely on asumptions about the underlying statistics) that uses a random number generator to repeatedly resample the original data (using the "*sampling with replacement"* method, Borradaile 2003) in order to create a large *pseudo*-data sample drawn from the original dataset, that is meant to yield reliable confidence estimates for the mean values. In this work the bootstrapping procedure has been applied to calculate the mean reduced stress tensor for the three main deformation events and the associated 95% confidence intervals for each stress axis orientation and the stress ratio value. In *Figure 2.8B* the calculated 95% confidence intervals are expressed as bounding values (extreme values that are not exceded with a 95% probability) and as delta (differences between the mean value and the confidence interval bounding values), which vary on average between 4.5° and 8.5° in most cases, with the exception of trends of sub-vertical stress axes, that are highly variable due to their nearly vertical dip angle. Deltas for stress ratio R vary between 0.01 and 0,14.

Since these values are generally small, we infer that no significant stress heterogeneities can be demonstrated in most cases, and we assume that the regional stress tensor at the time of deformation was generally homogeneous. The only case where some heterogeneity might be envisaged, is that of the Los Túneles mylonitic gneiss during NE-SW extension and ENE-WSW compression (second and third deformation events). The higer level of heterogeneities of these tensor most likely reflects the independently documented pervasive reactivation of the mylonitic foliation (Traforti et al., Chapter 3). The proposed explanations for stress perturbations around faults include low-friction fault materials (e.g., Lockner et al., 2011), dynamic mechanisms of friction reduction during earthquakes (e.g., Di Toro et al., 2004), or pore fluid pressures greater than hydrostatic in the fault zone before an earthquake (e.g., Rice, 1992). Since the Los Túneles shear zone does not display pervasive

veining or evidence for hydraulic fracturing, and no evidence of Mesozoic-Cenozoic paleo-earthquakes have been found to date (i.e., pseudotachylites), a low friction coefficient associated with the activation of the inherited mica-rich foliation planes (Traforti et al., Chapter 3) seems to be the most reasonable explanation in this case. Neverthless, the results of the bootstrapping procedure defined how the possible heterogeneous character of the stress tensors obtained from the Los Túneles mylonitic gneiss (in particular for second and third deformation events) do not significantly affect the overall consistency of stress inversion procedure among the different lithological domains.

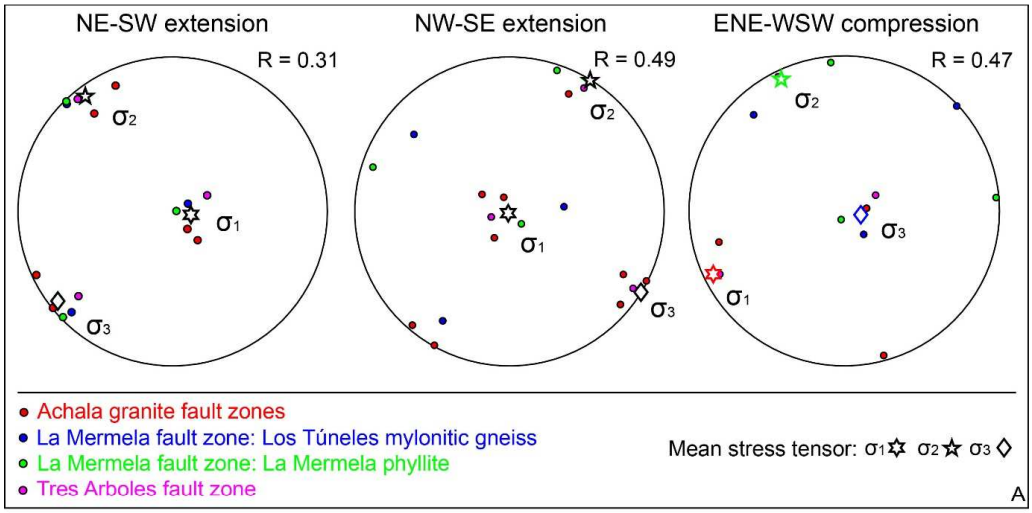

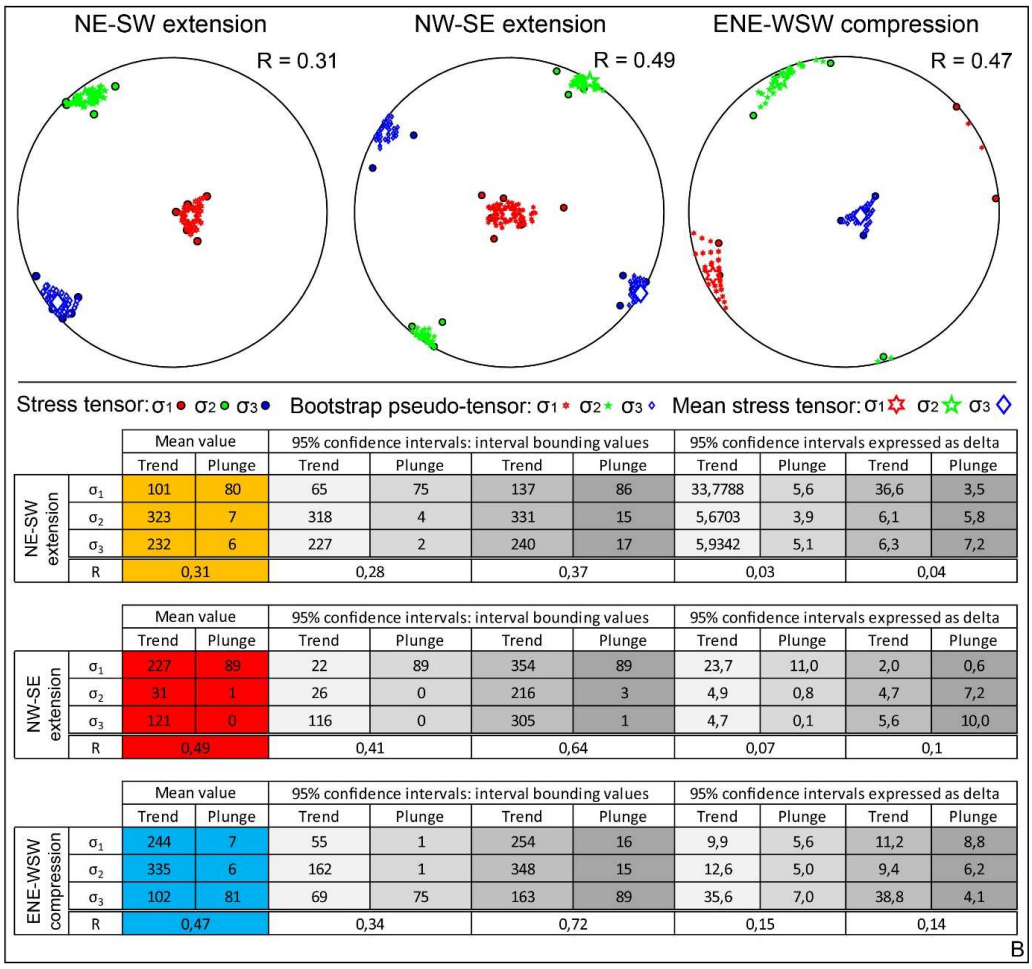

		Mean value		95% confidence intervals: interval bounding values				95% confidence intervals expressed as delta			
		Trend	Plunge	Trend	Plunge	Trend	Plunge	Trend	Plunge	Trend	Plunge
NE-SW extension	σ_1	101	80	65	75	137	86	33,7788	5,6	36,6	3,5
	σ_2	323	7	318	4	331	15	5,6703	3,9	6,1	5,8
	σ_3	232	6	227	2	240	17	5,9342	5,1	6,3	7,2
	R	0,31		0,28		0,37		0,03		0,04	

		Mean value		95% confidence intervals: interval bounding values				95% confidence intervals expressed as delta			
		Trend	Plunge	Trend	Plunge	Trend	Plunge	Trend	Plunge	Trend	Plunge
NW-SE extension	σ_1	227	89	22	89	354	89	23,7	11,0	2,0	0,6
	σ_2	31	1	26	0	216	3	4,9	0,8	4,7	7,2
	σ_3	121	0	116	0	305	1	4,7	0,1	5,6	10,0
	R	0,49		0,41		0,64		0,07		0,1	

		Mean value		95% confidence intervals: interval bounding values				95% confidence intervals expressed as delta			
		Trend	Plunge	Trend	Plunge	Trend	Plunge	Trend	Plunge	Trend	Plunge
ENE-WSW compression	σ_1	244	7	55	1	254	16	9,9	5,6	11,2	8,8
	σ_2	335	6	162	1	348	15	12,6	5,0	9,4	6,2
	σ_3	102	81	69	75	163	89	35,6	7,0	38,8	4,1
	R	0,47		0,34		0,72		0,15		0,14	

Figure 2.8: *(A) Visual comparative analysis applied separately to each tectonic phase considering the stress tensors computed for the analysed fault zones affecting different*

lithological domains. (B) Results of bootstrapping procedure reported as strereoplots and in table form. For each tectonic phase, the stereoplots report: the initial stress tensors, the mean stress tensors resulting from the boostrapping procedure and the bootstrap pseudo-tensors that allow estimating the 95% confidence interval for each mean stress axis orientation. The table reports: the numerical values of the mean stress tensors and the related 95% confidence intervals.

5 Discussion

5.1 Regional constraints on stress field evolution

In order to reconstruct an evolutionary model for the polyphase brittle tectonics recorded in the SDC, the obtained stress tensors were sorted according to the known sequence of regional tectonic phases that affected the Sierras Pampeanas and the Andean Precordillera between 27° and 33° S (e.g., Ramos et al., 2002).

During the Late Paleozoic to Mesozoic, these areas were affected by a sequence of extensional events, which developed seamlessly by commonly reactivating previous rift-related structures. Considering the obtained results, the proposed ~ NE-SW extensional episode (*Figure 2.6*) can be associated with the late Paleozoic formation of the intracratonic Paganzo basin (Salfity and Gorustovich, 1984), or, alternatively, to the subsequent development of the Triassic to Early Jurassic rift basins (e.g., Uliana et al., 1989; Ramos and Kay, 1991; Ramos et al., 2002). This is supported by Giambiagi and Martinez (2008), who analyzed extensional fault systems affecting Late Permian to Middle Triassic magmatic rocks of the Choiyoi Group (i.e., 270–230 Ma, according to Giambiagi and Martinez (2008) and references therein) in the Potrerillos-Uspallata area (western slopes of the Precordillera in the province of Mendoza) and proposed NNE–SSW extension (N23°E), indeed in agreement with the extensional tectonic phase outlined in this study. The magmatism of the Choiyoi Group is thought to result from orogenic collapse following terrane accretion during a period of relative relaxation or extension (see Ramos and Kay, 1991). The extensional regime outlined by Giambiagi and Martinez (2008) continued during the Triassic and led to

the formation of regional rift systems, such as the Triassic Cuyo basin in the province of Mendoza (Ramos and Kay, 1991).

By contrast, the ~ NW-SE extensional episode (*Figure 2.6*) has been associated with an Early Cretaceous extensional phase, which is likely to be connected to the earlier phase of the opening of the South Atlantic Ocean and was documented by Schmidt et al. (1995) in the nearby Sierra Chica and Sierra de El Gigante on Early Cretaceous rocks (i.e., K-Ar dates provided by Gordillo and Lencinas (1967b) from mafic lava flows). Schmidt et al. (1995) defined a WNW-ESE direction of crustal extension, (see also *Torsvik et al.*, 2010), which is orthogonal to the trend of the Early Cretaceous spreading center and compatible with the stretching direction constrained by the paleostress reconstruction of this study. The outlined sequence of extensional tectonic events is also supported by field evidence, which shows that some structures associated with the first NE-SW extensional episode were clearly reactivated during later NW-SE extension (e.g., site COR002, *Figure 2.6*).

These extensional fault systems were in part inverted during the Cenozoic Andean compression caused by the flat slab subduction of the Nazca Plate beneath the South American plate. This is recorded, for example, at site COR079-85, where the Nono thrust faults juxtaposes the Achala granite against Pliocene to late Pleistocene rocks, while the oblique ramp of the main Nono thrust likely represents an inverted normal fault structure. Therefore, the obtained compressional phase (σ_1 oriented ENE) can be associated with present-day Andean convergence, which, according to recent GPS surveys, is oriented N78°E (Vigny et al., 2009, see also Kendrick et al., 2003; Brooks et al., 2003). The σ_1 orientation calculated for the compressional phase appears to be also consistent with the orientations of the maximum horizontal compressive stress reported in the Word Stress Map between 27 and 32°S along the western South America plate margin (Heidbach et al., 2008). No evidence of neotectonic activity constrains the brittle deformation recorded at the Los Túneles section; this notwithstanding, the compressional episode recorded in La Mermela phyllite and Los Túneles mylonitic gneiss (*Figure 2.6*) can be related to the Andean compression as: (i) The stress tensors define a σ_1 orientation compatible with the present-

day Andean convergence (e.g., Kendrick et al., 2003; Brooks et al., 2003; Vigny et al., 2009; Heidbach et al., 2008) and the stress tensor obtained at site COR079-85; (ii) During fieldwork important evidence of reverse faulting reactivating normal structures of the previous extensional phases have been observed (e.g. see the unsorted field dataset for sites COR031 and COR049 in *Figure A.1*, Appendix A).

5.2 Age constraints on the proposed deformational history

The proposed evolutionary model has then been tested against existing time constraints for the SDC (i.e., Whitmeyer, 2008; Bense et al., 2013a, 2013b; Richardson et al., 2013) as reported in the following sections.

5.2.1 K–Ar illite fine-fraction age constraints

In the case of the Achala granite, the three identified tectonic events necessarily post-date the Late Devonian emplacement of the batholith (Dorais et al., 1997). Tighter constraints, however, can be derived from the analysis of the results by Bense et al. (2013a), who provide K–Ar illite gouge ages from brittle faults deforming the Achala granite and the Los Túneles section (*Figure 2.9*).

Bense et al. (2013a) analyzed two samples from a fault deforming the Achala granite corresponding to the exposure of our site COR011 (*Figure 2.1*C). Their finest dated fractions (< 0.2 micron in Bense et al. (2013a)) yielded Early Triassic ages of 251.4 ± 6.4 Ma and 249.2 ± 4.4 Ma and can be interpreted as maximum ages for the last recorded faulting episode (for example, see the Age Attractor Model of Torgersen et al.(2014), Torgersen et al. (2015) and Viola et al. (2016)). We interpret them as reliable constraints to our ~ NE-SW extensional phase, as the stress tensor produced by the inversion of COR011 fault-slip data defines the first extensional phase (*Figure 2.6*) and the structural and kinematics analysis at this site does not reveal signs of reactivation of the dated fault.

K/Ar fault gouge illite dating also constrains the brittle episodes along the Los Túneles section. The brittle-ductile transition in Los Túneles area took place in the Early

Carboniferous, as indicated by pseudotachylite $^{40}Ar/^{39}Ar$ ages of 345 ± 5 Ma and 348 ± 2 Ma (Whitmeyer, 2008). Bense et al. (2013a) dated by illite K-Ar two samples along the Los Túneles section, which yielded 246.4 Ma and 225.7 ± 8.8 Ma for the < 0.2 micron fractions (*Figure 2.9*). These results are not easily interpreted and assigned to our tensors as they are not associated with specific localities and Bense et al. (2013a) did not correlate the geochronological results with any structural information or fault-slip data. However, it is reasonable to assume that these Early to Late Triassic ages also date the first, NE-SW extensional phase, which has been constrained to the Early Triassic in the Achala granite and was associated, from a regional point of view, to the Permo-Triassic extension (Salfity and Gorustovich, 1984; Giambiagi and Martinez, 2008) and to the subsequent development of the Triassic to Early Jurassic rift basins.

The ages of the coarser <2 and 2-6 micron fractions by Bense et al. (2013a) from the Achala granite and the Los Túneles samples (except the 2-6 micron age of Los Túneles sample 94-09) are similar and define a broad, flat plateau between 278.2 ± 6 Ma and 307.5 ± 6.9 Ma (*Figure 2.9*). This might indicate an earlier deformation phase in the Early Permian (see Torgersen et al., 2015; Viola et al., 2016).

5.2.2 (U-Th)/He thermochronometry age constraints

Mean apatite (U-Th)/He cooling ages ranging between 257 ± 45 Ma and 180 ± 44 Ma were published by Richardson et al. (2013) along the Sierra Grande western scarp (Achala area, *Figure 2.10*). These ages indicate that, assuming a geothermic gradient of 25 °C/km (Richardson et al., 2013; Bense et al., 2013b), the whole Achala batholith was within the upper ~3 km of the crust since ~ 180 Ma. In the light of our field and structural analysis, the samples collected by Richardson et al. (2013), from within the Sierra Grande fault hanging-wall, are along a section transected by an important normal fault (i.e., COR011). In particular, the samples across the fault zone (TR 4 and TR 9) are associated with 265 ± 12 and 209 ± 34 zircon (U-Th)/He dating respectively. The difference in age between TR 4 and TR 9 (i.e., 56 Ma) is not justified by their difference in elevation (i.e., 430 m) considering the

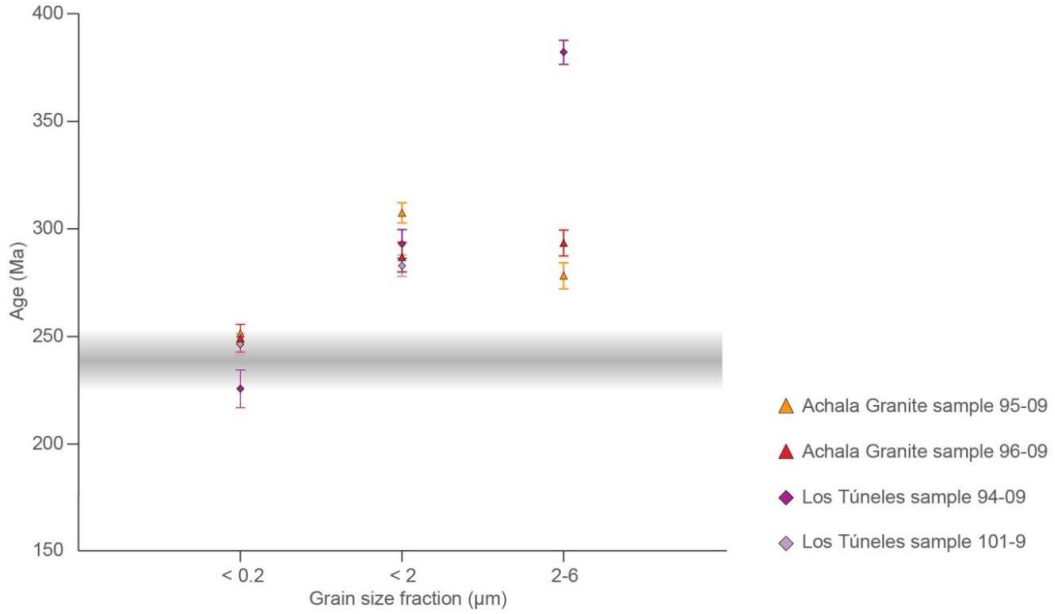

Location	Sample	Grain Fraction (µm)	K2O (wt%)	40Ar* (nl/g) STP	40Ar* (%)	Age (Ma)	2σ (Ma)
Los Túneles	94-09	2-6	4,92	38,14	89,8	382,1	5,6
		< 2	6,07	62,29	95,22	293	6,7
		< 0,2	6,92	94,97	98,94	225,7	8,8
	101-09	2-6	3,02	25,71	94,79		5,9
		< 2	2,63	25,97	95,04	282,9	5
		< 0,2	–	–	–	246,4	–
Achala	95-09	2-6	4,29	37,31	94,26	278,2	6
		< 2	5,32	57,52	96,79	307,5	6,9
		< 0,2	7,1	68,87	98,84	251,4	6,4
	96-09	2-6	4,88	42,05	92,34	293,5	6,1
		< 2	5,08	50,95	95,37	286,9	4,7
		< 0,2	4,32	44,41	98,92	249,2	4,4

Figure 2.9: *K–Ar illite ages vs. grain size for the samples analyzed by Bense et al. (2013a) in the Los Túneles section and Achala granite. The dashed grey horizontal bar loosely defines the last inferred faulting episode of Triassic age.*

regional geothermic gradient of 25 °C/km. This is instead presumably related to the activity of the NE dipping normal fault measured at site COR011 (*Figure 2.2B*). A rough differential exhumation can be inferred by assuming zircon and apatite (U-Th)/He dating samples at the same elevation in the hanging-wall (i.e., 1929 m for TR 9 and TR 15) rather than in the footwall (i.e., 1408m for TR 4 and TR 3b). This is reasonable given the low difference in

elevation between the two samples of the footwall (i.e., 117 m between TR 4 and TR 3b) and the hanging-wall (i.e., 611 m between TR 9 and TR 15). The resulting diagram (*Figure 2.10*) shows that between 209 Ma and 180 Ma the footwall was exhumed more rapidly than the hanging-wall (0.155 mm/Ma vs 0.018 mm/Ma, given a geothermic gradient of 25 °C/km), which implies indeed a normal displacement along the COR011 fault. On the contrary, starting at 180 Ma the exhumation of the two blocks slowed down to similar values. Although these observations should be taken cautiously and need to be integrated and verified against results from a larger number of samples, they clearly suggest that the activity associated with the normal fault measured at site COR011 (which is related to the first extensional phase) extended until early Jurassic times.

The thermochronological data produced by Bense et al. (2013b) along Los Túneles section are represented by apatite fission-track and zircon and apatite (UeTh)/He dating, and were obtained from samples located in the footwall and hanging-wall of the Pocho fault (AUY 38-10 and APM 59-08, respectively) and the La Mermela fault zone (APM 59-08 and APM 55-08, respectively), (*Figure 2.10*). For these three samples of the Los Túneles section, Bense et al. (2013b) calculated the best fitting paths from HeFTy cooling models reported in *Figure 2.9*, which suggests an extensional activity along the two faults up to the Early Cretaceous. Most likely, this activity represents the last extensional phase recorded by paleostress analysis.

5.3 Brittle tectonic evolutionary model for the Sierras de Córdoba

Considering the available independent geological and chronological constraints on the brittle deformation history and the evaluation of stress homogeneity among the computed paleostress tensors for each tectonic phase, a conceptual evolutionary model for the polyphase brittle tectonic evolution of the SDC was produced (*Figure 2.11*). In this model, the NE-SW extensional phase is thought to reflect regional Permo-Triassic/Early Jurassic extension. This extensional regime has been dated to the Early to Late Triassic by K-Ar fault gouge illite ages and to the Early Jurassic by U-Th/He ages.

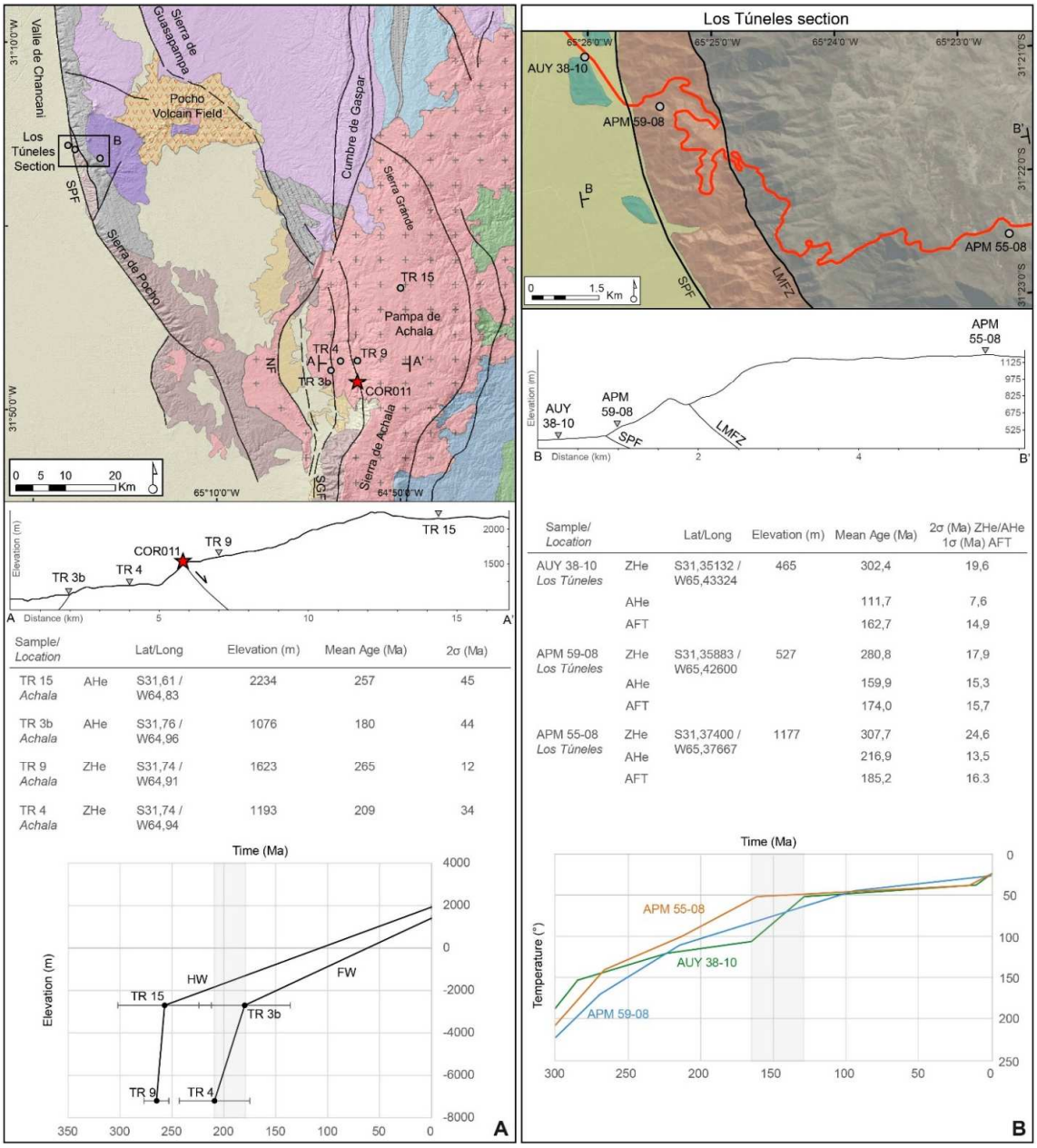

Sample/ Location		Lat/Long	Elevation (m)	Mean Age (Ma)	2σ (Ma)
TR 15 *Achala*	AHe	S31,61 / W64,83	2234	257	45
TR 3b *Achala*	AHe	S31,76 / W64,96	1076	180	44
TR 9 *Achala*	ZHe	S31,74 / W64,91	1623	265	12
TR 4 *Achala*	ZHe	S31,74 / W64,94	1193	209	34

Sample/ Location		Lat/Long	Elevation (m)	Mean Age (Ma)	2σ (Ma) ZHe/AHe 1σ (Ma) AFT
AUY 38-10 *Los Túneles*	ZHe	S31,35132 / W65,43324	465	302,4	19,6
	AHe			111,7	7,6
	AFT			162,7	14,9
APM 59-08 *Los Túneles*	ZHe	S31,35883 / W65,42600	527	280,8	17,9
	AHe			159,9	15,3
	AFT			174,0	15,7
APM 55-08 *Los Túneles*	ZHe	S31,37400 / W65,37667	1177	307,7	24,6
	AHe			216,9	13,5
	AFT			185,2	16.3

Figure 2.10: *Published thermochronological data by Richardson et al. (2013) along the Sierra Grande western scarp (a) and by Bense et al. (2013b) along the Los Túneles section (b), showing the inferable information about the age of fault* activities.

The NW-SE extensional phase is attributed to Early Cretaceous tectonics on the base of regional consideration and published U-Th/He ages. Finally, the youngest compressional stress field (sub-horizontal ENE-WSW σ_1 axis) is tentatively linked to Andean tectonism on

the base of clear evidence of neotectonic activity and kinematic and geometric compatibility of the obtained stress tensors with the current direction of convergence.

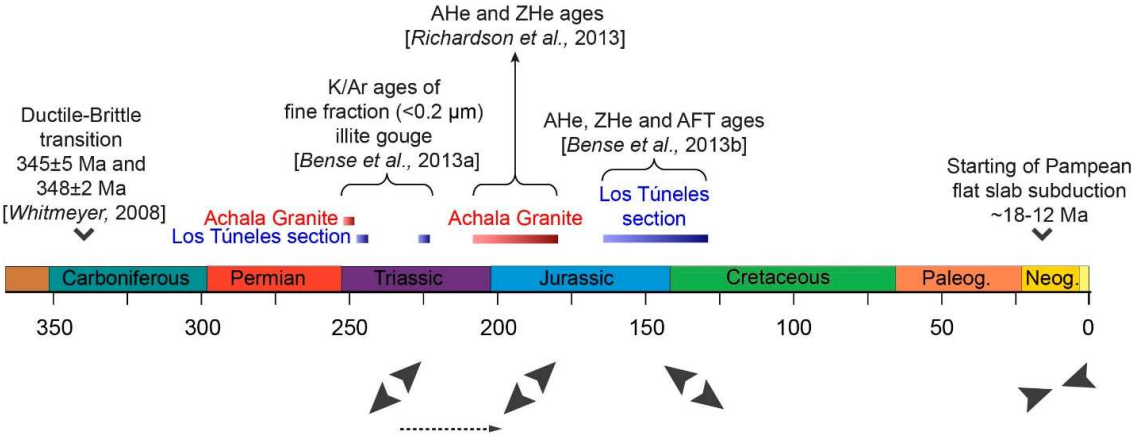

Figure 2.11: *Conceptual evolutionary model for the polyphase brittle tectonic evolution of the Sierra de Córdoba reporting the considered time constraints on the top.*

6 Conclusions

The brittle regional polyphase deformation history of the Sierras de Córdoba of the Eastern Sierras Pampeanas appears to be dominated by two extensional episodes (σ_3 oriented NE and NW, respectively) spanning the Early Triassic to Early Cretaceous time interval, followed by a compressional paleostress regime (σ_1 oriented ENE), which is compatible with the present-day Andean convergence.

The first episode appears to be associated with a regional extensional phase which, based on K/Ar fault gouge illite dating and U-Th/He ages, lasted from Early Triassic to Early Jurassic. This extension might be connected to the formation of the Late Paleozoic intracratonic Paganzo basin and to the subsequent opening of Triassic to Early Jurassic rift basins.

The second episode is well developed in the study area and, consistently with indirect constraints derived from the analysis of the regional evolution of the Eastern Sierras Pampeanas and published U-Th/He ages, is assigned to an Early Cretaceous extensional phase associated with the initial opening of the South Atlantic Ocean.

The final compressional episode inverted the older, inherited normal faults and is responsible for the neotectonic activity in the study area. The reconstructed shortening direction (ENE σ_1) is indeed compatible with the present-day Andean tectonism, suggesting that the current plate convergence has not significantly changed since at least the Late Pliocene.

Paleostress analysis has been critically applied by carefully considering each of the analyzed fault zones and the different mechanical behavior of the lithological domains they deform. A statistical analysis was carried out on stress tensors retrieved from different fault zones for each tectonic event, which allowed to conclude overall stress field homogeneity for the Sierras de Córdoba during all reconstructed deformation events. Given that no systematic or significant local heterogeneities in stress distribution were found, we conclude that the results of the performed stress inversion procedure are meaningful and fully representative for all the analyzed fault zones.

The adopted methodological workflow provides an efficient means to unravel polyphase brittle tectonics within lithologically heterogeneous rock domains characterized by a complex reactivation history, where the evaluation of possible stress heterogeneities is necessary to avoid the erroneous identification of tectonic phases, which are instead solely the expression of local stress perturbations.

Acknowledgments

Patricia Alvarado and the seismotectonics research group of the University of San Juan (AR) and CIGEOBIO-CONICET are warmly thanked for logistics and technical support during our stay in Argentina. In particular, we are grateful to Agostina Lia Venerdini, Yamila Dubokivic and Gustavo Ortiz for the assistance provided during the field work. Stress inversion was performed using Win_Tensor, a software developed by Dr. Damien Delvaux, Royal Museum for Central Africa, Tervuren, Belgium. Slip tendency analysis and tensor averaging with bootstapping was performed with applications developed by Andrea Bistacchi (andrea.bistacchi@unimib.it). This research was funded by the Università degli Studi di Padova, Scientific Research funds, part EX 60% 2014-2015 and DOR 2016, and by the European Research Council Consolidator Grant Project (NOFEAR) No 614705.

References

Alvarado, P., Beck, S., Zandt, G., Araujo, M., Triep, E., 2005a. Crustal deformation in the south-central Andes backarc terranes as viewed from regional broad-band seismic waveform modelling. Geophysical Journal International 163, 580–598, doi:10.1111/j.1365-246X.2005.02759.x.

Alvarado, P., Machuca, B.C., Beck, S.L., 2005b. Comparative seismic and petrographic crustal study between the Western and Eastern Sierras Pampeanas region, Argentina. Revista de la Asociación Geológica Argentina 60, 787–796.

Bellahsen, N., Sebrier, M., Siame, L., 2016. Crustal shortening at the Sierra Pie de Palo (Sierras Pampeanas, Argentina): near-surface basement folding and thrusting. Geological Magazine 153(5–6), 992–1012, doi:10.1017/S0016756816000467.

Bense, F.A., Wemmer, K., Löbens, S., Siegesmund, S., 2013a. Fault gouge analyses: K–Ar illite dating, clay mineralogy and tectonic significance–a study from the Sierras Pampeanas, Argentina. International Journal of Earth Sciences 103, 189–218, doi:10.1007/s00531-013-0956-7.

Bense, F. A., Löbens, S., Dunkl, I., Wemmer, K., Siegesmund, S., 2013b. Is the exhumation of the Sierras Pampeanas only related to Neogene flat-slab subduction? Implications from a multi-thermochronological approach. Journal of South American Earth Sciences 48, 123–144, doi:10.1016/j.jsames.2013.09.002.

Bistacchi, A., Massironi, M., Menegon, L., Bolognesi, F., Donghi, V., 2012. On the nucleation of non-Andersonian faults along phyllosilicate-rich mylonite belts. Geological Society of London, Special Publications 367(1), 185–199, doi:10.1144/sp367.13.

Bonalumi, A., Martino, R., Baldo, E., Zarco, J., Sfragulla, J., Carignano, C., Kraemer, P., Escayola, M., Tauber, A., 1999. Hoja Geológica 3166-IV, Villa Dolores, Provincias de Córdoba, La Rioja y San Luis. Instituto de Geología y Recursos Minerales, Servicio Geológico Minero Argentino, Buenos Aires, Boletín 250, 123.

Borradaile, G.J., 2003. Statistics of Earth Science Data: Their Distribution in Time, Space and Orientation. first ed. Springer, 351.

Bott, M.H.P. 1959. The mechanics of oblique slip faulting. Geological Magazine 96, 109–117.

Boyer, S., Elliot, D., 1982. Thrust systems. American Association of Petroleum Geologists Bulletin 66, 1196– 230.

Brooks, B. A., Bevis, M., Smalley Jr., R., Kendrick, E., Manceda, R., Lauria, E., Maturana, R., Araujo, M., 2003. Crustal motion in the Southern Andes (26 -36 S): Do the Andes behave like a microplate?. Geochemistry Geophysics Geosystems 4(10), 1085, doi:10.1029/2003GC000505.

Charlersworth, H., Cruden, D., Ramsden, J., Huang, Q., 1989. Orient: An interactive Fortran 77 program for processing orientations on a microcomputer. Computers & Geosciences 15(3), 275–293.

Collettini, C., Sibson, R.H., 2001. Normal faults normal friction?. Geology 29, 927–930, doi:10.1130/0091-7613(2001)029<0927:NFNF> 2.0.CO;2.

Costa, C.H., Machette, M.N., Dart, R.L., Bastias, H.E., Paredes, J.D., Perucca, L.P., Tello, G.E., Haller, K.M., 2000. Map and database of Quaternary faults and folds in Argentina, U.S. Geological Survey Open File Report, 00–0108.

Costa, C.H., Murillo, M.V., Sagripanti, G.L., Gardini, C.E. 2001. Quaternary intraplate deformation in the southeastern Sierras Pampeanas, Argentina. Journal of Seismology 5, 399–409.

Costa, C.H., Massabie, A.C., Sagripanti, G.L., Brunetto, E., Coppolecchia, M., 2014. Neotectónica. Relatorio del 19º Congreso Geológico Argentino, Asociación Geológica Argentina, Córdoba, 725–746.

Crider, J.G. 2015. The initiation of brittle faults in crystalline rock. Journal of Structural Geology 77, 159–174, doi: 10.1016/j.jsg.2015.05.001.

Di Toro, G., Goldsby, D.L., Tullis, T.E., 2004. Friction falls towards zero in quartz rock as slip velocity approaches seismic rates. Nature 427, 436–439.

Delvaux, D. 2011. Win-Tensor, an interactive computer program for fracture analysis and crustal stress reconstruction. EGU General Assembly, Vienna, 2011. Geophysical Research Abstracts, Vol. 13, EGU2011-4018.

Delvaux, D. 2012. Release of program Win-Tensor 4.0 for tectonic stress inversion: statistical expression of stress parameters. EGU General Assembly, Vienna, 2012. Geophysical Research Abstracts, Vol. 14, EGU2012-5899, doi:10.13140/RG.2.2.23415.62887

Delvaux, D. 2017. Version 5.8.7 and above of the Win-Tensor Program. (Available at http://users.skynet.be/damien.delvaux/Tensor/tensor- index.html.)

Delvaux, D., Moeys, R., Stabel, G., Petit, C., Levi, K., Miroschnichenko, A., Ruzhich, V., San'kov, D., 1997. Paleostress reconstructions and geodynamics of the Baikal region, Central Asia, Part II, Cenozoic rifting. In: Cloetingh, S., Fernandez, M., Munoz, J.A., Sassi, W., Horvath, F. (Ed.), Structural controls on sedimentary basin formation. Tectonophysics 282, 1–38.

Delvaux, D., Sperner, B., 2003. New aspects of tectonic stress inversion with reference to the TENSOR program. In: Nieuwland, D.A. (ed.), New Insights into Structural Interpretation and Modelling. Geological Society of London, Special Publication 212, 75–100, doi:10.1144/GSL.SP.2003.212.01.06.

Doblas, M. 1998. Slickenside kinematic indicators. Tectonophysics 295,187–197.

Dorais, M.J., Lira, R., Chen, Y., Tingey, D., 1997. Origin of biotite– apatite-rich enclaves, Achala Batholith, Argentina. Contributions to Mineralogy and Petrology 130, 31–46.

Famin, V., Raimbourg, H., Garcia, S., Bellahsen, N., Hamada, Y., Boullier, A.M., Fabbri, O., Michon, L., Uchide, T., Ricci, T., Hirono, T., Kawabata, K., 2014. Stress rotations and the long-term weakness of the Median Tectonic Line and the Rokko-Awaji Segment. Tectonics 33(10), 1900–1919, doi: 10.1002/2014TC003600.

Fisher, N.I., Lewis, T.L., Embleton, B.J.J., 1987. Statistical analysis of spherical data. Cambridge University Press, Cambridge, U.K., 329.

Giambiagi, L., Martinez, A.N., 2008. Permo-Triassic oblique extension in the Potrerillos-Uspallata area, western Argentina. Journal of South American Earth Sciences 26(3), 252–260, doi:10.1016/j.jsames.2008.08.008.

Gordillo, C. 1984. Migmatitas cordieríticas de las Sierras de Córdoba; condiciones físicas de la migmatización. Academia Nacional de Ciencias, Córdoba, 68, 1–40.

Gordillo, C., Lencinas, A., 1967b. El basalto nefelínico de El Pungo. Boletín Academia Nacional Ciencias, Córdoba, 46, 110–115.

Gordillo, C., Linares, E., 1981. Geocronología y petrografía de las vulcanitas del Departamento Pocho, Provincia de Córdoba. Revista de la Asociación Geológica Argentina 36(4), 380–388.

Guereschi, A. B., Martino, R. D., 2014. Las migmatitas de las Sierras de Córdoba. In: Martino, R.D., Guereschi, A.B. (Ed.) Geología y Recursos Naturales de la Provincia de Córdoba. Relatorio del 19º Congreso Geológico Argentino, Asociación Geológica Argentina, Córdoba, 67–94.

Jordan, T.E., Allmendinger, R.W., 1986. The Sierras Pampeanas of Argentina: A modern analogue of Rocky Mountain foreland deformation. American Journal of Science 286, 737–764.

Hiecke-Merlin, O., Piccoli, G., 1961. Studi geologici e petrografici su un gruppo di vulcani della sierra de Córdoba (Argentina). Memorie degli Istituti di Geologia e Mineralogia dell'Università di Padova, Padova, 33, 1–29.

Heidbach, O., Tingay, M., Barth, A., Reinecker, J., Kurfeß, D., Müller, B., 2008. The World Stress Map database release 2008, doi:10.1594/GFZ.WSM.Rel2008.

Huang, G., Charlesworth, H., 1989. A FORTRAN-77 program to separate a heterogeneous set of orientations into subsets. Computers & Geosciences 15, 1–7.

Hünicken, M., Pensa, M., 1980. Estratigrafía y tectónica de las sedimentitas neopaleozoicas (Fm. Chancaní) y de las filitas (Fm. La Mermela) del borde occidental de las Sierras

de Pocho y Guasapampa. Actas Academia Nacional de Ciencias, Córdoba, 53, 255–286.

Kendrick, E., Bevis, M., Smalley, R., Brooks, B., Vargas, R.B., Lauría, E., Fortes L.P.S. 2003. The Nazca-South America Euler vector and its rate of change. Journal of South American Earth Sciences 16(2), 125–131, doi:10.1016/S0895-9811(03)00028-2.

Kay, S.M., Gordillo, C.E., 1994. Pocho volcanic rocks and the melting of depleted continental lithosphere above a shallowly dipping subduction zone in the central Andes. Contributions to Mineralogy and Petrology 117, 25–44.

Kay, S.M., Abbruzzi, J.M., 1996. Magmatic evidence for Neogene lithospheric evolution of the central Andean "flat-slab" between 30 S and 32 S. Tectonophysics 259,15–28, doi:10.1016/0040-1951(96)00032-7.

Kay, S.M., Mpodozis, C., 2002. Magmatism as a probe to the Neogene shallowing of the Nazca plate beneath the modern Chilean flat-slab. Journal of South American Earth Sciences 15, 39–57, doi:10.1016/S0895-9811(02)00005-6.

Kraemer, P.E., Tauber, A., Schmidt, C., Ramé, G., 1993. Analisis cinemático de la "Falla de Nono." Evidencias de actividad neotectónica. Valle de San Alberto, Provincia de Córdoba. XII Congreso Geológico Argentino y II Congreso de Exploracíon de Hidrocarburos, Valle de San Alberto, Argentina, Actas TIII.

Lacombe, O., 2012. Do fault slip data inversions actually yield "paleostresses" that can be compared with contemporary stresses? A critical discussion. Comptes Rendus Geoscience 344(3–4), 159–173, doi:10.1016/j.crte.2012.01.006.

Lockner, D.A., Morrow, C., Moore, D., Hickman, S., 2011. Low strength of deep San Andreas fault gouge from SAFOD core. Nature 472(7341), 82–85.

Marrett, R.A., Allmendinger, R.W., 1990. Kinematic analysis of fault-slip data. Journal of Structural Geology 12, 973–986.

Martino, R.D., 2003. Las fajas de deformación dúctil de las Sierras Pampeanas de Córdoba: Una reseña general. Revista de la Asociación Geológica Argentina 58, 549–571.

Martino, R.D., Guereschi, A.B., Caro Montero, A., 2016. Reactivation, inversion and basement faulting and thrusting in the Sierras Pampeanas of Córdoba (Argentina) during Andean flat-slab deformation. Geological Magazine 1–30, doi:10.1017/S0016756816000339.

Massabie, A., Sanguinetti, A., Lo Forte, G., Cegarra, M., 2003. La actividad neotectónica en la sierra Baja de San Marcos-Cruz del Eje, flanco occidental de las Sierras Pampeanas Orientales. Revista de la Asociación Geológica Argentina 58, 653–663.

Massironi, M., Bistacchi, A., Menegon, L., 2011. Misoriented faults in exhumed metamorphic complexes : Rule or exception?. Earth And Planetary Science Letters 307(1–2), 233–239, doi:10.1016/j.epsl.2011.04.041.

Mattila, J., Viola, G., 2014. New constraints on 1.7 Gyr of brittle tectonic evolution in southwestern Finland derived from a structural study at the site of a potential nuclear waste repository (Olkiluoto Island). Journal of Structural Geology 67, 50–74, doi:10.1016/j.jsg.2014.07.003.

Mehl, C., Jolivet, L., Lacombe, O., 2005. From ductile to brittle: Evolution and localization of deformation below a crustal detachment (Tinos, Cyclades, Greece). Tectonics 24(4), 1–23, doi: 10.1029/2004TC001767.

Mpodozis, C., Ramos, V.A., 1990. The Andes of Chile and Argentina. In: Ericksen, G.E., Canas Pinochet, M.T., Reinemud, J.A. (Ed.), Geology of the Andes and its Relation to Hydrocarbon and Mineral Resources. Earth Science Series 11, 59–90.

Peacock, D.C.P., Sanderson, D.J., 1992. Effects of layering and anisotropy on fault geometry. Journal of the Geological Society, London 149(5), 793–802, doi: 10.1144/gsjgs.149.5.0793.

Petit, J.P., 1987. Criteria for the sense of movement on fault surfaces in brittle rocks. Journal of Structural Geology 9, 597–608.

Ramos, V.A., 1988a. The tectonics of the Central Andes; 30° to 33° S latitude. Geological Society of America, Special Papers 218, 31–54, doi:10.1130/SPE218-p31.

Ramos, V.A., 1988b. Late Proterozoic-Early Paleozoic of South America e a collision history. Episodes 11, 168–174.

Ramos, V.A., Jordan, T. E., Allmendinger, R.W., Mpodozis, C., Kay, S.M., Cortés, J.M., Palma, M.A., 1986. Paleozoic terranes of the central Argentine-Chilean Andes. Tectonics 5(6), 855–880.

Ramos, V.A., Kay, S. M., 1991. Triassic rifting and associated basalts in the Cuyo basin, central Argentina. In: Harmon, R.S., Rapela, C.W. (Ed.), Andean Magmatism and its Tectonic Setting Geological Society of America, Special Papers 265, 79–91.

Ramos, V.A., Cristallini, E.O., Perez, D.J., 2002. The Pampean flat- slab of the Central Andes. Journal of South American Earth Sciences 15, 59–78.

Rapela, C.W., Pankhurst, R.J., Casquet, C., Baldo, E.G., Saavedra, J., Galindo, C., Fanning, C.M., 1998b. The Pampean orogeny of the southern proto-Andes: Cambrian continental collision in the Sierras de Córdoba. Geological Society of London, Special Publications 142, 181–218.

Rapela, C.W., Pankhurst, R.J., Casquet, C., Fanning, C.M., Baldo, E.G., González-Casado, J.M., Galindo, C., Dahlquist, J., 2007. The Río de la Plata craton and the assembly of SW Gondwana. Earth-Science Reviews 83, 49–82.

Rice, J.R., 1992. Fault stress states, pore pressure distributions, and the weakness of the San Andreas Fault. In: Wong, T. (Ed.), Fault Mechanics and Transport Properties of Rocks. Academic Press, San Diego 475–503.

Richardson, T., Gilbert, H., Anderson, M., Ridgway, K.D., 2012. Seismicity within the actively deforming Eastern Sierras Pampeanas, Argentina. Geophysical Journal International 188, 408–420, doi:10.1111/j.1365-246X.2011.05283.x.

Richardson, T., Ridgway, K.D., Gilbert, H., Martino, R., Enkelmann, E., Anderson, M., Alvarado, P., 2013. Neogene and Quaternary tectonics of the Eastern Sierras Pampeanas, Argentina: Active intraplate deformation inboard of flat-slab subduction. Tectonics 32(3), 780–796, doi:10.1002/tect.20054.

Rossello, E., Mozetic, M.E., 1999. Caracterizacion estructural y significado geotectonico de los depocentros cretacicos continentales del centro-oeste argentine. 5° Simposio sobre o Cretaceo do Brasil, Boletim 5, 107–113.

Saintot, A., Stephens, M.B., Viola, G., Nordgulen, Ø., 2011. Brittle tectonic evolution and paleostress field reconstruction in the southwestern part of the Fennoscandian Shield, Forsmark, Sweden. Tectonics 30, 1–36, doi:10.1029/2010TC002781.

Salfity, J.A., Gorustovich, S.A., 1984. Paleogeografıa del Grupo Paganzo (Paleozoico Superior). Revista de la Asociación Geológica Argentina 38, 437–453.

Schmidt, C.J., Astini, R.A., Costa, C.H., Gardini, C.E., Kraemer, P.E., 1995. Cretaceous rifting, alluvial fan sedimentation, and neogene inversion, Southern Sierras Pampeanas, Argentina. In: Tankard, A.J., Suarez, R., Welsink, H.J. (Ed.). Petroleum Basins of South America. AAPG Memoir 62, 341–358.

Sibson, R.H., 1985. A note on fault reactivation. Journal of Structural Geology 7, 751–752.

Siegesmund, S., Steenken, A., Martino, R., Wemmer, K., López De Luchi, M., Frei, R., Presnyakov, S., Guereschi, A., 2010. Time constraints on the tectonic evolution of the Eastern Sierras Pampeanas (Central Argentina). International Journal of Earth Sciences 99, 1199–226.

Simpson, C., Whitmeyer, S., De Paor, D.G., Gromet, L.P., Miro, R., Krol, M.A., Short, H., 2001. Sequential ductile through brittle reactivation of major fault zones along the accretionary margin of Gondwana in Central Argentina. Geological Society of London, Special Publications 186.

Simpson, C., Law, R.D., Gromet, L.P., Miro, R., Northrup, C.J., 2003. Paleozoic deformation in the Sierras de Córdoba and Sierra de Las Minas, eastern Sierras Pampeanas, Argentina. Journal of South American Earth Sciences 15, 749–764.

Sims, J., Ireland, T.R., Camacho, A., Lyons, P., Pieters, P.E., Skirrow, R., Stuart-Smith, P., Miro, R., 1998. U–Pb, Th–Pb and Ar–Ar geochronology from the southern Sierras Pampeanas, Argentina: implications for the Paleozoic tectonic evolution of the

western Gondwana margin. Geological Society of London, Special Publications 142, 259–281.

Sperner, B., Zweigel, P., 2010. A plea for more caution in fault-slip analysis. Tectonophysics 482(1–4), 29–41.

Steenken, A., López de Luchi, M.G., Siegesmund, S., Wemmer, K., Pawlig, S., 2004. Crustal provenance and cooling of the basement complexes of the Sierra de San Luis: an insight into the tectonic history of the proto-Andean margin of Gondwana. Gondwana Research 7 (4), 1171–1195.

Steenken, A., Wemmer, K., Martino, R.D., López de Luchi, M.G., Guereschi, A., Siegesmund, S., 2010. Post-Pampean cooling and the uplift of the Sierras Pampeanas in the west of Córdoba (Central Argentina). Neues Jahrbuch Fur Geologie Und Palaontologie-Abhandlungen 256(2), 235–255, doi:10.1127/0077-7749/2010/0094.

Stipanicic P.N., Linare, E., 1975. Catálogo de edades Radiométricas determinadas para la República Argentina I, Años 1960–1974. Asociatión Geológica Argentina, Publication Especial B3, 1–42.

Tchalenko, J.S., 1970. Similarities between shear zones of different magnitudes. Geological Society of America Bulletin 81, 1625–1640.

Torgersen, E., Viola, G., Zwingmann, H., Harris, C., 2014. Structural and temporal evolution of a reactivated brittle–ductile fault – Part II: Timing of fault initiation and reactivation by K–Ar dating of synkinematic illite/muscovite. Earth and Planetary Science Letters 410, 212–224, doi:10.1016/j.epsl.2014.09.051.

Torgersen, E., Viola, G., Zwingmann, H., Henderson, I.H.C., 2015. Inclined K–Ar illite age spectra in brittle fault gouges: effects of fault reactivation and wall-rock contamination. Terra Nova 27, 2, 106–113.

Torsvik, T.H., Rousse, S., Smethurst, M.A., 2010. Reply to comment by D. Aslanian and M. Moulin on “A new scheme for the opening of the South Atlantic Ocean and the dissection of an Aptian salt basin.”. Geophysical Journal International 183(1), 29–34, doi:10.1111/j.1365-246X.2010.04728.x.

Traforti, A., Massironi, M., Bistacchi, A., Zampieri, D., Viola, G., (Chapter 3). Unravelling polyphase brittle deformation histories - Part II: Slip Tendency Analysis as a tool to constrain the mechanical properties of anisotropic rocks. Journal of Structural Geology.

Tricart, P., Schwartz, S., Sue, C., Lardeaux, J.M., 2004. Evidence of synextension tilting and doming during final exhumation from analysis of multistage faults (Queyras Schistes lustrés, Western Alps). Journal of Structural Geology 26(9), 1633–1645, doi: 10.1016/j.jsg.2004.02.002.

Uliana, M.A., Biddle, K.T., Cerdan, J., 1989. Mesozoic extension and the formation of Argentine sedimentary basins. In: Tankard, A.J., Balkwill, H.R. (Ed.), Extensional Tectonics and the Stratigraphy of the North Atlantic Margins. AAPG Memoir 46, 599–614

Urbina, N., Sruoga, P., Malvicini, L., 1997. Late Tertiary gold-bearing volcanic belt in the Sierras Pampeanas of San Luis, Argentina. International Geology Review 39, 287–306.

Vigny, C., Rudloff, A., Ruegg, J., Madariaga, R., Campos, J., Alvarez, M., 2009. Upper plate deformation measured by GPS in the Coquimbo Gap, Chile. Physics of The Earth and Planetary Interiors 175, 86–95.

Viola, G., Venvik Ganerød, G., Wahlgren, C.-H., 2009. Unraveling 1.5 Ga of brittle deformation history in the Laxemar-Simpevarp area, southeast Sweden: A contribution to the Swedish site investigation study for the disposal of highly radioactive nuclear waste. Tectonics 28, TC5007, doi:10.1029/2009TC002461.

Viola, G., Kounov, A., Andreoli, M.A.G., Mattila, J., 2012. Brittle tectonic evolution along the western margin of South Africa: More than 500Myr of continued reactivation. Tectonophysics 514–517, 93–114, doi:10.1016/j.tecto.2011.10.009.

Viola, G., Scheiber, T., Fredin, O., Zwingmann, H., Margreth, A., Knies, J., 2016. Deconvoluting complex structural histories archived in brittle fault zones. Nature Communications 7, 13448, doi:10.1038/ncomms13448.

Wallace, R.E. 1951. Geometry of shearing stress and relation to faulting. Journal of Geology 59, 118–130.

Whitmeyer, S.J., Simpson, C., 2003. High strain-rate deformation fabrics characterize a kilometers-thick Paleozoic fault zone in the eastern Sierras Pampeanas, central Argentina. Journal of Structural Geology 25, 909–922.

Whitmeyer, S.J., 2008. Dating fault fabrics using modern techniques of $^{40}Ar/^{39}Ar$ thermochronology: evidence for Paleozoic deformation in the Eastern Sierras Pampeanas, Argentina. In: De Paor, D. (Ed.), Making Sense of Shear. Journal of the Virtual Explorer 30, paper 3, doi:10.3809/jvirtex.2008.00207.

Yáñez, G.A., Ranero, C.R., Von Huene, R., Díaz, J. 2001. Magnetic anomaly interpretation across the southern central Andes (32°–34° S): The role of the Juan Fernández Ridge in the late Tertiary evolution of the margin. Journal of Geophysical Research 106(B4), 6325–45.

Zain Eldeen, U., Delvaux, D., Jacobs, P., 2002. Tectonic evolution in the Wadi Araba segment of the Dead Sea Rift, South-West Jordan. European Geophysical Society, Special Publication Series 2, 1–29.

3. Unravelling polyphase brittle deformation histories - Part II: Slip Tendency Analysis as a tool to constrain the mechanical properties of anisotropic rocks

A. Traforti[a], M. Massironi[a], A. Bistacchi[b], D. Zampieri[a], and G. Viola[c]

[a] Dipartimento di Geoscienze, Università degli Studi di Padova, via Gradenigo, 6, 35131 Padova, Italy.

[b] Dipartimento di Scienze Geologiche e Geotecnologie, Università degli Studi di Milano Bicocca, Piazza della Scienza 4, 20126 Milano, Italy.

[c] Dipartimento di Scienze Biologiche, Geologiche ed Ambientali, Università degli Studi di Bologna, Via Zamboni 67, 40126 Bologna, Italy.

Abstract

The mechanical strength of foliated rocks is typically anisotropic because it varies with the orientation of the foliation relative to the applied principal stresses and depends on phyllosicate content and physical interconnectivity. We constrain the degree of mechanical anisotropy associated with pre-existing planar discontinuities (metamorphic foliations and inherited faults) by combining paleostress analysis and meso- and microscale characterization of brittle failure modes in different phyllosilicate-bearing rocks outcropping in the Sierras de Córdoba (SDC) of Central Argentina. The SDC show evidence of a long brittle deformation history (Early Triassic – Present time) with three distinct brittle deformational events. Each phase caused new strain increments accommodated by the formation of neo-formed faults or by the reactivation of inherited discontinuities. Structural investigations reveal that the analyzed rock types (gneiss and phyllite) deformed by different failure modes during the different events. This enabled us to set up a conceptual field-scale triaxial experiment by applying a stress model based on normalized slip tendency analysis. We constrained the friction coefficient for slip along the foliations (μs) and along pre-existing faults (μf) to 0.3-0.2 and 0.4 respectively. These values fit independent estimates for similar rocks confirming the potential of our approach to other case studies.

1 Introduction

Upper crustal deformation is invariably accommodated either by the nucleation and growth of new faults (generally satisfying the Anderson's theory of faulting) or the brittle reactivation of pre-existing mechanical planar anisotropies. In detail, in foliated metamorphic rocks, the successful reactivation of a pre-existing, inherited mechanical discontinuity depends essentially on its mechanical strength compared to the surrounding intact rock and on its orientation with respect to the applied stress field (e.g., Massironi et al., 2011). A pre-existing discontinuity is optimally oriented if its orientation coincides with the expected orientation of neo-formed faults for a given stress field (i.e., Andersonian faults); otherwise, the existing discontinuity can be considered misoriented (e.g., Sibson, 1985). Foliated metamorphic rocks are, therefore, typically anisotropic as their strength varies as a function of the orientation of the foliation with respect to the principal stress axes (e.g., Crider 2015): they can be readily reactivated along the foliation when the latter is favorably oriented or they can be strong, when the foliation is misoriented and new fractures need to form and dissect the foliation at a high angle (Jaeger et al., 2007). The geo-mechanical characterization of foliated rock anisotropy is mainly limited to laboratory experiments (Walsh & Brace, 1964; Donath, 1961 and 1972; Attewell & Sandford, 1974; McCabe & Koerner, 1975; Bell & Coulthard, 1997; Duveau et al. 1998; Collettini et al., 2009). These experiments, and in particular triaxial tests, can be performed to investigate the effects of the different orientation of the metamorphic foliation (within the deforming specimen) to the maximum compressive stress axis and therefore offer the potential to study in detail the variability of the internal friction coefficient (tangential stress/normal stress at failure), which varies between c. 0.3 in the case of the brittle (re)activation of favourably oriented anisotropies (i.e., foliation) and c. 0.7 in the case of the nucleation and propagation of newly formed fractures (Jaeger et al., 2007, Kronenberg et al., 1990; Moore & Lockner 2004, Bistacchi et al., 2012). This range reflects the content and, above all, the physical interconnectivity of weak mineral phases such as phyllosilicate minerals, which have been shown to drastically weaken the strength of foliated rocks and fault rocks (e.g.,

Collettini et al., 2009; Van Diggelen et al., 2010; Holdsworth et al., 2011; Massironi et al., 2011; Bistacchi et al., 2012). It should be stressed, however, that experimental deformation tests aimed at characterising the mechanical anisotropy of foliated and fault rocks (i.e., performed on natural samples e.g., Brown et al., 2003; 2006; Numelin et al., 2007; Collettini et al., 2009) yield results that are representative of only the tested volume and their extrapolation to larger volumes or domains may not be straightforward. This might become particularly limiting when dealing with the characterization of the mechanical behaviour of lithologically heterogeneous crustal blocks or fault zones with highly complex internal architectures (Numelin et al., 2007), such as reactivated faults (e.g. Torgersen and Viola, 2014; Viola et al., 2016), and of foliated rocks with variably oriented pre-existing discontinuities.

The aim of this contribution is to provide an independent, semi-quantitative method for assessing and estimating the mechanical anisotropy of crustal blocks induced by their pre-existing planar discontinuities (i.e., metamorphic foliations and inherited faults) and so characterize their mechanical behaviour at a significantly larger scale than that constrainable by laboratory experiments. Our proposed analytical approach relies on further refining the concept of mechanical anisotropy by combining the paleostress analysis of the brittle history of the crustal block under consideration (whose results constrain the stress field at the time of deformation) with the meso- and micro-scale characterization of the brittle failure modes in the different phyllosilicate-bearing rocks that deformed during the reconstructed brittle polyphase tectonic evolution.

The chosen study area is the Sierras de Córdoba (SDC) of the Eastern Sierras Pampeanas (ESP), which consist of a series of N-S trending basement ranges located in the Andean foreland of Central Argentina (*Figure 3.1*). These ranges show compelling evidence of a long-lasting brittle deformation history, which has been studied and sorted out in the companion paper of this contribution (Traforti et al., Chapter 2). Traforti et al. (Chapter 2) present an evolutionary model for the SDC that is time-constrained and integrates a

detailed paleostress inversion analysis with independent published regional and geochronological constraints. The proposed polyphase brittle tectonic evolution of the SDC includes: (i) an Early Triassic to Early Jurassic NE-SW extension episode (D1); (ii) an Early Cretaceous NW-SE extension event (D2) and (iii) a Miocene to Present ENE-WSW compression (D3). Each brittle deformation phase resulted in additional strain increments that were accommodated by either the formation of neo-formed Andersonian faults or, predominantly, by the reactivation of older and/or inherited structures and rheological anisotropies (e.g., Ramos et al., 2002; Bense et al., 2013a; Martino et al., 2016; Traforti et al., Chapter 2), leading to a long history of structural reactivation.

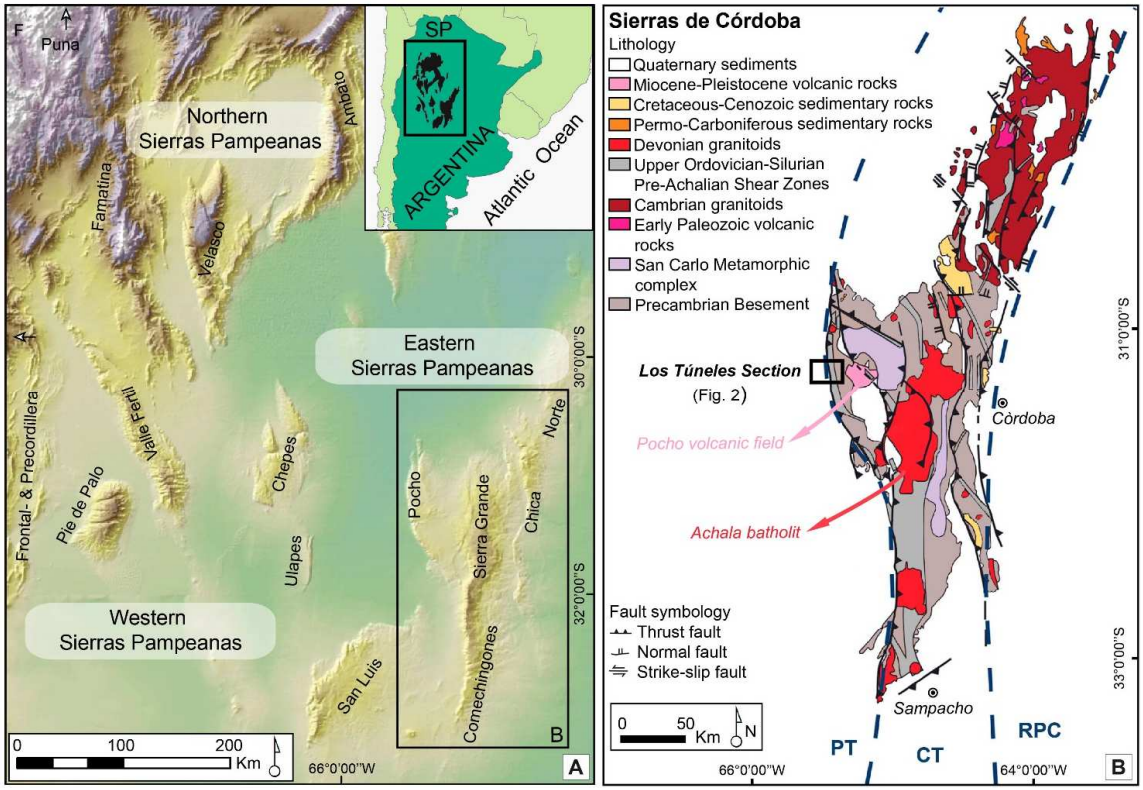

Figure 3.1: *(A) Shaded relief map of the Sierras Pampeanas showing the location of the Northern, Western and Eastern Sierras Pampeanas. Inset and black square show the location of the Sierras Pampeanas (SP) in Argentina and the location of the Sierras de Córdoba, respectively. (B) Simplified geological map of the Sierras de Córdoba modified from Martino (2003) and Richardson et al. (2013). Blue dashed lines indicate the locations of terrane boundaries after Ramos et al. (2002), Rapela et al. (2007) and Richardson et al.*

(2013): Pampia Terrane (PT), Córdoba Terrane (CT) and Rio de la Plata Craton (RPC). Black square outlines the location of Los Túneles section (Figure 3.2).

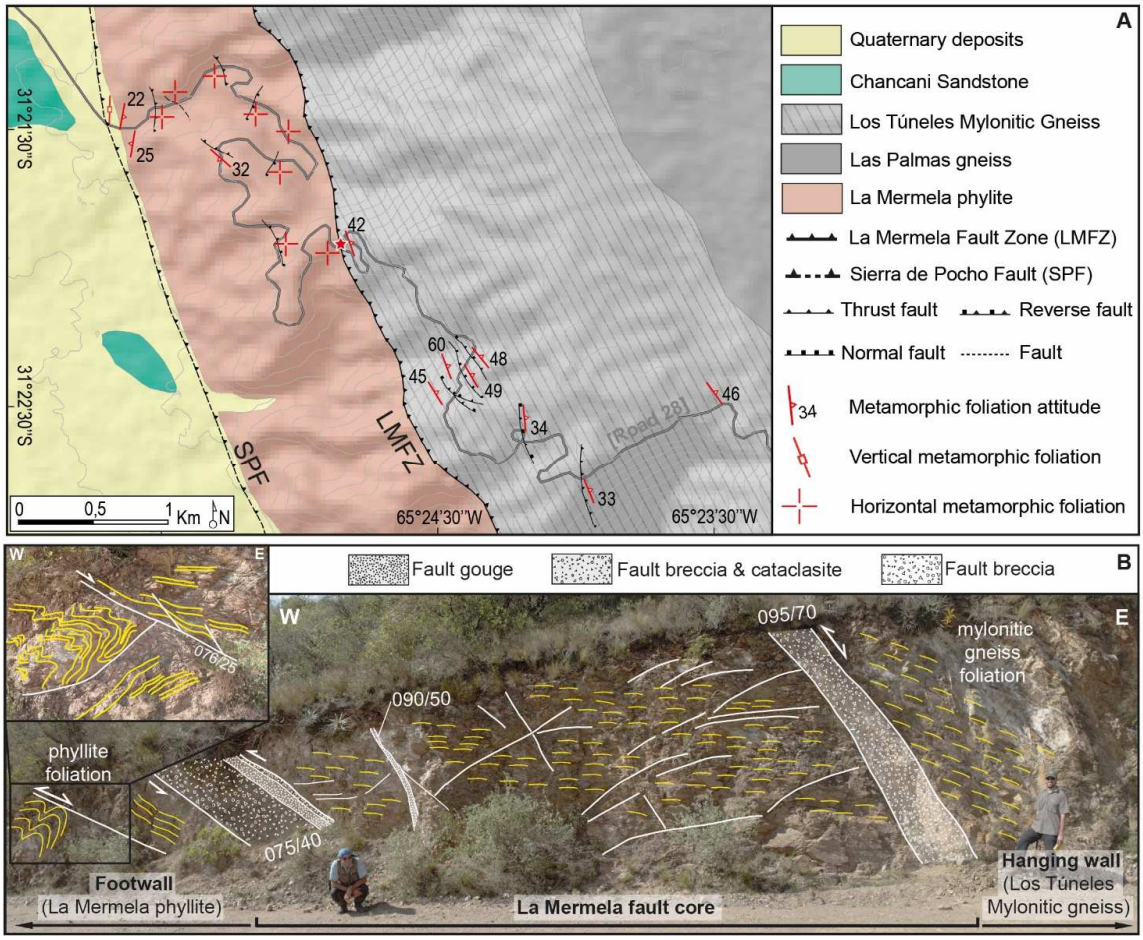

Figure 3.2: *(A) Geological map of the Los Túneles transect. (B) Detailed geological section of the La Mermela Fault Zone separating the Los Túneles Mylonitic gneiss and the La Mermela phyllite. The red star in (A) represents the location of the geological section.*

This study focusses in detail on the brittle deformation of the La Mermela Fault Zone (LMFZ; *Figure 3.1* and *Figure 3.2*), which is a major, east-dipping reverse fault zone juxtaposing the Los Túneles mylonitic gneiss (Bonalumi et al., 1999; Martino 2003) of the hanging wall against the La Mermela phyllite in the footwall. Meso- and micro-structural analysis shows that the footwall and hanging wall rocks (i.e., phyllites and gneisses,

respectively) responded very differently to their common brittle deformation history that took place after their tectonic coupling.

For each of the analyzed rock types, we define the modes of brittle deformation produced by the three distinct tectonic phases, each of which can be considered as a "field-scale triaxial experiment" (*sensu* Bolognesi, 2015) aimed at estimating the upper and lower bounds of the friction coefficient for slip along the foliations (μs) and along pre-existing faults (μf) by applying a stress model based on normalized slip tendency analysis (*sensu* Lisle and Srivastava, 2004). Our results are then used to assess the reliability of the extrapolation of experimental data to large rock volumes.

2 Sierras de Córdoba (SDC): Geological background and tectonic evolution

The SDC are the easternmost range of the ESP and consist of poly deformed Late Neoproterozoic to Early Paleozoic metamorphic sequences, predominantly composed of large migmatitic bodies and Paleozoic granitoids, minor gneisses, amphibolites and marbles (*Figure 3.1B*). High temperature- moderate pressure metamorphism associated with deformation leading to a penetrative, east-dipping metamorphic foliation occurred during the Cambrian Pampean orogeny connected to the collision between the Pampean Terrane and the Rio de la Plata Craton (e.g., Rapela et al., 1998b; Sims et al., 1998; Simpson et al., 2003). Pressure and temperature reached granulite facies conditions leading to widespread anatexis of basement rocks at 7–8 kb and 700–800 °C (e.g., San Carlos Metamorphic Complex in *Figure 3.1B*; Guereschi and Martino, 2014). Low-grade rocks (i.e., La Mermela phyllite) crop out only locally in the western Sierra de Pocho, where they are overthrusted on Carboniferous-Permian continental sedimentary rocks. The Pampean orogeny was followed by the Ordovician-Silurian Famatinian cycle, during which the basement was deformed by east-dipping, greenschist-grade mylonitic to ultramilonitic shear zones referred to as Pre-Achalian shear zones (Martino, 2003; Simpson et al., 2003; Whitmeyer and Simpson, 2003). The shear zones were reactivated in Devonian-Carboniferous times

(Martino, 2003; Steenken et al., 2010) during the Achalian orogeny, which was accompanied by the intrusion of Devonian granitoids (e.g., Achala batholith in *Figure 3.1B*). The tectono-metamorphic evolution and associated ductile deformation of the SDC ceased in the Early Carboniferous (e.g., Whitmeyer, 2008; Bense et al., 2013a, 2013b). Inter-terrane suture zones and intra-terrane shear zones accommodating the Paleozoic orogenies strongly influenced subsequent strain localization and the geometry of faults associated with the Late Permian to Mesozoic extensional deformation events (e.g., Uliana et al., 1989; Schmidt et al., 1995; Ramos et al., 2002). A first extensional episode (D1) was characterized by NE-SW extension (Traforti et al., Chapter 2) and reflects the formation of a Late Paleozoic intracratonic basin (Paganzo Basin; Salfity and Gorustovich, 1984; Mpodozis and Ramos, 1990; Ramos et al., 2002) and the subsequent opening of Triassic to Early Jurassic rift basins (e.g., Ramos and Kay, 1991; Ramos et al., 2002). A second extensional phase (D2) accommodated NW-SE extension (Traforti et al., Chapter 2) during the Early Cretaceous in response to a first stage of the South Atlantic Ocean opening (Schmidt et al., 1995). Finally, Andean deformation began in the Late Cretaceous with the subduction of the Farallon Plate beneath the South American Plate. Between 18 Ma and 12 Ma, subduction of the Juan Fernandez Ridge caused a flattening of the slab between 27° and 33° S (Ramos et al., 2002; Yañez et al., 2001), which resulted in strong mechanical coupling between the subducting Nazca Plate and the upper South American Plate, and caused propagation toward the Andean foreland of Cenozoic magmatism (e.g., Pocho volcanic field) and crustal shortening. Consequently, the extensional fault systems of the SDC were reactivated and inverted. This represents the last brittle tectonic event recorded in the study area (D3) and it is characterized by ENE-WSW shortening direction (Traforti et al., Chapter 2), compatible with the present-day plate convergence (i.e., N 78°E, Vigny et al., 2009).

2.1 La Mermela fault zone

The La Mermela fault zone (LMFZ) is a major, east-dipping reverse fault zone associated with significant westward displacement accommodated by brittle-ductile

deformation. It can be followed along-strike for at least 100 km on the northwest margin of the SDC and shows its best exposures in the Los Túneles area (*Figure 3.1B* and *Figure 3.2*).

The footwall of the LMFZ consists of the La Mermela phyllite (Hünicken and Pensa, 1980), which represents an Early Cambrian (Late Neoproterozoic?) succession of low-grade metasedimentary rocks (Simpson et al., 2003) arguably associated with the accretionary prism of the destructive Early Cambrian margin of Gondwana. These rocks consist of chloritic phyllites deformed by solution cleavage, kink bands and small-scale chevron folds.

The La Mermela fault core (mean attitude 080/60, dip-direction/dip) consists of tabular cataclasite bands and foliated gouges up to several m in thickness, intercalated by up to 2 m thick breccia levels with a subhorizontal fracture cleavage (*Figure 3.2B*). Brittle kinematic indicators indicate both normal and reverse kinematics with a prevalent dip-slip movement.

The immediate LMFZ hanging wall contains a c. 2 km- thick ductile shear zone, referred to as Los Túneles ductile shear zone by Martino (2003) and Los Túneles mylonitic gneiss by Bonalumi et al. (1999), that is directly juxtaposed against the brittle LMFZ. It consists of coarse-grained augen gneiss sheared into mid- to upper-greenschist-grade protomylonites and mylonites. The Túneles ductile shear zone represents a Pre-Achalian shear zone that formed during the Ordovician-Silurian Famatinian orogenetic cycle and that was reactivated and progressively retrogressed during the Achalian orogeny in Devonian-Carboniferous times (Martino, 2003; Steenken et al., 2010). Mylonites are more common down section towards the LMFZ fault contact with the underlying phyllites, above which sheared rocks contain cm-scale pseudotachylyte veins. The latter represents a semi-brittle reactivation of the ductile shear zone (Simpson et al., 2001). Pseudotachylite veins in Los Túneles gneiss were dated by Whitmeyer (2008) to 345 ± 5 Ma and 348 ± 2 Ma ($^{40}Ar/^{39}Ar$ laser ablation analysis)

3 Structural analysis

Our structural analysis focused on the brittle evolution of the LMFZ that has been reconstructed along the Los Túneles road cut (*Figure 3.2*).

3.1 Meso- and microstructural analysis:

The footwall

The footwall phyllites of the LMFZ contain a penetrative sub-horizontal metamorphic foliation, with an average orientation of 237/05, commonly cut by numerous fault planes (*Figure 3.3*A-D). The faults are characterized by tabular, decimetric cataclastic/brecciated bands, usually associated with centimeter to millimeter thick clay gouges, within which illite, chlorite and smectite are the most abundant clay mineral phases (Bense et al., 2013a).

The measured fault sets comprise: (i) NE-SW conjugate faults, dipping steeply to moderately toward the NW or SE, with average attitudes of 292/54 and 117/40 respectively; (ii) NE dipping faults with a mean orientation of 052/46 and (iii) ENE dipping faults, showing a mean orientation of 078/41 (*Figure 3.4*). The kinematics of these faults are normal or inverse (occasionally both kinematics characterize the same fault plane), as clearly indicated by shear sense indicators on the fault planes, secondary shear or tension fractures (*Figure 3.3A and Figure 3.3D*) and drag folds deflecting the metamorphic foliation (*Figure 3.3B*). NE dipping faults represent dip-slip Andersonian faults nucleated during the first NE-SW extension (D1), while NE-SW striking conjugated faults are ascribable to the second NW-SE extension event (D2). All these faults were then reactivated with reverse kinematics during the ENE-WSW Andean compression D3 (*Figure 3.4*). Also the ENE dipping faults bear two sets of striae on the fault planes that are coherent with D1 extension and D3 compression (*Figure 3.4*). In some cases, the sub-horizontal foliation of the phyllites appears to have been reactivated during brittle deformation, as revealed by the formation of centimetric to decimetric subhorizontal bands of cataclasite or breccia along the foliation planes (*Figure 3.3C and Figure 3.3D*), indicating reverse kinematics, similar to what reported by Bellahsen et al. (2016) in the Western Sierras Pampeanas.

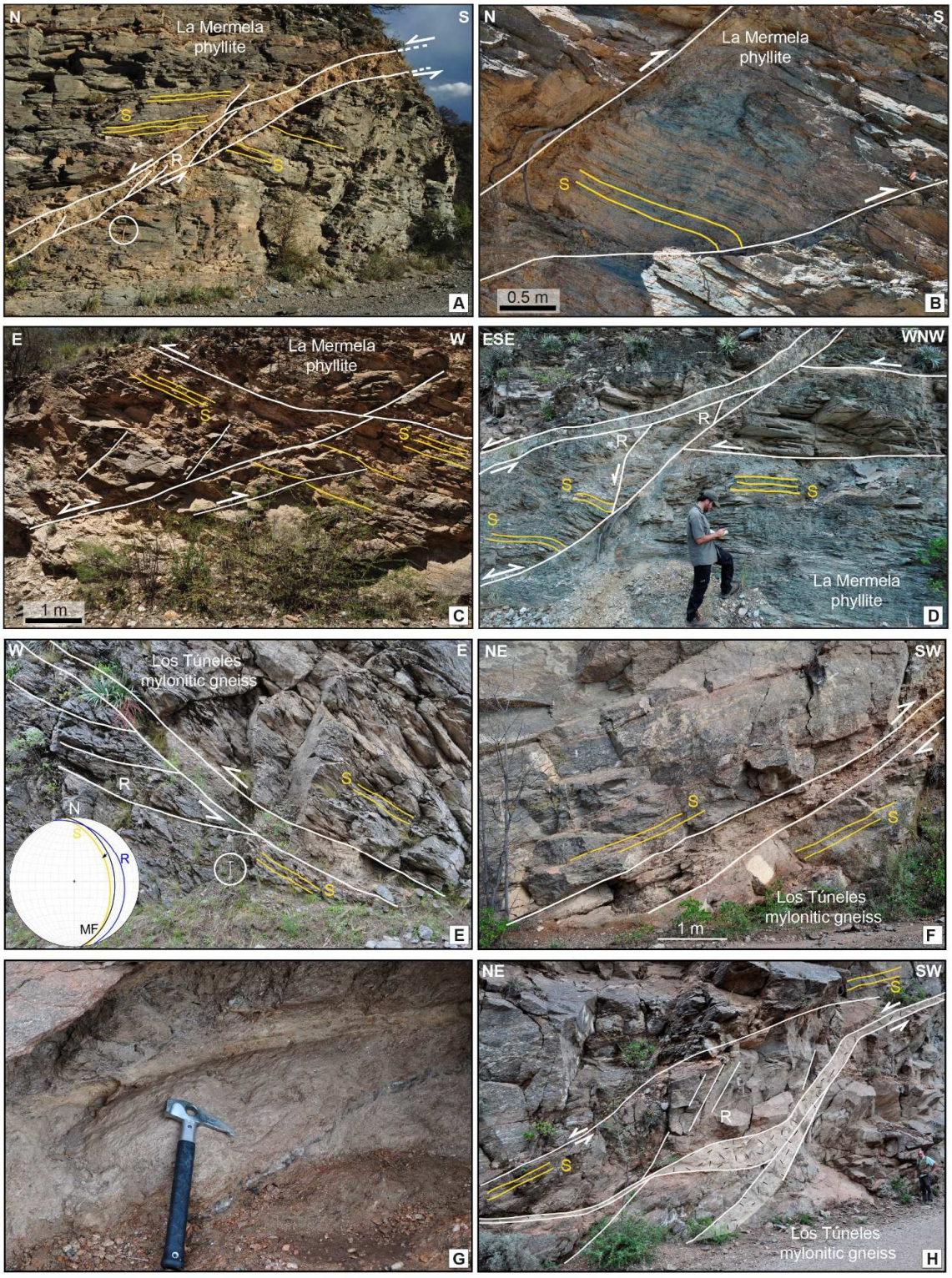
N
S
La Mermela phyllite
S
R
S
A
N
S
La Mermela phyllite
S
0.5 m
B
E
W
La Mermela phyllite
S
S
1 m
C
ESE
WNW
R
R
S
S
S
La Mermela phyllite
D
W
E
Los Túneles mylonitic gneiss
R
S
N
S
R
MF
S
E
NE
SW
S
S
Los Túneles mylonitic gneiss
1 m
F
G
NE
SW
S
R
S
Los Túneles mylonitic gneiss
H

Figure 3.3: *Examples of mesoscopic structural features along the Los Túneles transect. (A) Moderately dipping brittle normal fault cutting sub-horizontal metamorphic foliation in the La Mermela phyllite and associated secondary shear fractures. (B) S-vergent drag fold deflecting the metamorphic foliation in the La Mermela phyllite. (C, D) Brittle thrust faults associated with cataclasite and gouge levels that partially reactivates the sub-horizontal foliation of the La Mermela phyllite. (E, G) Thrust fault reactivating the mylonitic foliation in the Los Túneles mylonitic gneiss. (F) Detail of the foliated fault gouge showed in (G). (H) Anastomosed fault structure associated with a ramp and flat fault geometry in the Los Túneles mylonitic gneiss.*

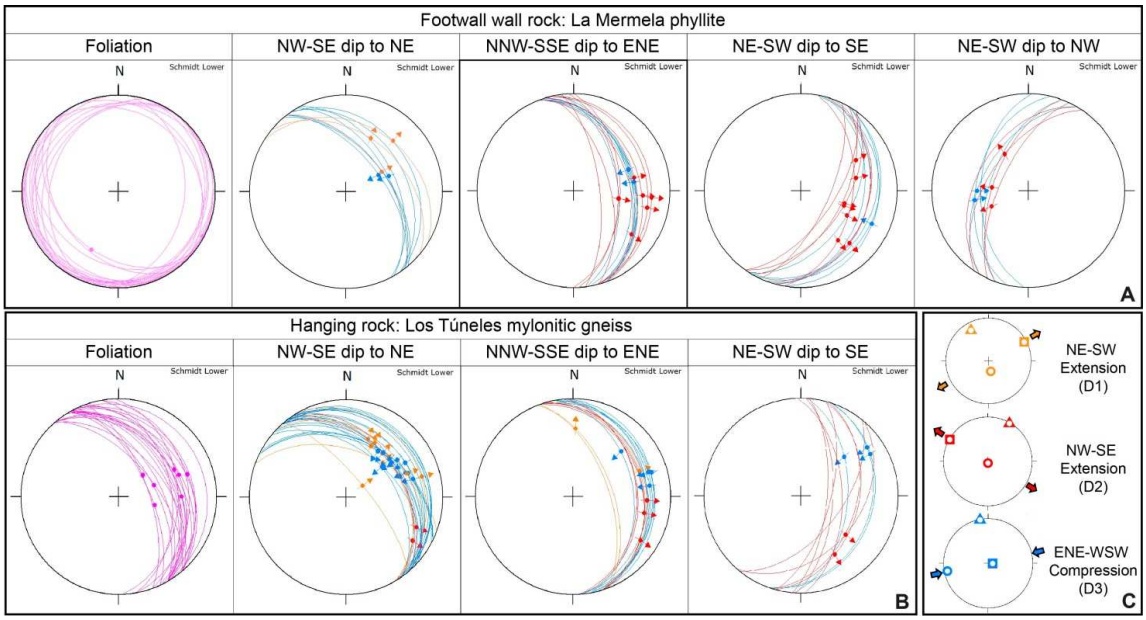

Figure 3.4: *Metamorphic foliation and major fault sets measured at Los Túneles transect in: (A) the La Mermela phyllite (footwall block of the LMFZ) and (B) the Los Túneles mylonitic gneiss (hanging wall block of the LMFZ). Each fault is plotted with colors reflecting the tectonic phase that caused its nucleation or reactivation, as per color key in (C). (C) Mean stress tensor reflecting the three main tectonic phases in the Sierra de Córdoba.*

At the microscale, cataclasites up to 0.5 cm thick occur concordant with the foliation (*Figure 3.5A*) and consist of poorly sorted, angular to rounded clasts of quartz and albite, which appear commonly fractured (*Figure 3.5B*) and are dispersed in a foliated matrix of predominantly chlorite and muscovite. Mica-rich levels in the phyllites do not show clear

evidence of brittle reactivation, but typically contain up to 50 µm thick seams of opaques indicating pressure solution processes (*Figure 3.5B*).

The hanging wall

Along the Los Túneles transect, the LMFZ hanging wall (i.e., the Los Túneles mylonitic gneiss) is dominated by a NNW trending mylonitic foliation (*Figure 3.4*), with an average attitude of 062/43. The mylonites are commonly overprinted by cataclasites and ultracataclasites. During the localization of brittle deformation, the mylonitic sequence was selectively reactivated leading to the formation of decimetric breccia bands, commonly interleaved with centimetric cataclasite and gouge levels (*Figure 3.3E and Figure 3.3H*). Mineralogical analysis performed by XRPD shows illite, chlorite and smectite to be the most abundant clay mineral phases in the gouge (Bense et al., 2013a).

Fault planes measured along the Los Túneles transect can be grouped into three major sets (*Figure 3.4*): (i) NE dipping faults with a mean orientation of 046/36; (ii) ENE dipping faults with a mean orientation of 076/31 and (iii) SE dipping faults, exhibiting some scattering around a mean orientation of 105/49. The NE and ENE dipping fault sets derived from the reactivation of the pervasive mylonitic foliation, which is thus obviously an important factor in controlling the localization of younger brittle deformation. These fault sets bear dip-slip striae that track both extensional and compressive kinematics (i.e., associated with D1 and D3 respectively) as well as oblique-slip striae (i.e., ascribable to D2 extension), and thus document strain increments related to all the three tectonic events that have affected the area (*Figure 3.4*). By contrast, the SE dipping faults that cut the mylonitic foliation represent dip-slip Andersonian faults nucleated during the D2 NW-SE extension and were subsequently reactivated with reverse kinematics by the ENE-WNW D3 compressional phase (*Figure 3.4*).

At the microscale, the mylonitic foliation of the Los Túneles mylonitic gneiss exhibits a typical lepidoblastic texture, with alternating quartz/feldspar bands and anastomosing

phyllosilicate layers containing muscovite, chlorite, and biotite. Incipient brittle

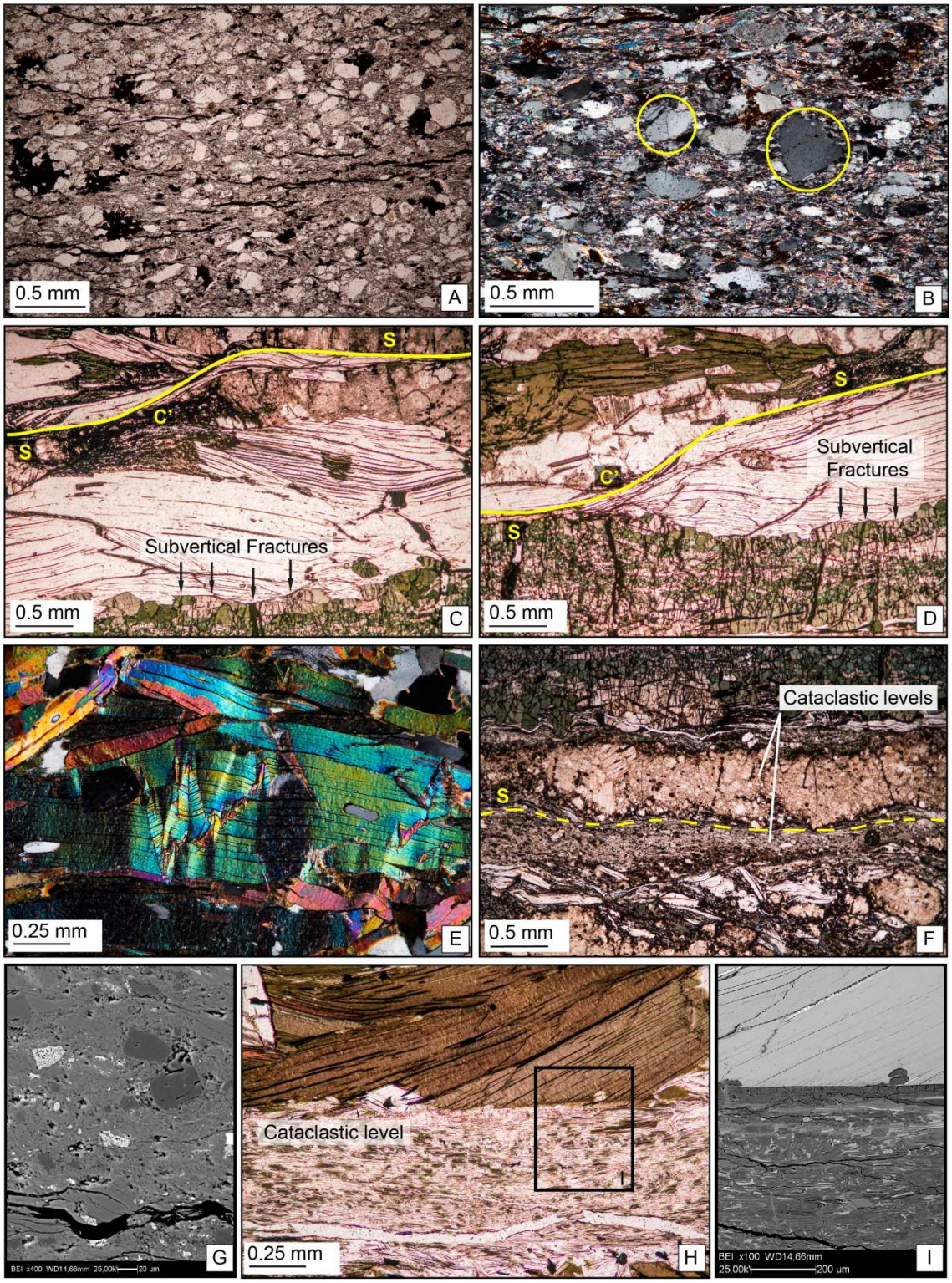

Figure 3.5: *(A) Optical microphotographs (crossed polarizers) of cataclasite layer along foliation of La Mermela Phyllite. (B) Angular to rounded fractured quartz clasts in a mica-rich foliated matrix. (C, D) Optical microphotograph (parallel polarizers) of the Los Túneles Mylonitic Gneiss showing tensional fractures associated with earlier SC' shear bands representing incipient evidence of brittle deformation along foliation planes. (E) Optical microphotograph (crossed polarizers) illustrating micro-kink bands in white mica flakes; (F, H) Optical microphotographs (parallel polarizers) of the Los Túneles Mylonitic Gneiss showing cataclastic levels exploiting and reactivating the primary gneissic foliation. (G, I) SEM-BSE high magnification images of angular clasts belonging to the cataclastic level showed in F and to the foliated cataclasite reported in H, respectively.*

deformation along the foliation planes is evidenced by tensional fractures associated with earlier shear bands (*Figure 3.5C and Figure 3.5D*) and micro- kinking in white mica flakes (*Figure 3.5E*) accommodating slip along (001) cleavage planes (i.e., intragranular micro-kink bands of Shea and Kronenberg 1993, interpreted by Bolognesi and Bistacchi (2016) as the last deformation stage before cataclasis of mica grains). Cataclastic seams along the foliation contain angular to sub-angular clasts, with grainsize ≤ 50 μm, dispersed in a very fine-grained matrix (*Figure 3.5G and Figure 3.5I*). These cataclastic levels increase in frequency, continuity and thickness approaching the LMFZ brittle fault core.

4 Phyllosilicate content and interconnectivity

The mechanical anisotropy typically shown by foliated metamorphic rocks is generally connected to the content and spatial arrangement of the phyllosilicates defining the foliation planes. Phyllosilicate contents ≥ 20-25% accompanied by their strong shape-preferred orientation (SPO) can define a well-developed lepidoblastic fabric controlling the mechanical behaviour of the rock (Bistacchi et al., 2012). In order to estimate the amount of phyllosilicates and visually evaluate their physical interconnectivity to form "easy-glide" continuous layers, we applied image analysis on Back Scattered-Scanning Electron Microscope images (BS-SEM) on representative portions of thin sections of the studied rocks (Appendix 1). The La Mermela phyllite contains between 41 and 45% phyllosilicates (*Figure 3.6*), while the Los Túneles mylonitic gneiss phyllosilicate content is about 45%

(varying between 32 and 60% for the predominantly granoblastic or lepidoblastic domains, respectively; *Figure 3.6*).

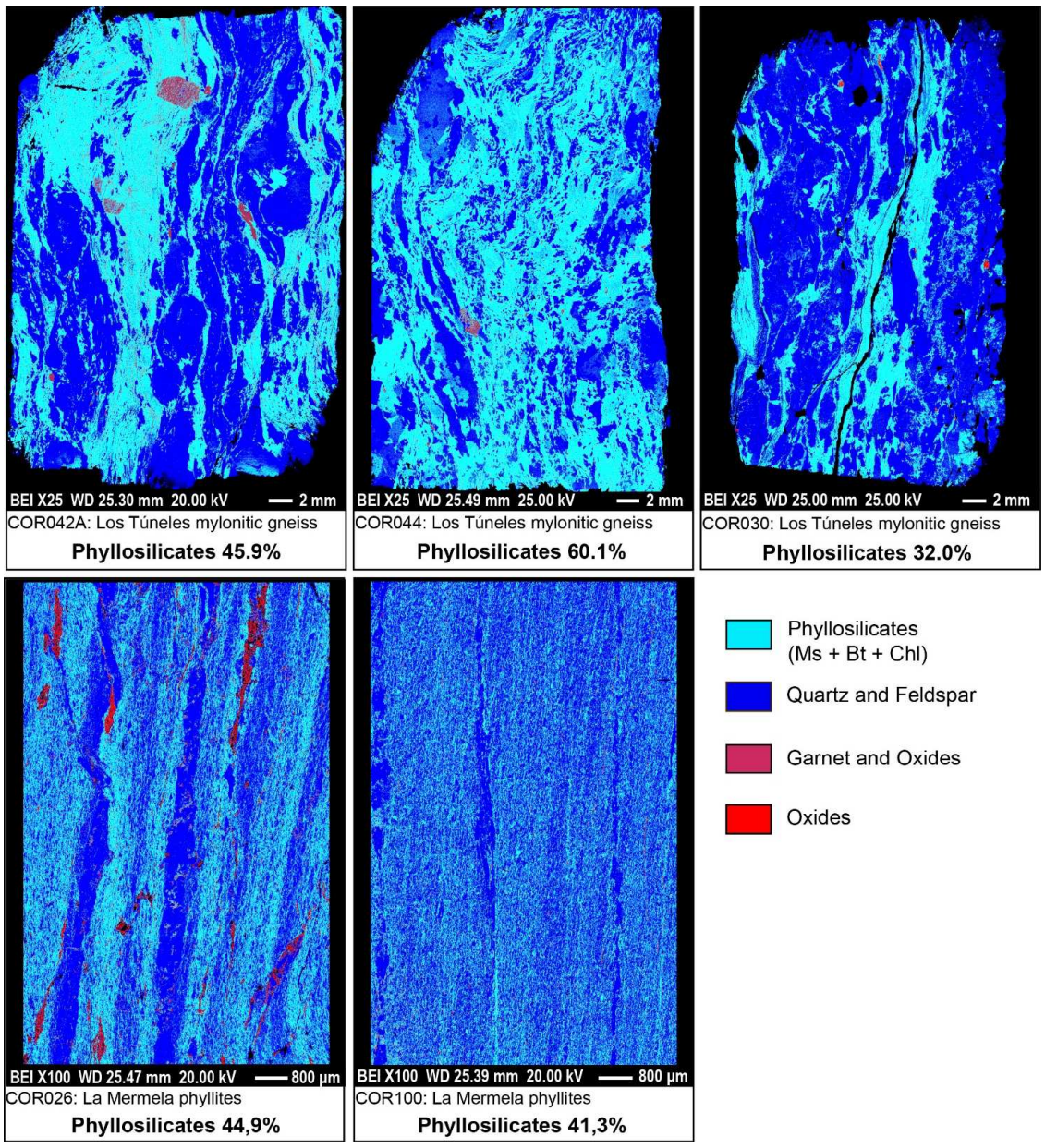

Figure 3.6: Image-analysis on Back Scattered-Scanning Electron Microscope images (BS-SEM) to document the amount of phyllosilicates (reported as % below each image). Different minerals were classified based on their grey scale tones in the image and associated to different color as reported in the legend.

Both lithologies show highly interconnected phyllosilicate layers due to the strong shape-preferred orientation of the contiguous mica flakes (*Figure 3.6*). Within a suitably oriented stress field, the estimated content of phyllosilicate minerals and the observed lepidoblastic fabric represent efficient weakening mechanisms. Moreover, considering that gneisses and phyllites underwent a polyphase brittle evolution, also inherited earlier faults associated with particularly weak fault gouges increased the mechanical anisotropy of the system.

5 Normalised slip tendency analysis

The meso- and microstructural analysis of the studied brittle failure modes revealed that within the study area gneisses and phyllites evolved mechanically very differently during their common brittle deformation history. In more detail, the phyllite foliation was reactivated only during the last compressional phase D3 and was instead cut discordantly by newly-formed Andersonian faults during the first two extensional regimes (D1 and D2); on the other hand, the mylonitic foliation in the gneisses was pervasively reactivated during all tectonic phases (D1, D2 and D3). Considering these observations, in order to constrain possible upper and lower bounds to the friction coefficient for slip along the foliations (μs) and pre-existing faults (μf), we applied the normalized slip tendency analysis (Lisle and Srivastava, 2004) calculated as:

$$\boldsymbol{NTs} = \frac{\boldsymbol{Ts}}{\boldsymbol{Max(Ts)}} = \frac{\boldsymbol{\tau}}{\boldsymbol{\sigma_n}} \cdot \frac{\mathbf{1}}{\boldsymbol{\mu_0}}$$

where *Ts* is the slip tendency defined by Morris et al. (1996) as $Ts = \tau / \sigma_n$ (τ and σ_n are the tangential and normal stress, respectively), *Max(Ts)* is the maximum slip tendency (i.e., $Max(Ts) = \tau_{critical} / \sigma_n = \mu$, where $\tau_{critical}$ is the maximum tangential stress on a surface with friction coefficient μ), and μ_0 is the average friction coefficient for pristine crustal rocks, which is equal to 0.7 (e.g., Sibson, 1985). If simultaneous failure on both the inherited mechanical discontinuities (foliation or pre-existing fault) and new Andersonian faults

occurs, the relationship between μs or μf and μ_0 can be expressed as: $\mu s \text{ (or } \mu f) = NTs \cdot \mu_0$, where *NTs* represents the normalized slip tendency of the analyzed discontinuity (*Figure 3.7A*). If mechanical anisotropies are not reactivated and new Andersonian faults nucleate (*Figure 3.7B*), a lower bound to μs and μf can be defined for $\mu s \text{ (or } \mu f) > NTs \cdot \mu_0$. By contrast, when only reactivation of existing foliation/faults is observed (i.e. no newly-formed Andersonian faults are recognised) an upper bound to μs and μf can be estimated as: $\mu s \text{ (or } f) < NTs \cdot \mu_0$ (*Figure 3.7C*). All together these conditions allow to derive a solid constraint to μs and μf.

Additionally, in order to apply the normalised slip tendency approach, we need to know the reduced stress tensor parameters associated with each brittle deformation event characterized during the meso- and micro-structural study. To this purpose, we refer to the paleostress field reconstruction by Traforti et al. (Chapter 2). Traforti et al. carried out palaeostress inversion at the regional scale from mesoscopic faults in the Sierra de Córdoba (including faults from both hanging wall and footwall of the LMFZ) and produced several reduced stress tensors, which have been assigned to the reconstructed tectonic phases (D1, D2 and D3 *Figure 3.8*). The average orientation and the statistical dispersion of the data have been calculated for each stress axis orientation using the bootstrap approach (see details in Traforti et al., Chapter 2). As a result, the calculated mean stress tensors (*Figure 3.8*) show a 95% confidence interval from bootstrapping (given in delta form) of about 6,5° for each stress axis of D1, D2 and D3 events (see details in Traforti et al., Chapter 2). Additionally, the 95% confidence interval of the stress ratio R (i.e., $R = (\sigma_2-\sigma_3)/(\sigma_1-\sigma_3)$, Angelier 1990) is 0.1 for all the tectonic phases (see details in Traforti et al., Chapter 2). Therefore, during the normalised slip tendency analysis, the mean paleostress tensors obtained by Traforti et al., Chapter 2) have been considered with an uncertainty of ± 6,5° for the mean stress axis orientations and ± 0.1 for the R values.

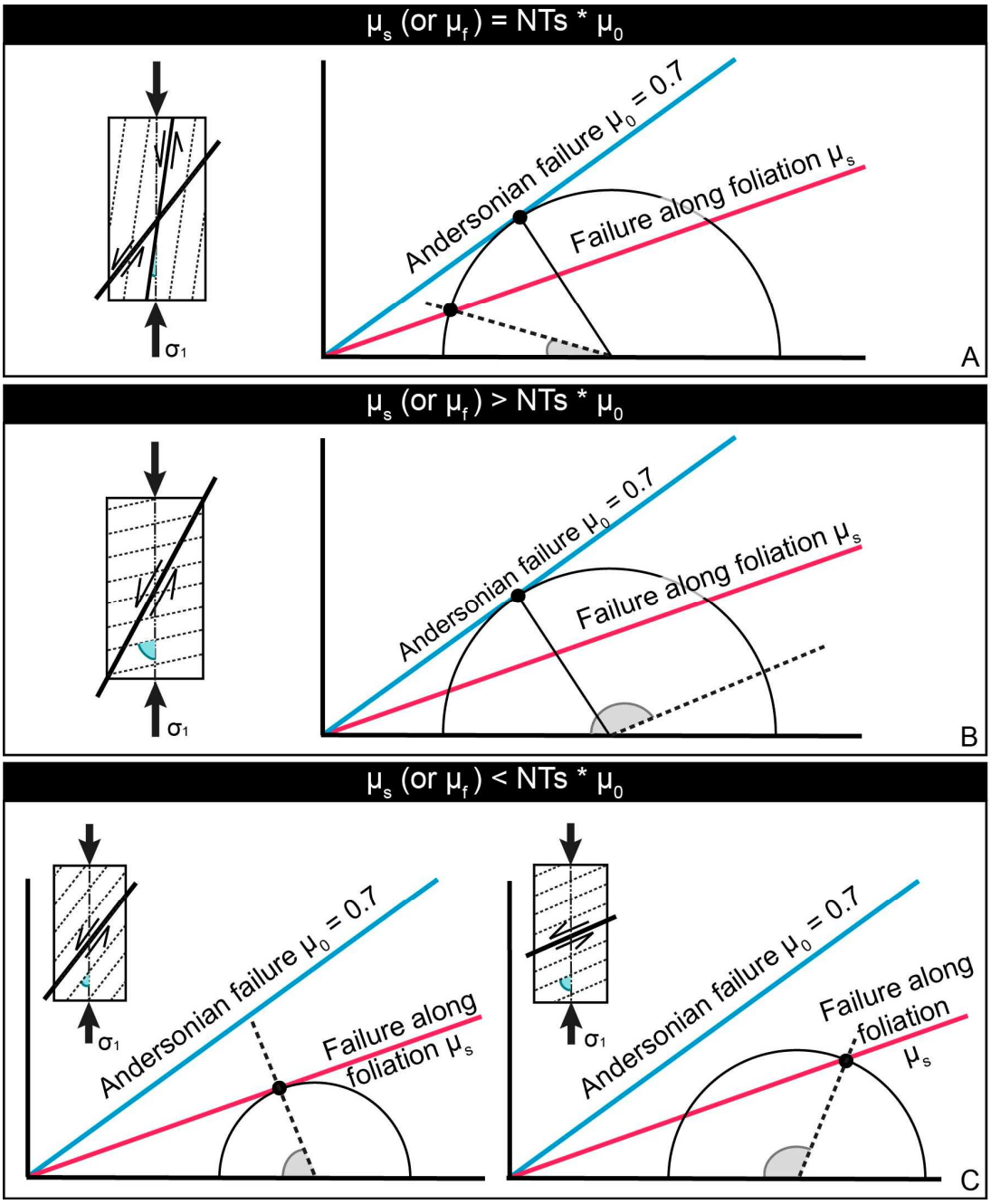

Figure 3.7: *Conceptual diagram illustrating the three different brittle failure modes and the associated Normalised Slip Tendency analysis aimed at: (A) estimating the value of the friction coefficient for slip along foliations (μs) and along pre-existing faults (μf), (B) estimating the lower bound to the of the friction coefficient μs and μf and (C) estimating the upper bound to the of the friction coefficient μs and μf. Each failure scheme reports in light blue the angle τ, while each Mohr diagram displays in grey the angle 2·τ, where τ is the angle between σ_1 and the plane of discontinuity.*

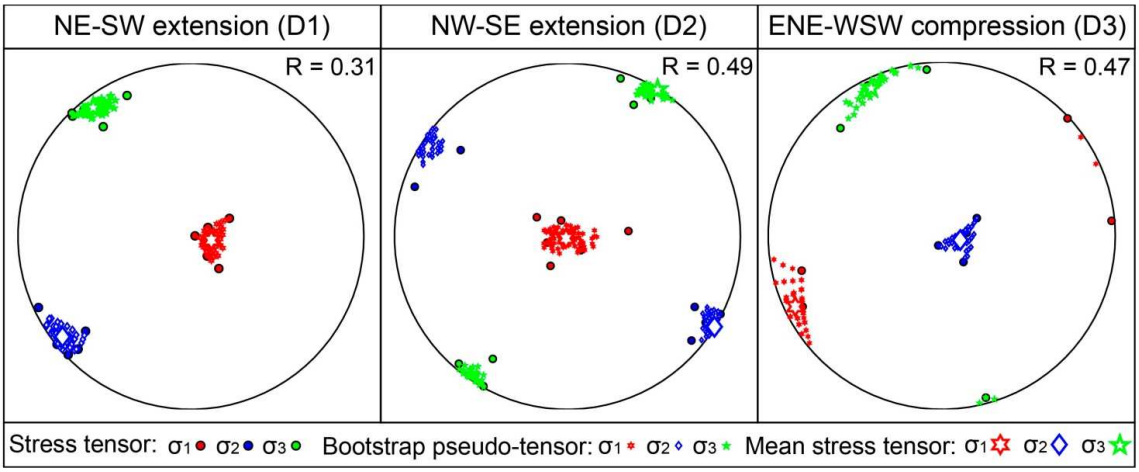

Figure 3.8: *Mean stress tensor calculated for each of the tectonic phases that characterize the polyphase brittle evolution of the Sierras de Córdoba. Each plot also reports the bootstrap pseudo-tensors allowing to estimate the 95% confidence interval for each mean stress axis orientation.*

6 Results

Figure 3.9 presents three examples of the performed normalised slip tendency analysis, each representing one of the conditions outlined in Figure *3.7*.

In *Figure 3.9A* we consider the deformation of the La Mermela phyllite during the NW-SE extensional phase, for which no reactivation of pre-existing NE dipping normal faults occurred, while new, NW dipping, Andersonian normal faults nucleated (stereoplots on the left in *Figure 3.9A*). The observations from our mesoscopic field analysis are indeed in agreement with the normalized slip tendency analysis (Schmidt and Mohr plot in *Figure 3.9A*), which yielded an NTs close to the maximum value of 1 (0.98) for the newly formed Andersonian fault set and a low NTs value of 0.37 for the highly misoriented pre-existing fault set. As the conditions to estimate the lower bound to the friction coefficient for slip along pre-existing faults (μf) are met (i.e., mechanical anisotropies are not reactivated and

new Andersonian faults nucleate, *Figure 3.7A*), the friction coefficient along NE dipping inherited fault set can be estimate to be greater than 0.26 ($\mu f > NTs \cdot \mu_0 > 0.37 \cdot 0.7 > 0.26$).

Figure 3.9B reports the normalised slip tendency analysis performed considering the deformation of the gneiss in the LMFZ hanging wall during the NW-SE extensional phase. In this case both the reactivation of pre-existing normal faults (NE dipping faults with NTs = 0.36) and the nucleation of new Andersonian faults (SE dipping normal faults with NTs = 0.91) have been observed in the field. Therefore the conditions to estimate the friction coefficient for slip along pre-existing faults (μf) are satisfied (*Figure 3.7B*) and the normalised slip tendency analysis results allow to constraint the value of μf along the NE dipping pre-existing faults in the gneisses to be about 0.25 ($\mu f = 0.36 \cdot 0.7 = 0.25$).

Finally, *Figure 3.9C* represents the deformation of the LMFZ hanging wall gneiss during the ENE-WSW compressional phase. In this phase, all the pre-existing normal fault sets and the mylonitic foliation were reactivated while no new Andersonian faults (i.e., related to this last deformational event) were observed in the field. These observations in turn permit the upper bound to the friction coefficient for slip along pre-existing faults to be estimated (*Figure 3.7C*), which results to be $\mu f < 0.56$ ($\mu f < 0.8 \cdot 0.7 < 0.56$) and $\mu f < 0.41$ ($\mu f < 0.58 \cdot 0.7 < 0.41$) for the NE and SE dipping normal fault sets, respectively (*Figure 3.9C*).

The normalised slip tendency analysis has been carried out for each tectonic phase considering all the fault sets and the metamorphic foliations measured in the LMFZ hanging wall gneisses and footwall phyllites. Subsequently, the normalised slip tendency results have been interpreted using the rationale illustrated in *Figure 2.9*. Histograms in *Figure 3.10* summarize the estimated friction coefficient along pre-existing faults (μf) and foliation planes (μs) calculated for the gneisses and phyllites based on the normalised slip tendency

results. The reported error bars reflect the uncertainty of ± 6,5° in mean stress axis orientations and of ± 0.1 for the R values of the computed paleostress tensors.

In the case of LMFZ hanging wall gneiss, the friction coefficient μs_{gneiss} for slip along the mylonitic foliation was constrained to ≈ 0.33 ± 0.04 (*Figure 3.10A*). The friction coefficient μf for slip along inherited faults reactivating the metamorphic foliation is ≈ 0.25 ± 0.01 (second histogram in *Figure 3.10A*). In fact, this estimated μf value is constrained by considering inherited normal faults that were initially activated exploiting the mylonitic foliation during the first NE-SW extensional phase and then reactivated by the subsequent tectonic events (NW-SE extension D2 and ENE-WSW compression D3). This accounts for the low value of the estimated friction coefficient (i.e., μf ≈ 0.25). Additionally, the normalised slip tendency results allow to constrain the friction coefficient for slip along inherited faults cutting the metamorphic foliation to values lower than 0.48 (third histogram in Figure 3.10A).

Considering the LMFZ footwall phyllite, the friction coefficient μsphyllite along the metamorphic foliation was constrained to ≈ 0.2 ± 0.1 (*Figure 3.10B*), while the friction coefficient μf for slip along inherited faults cutting the metamorphic foliation is ≈ 0.4 ± 0.15; (*Figure 3.10B*).

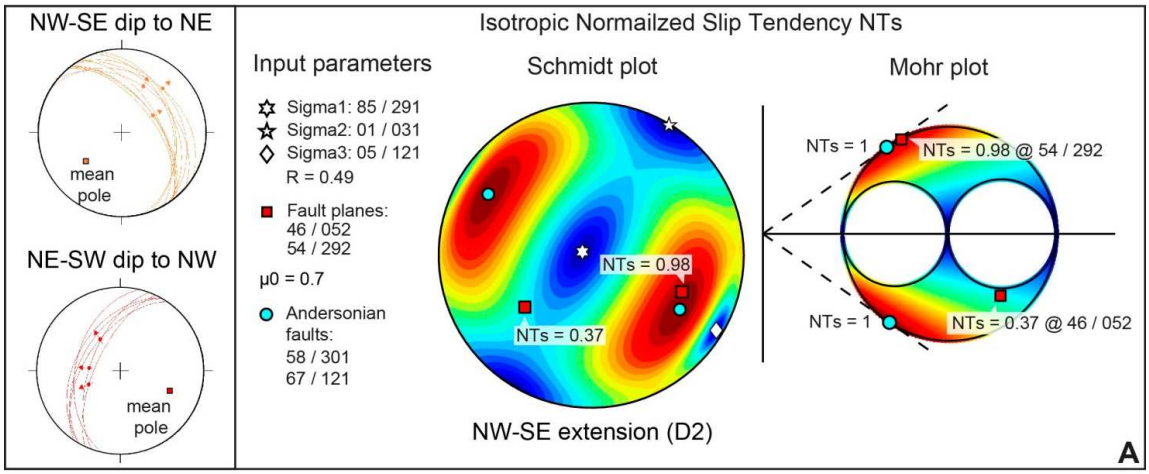

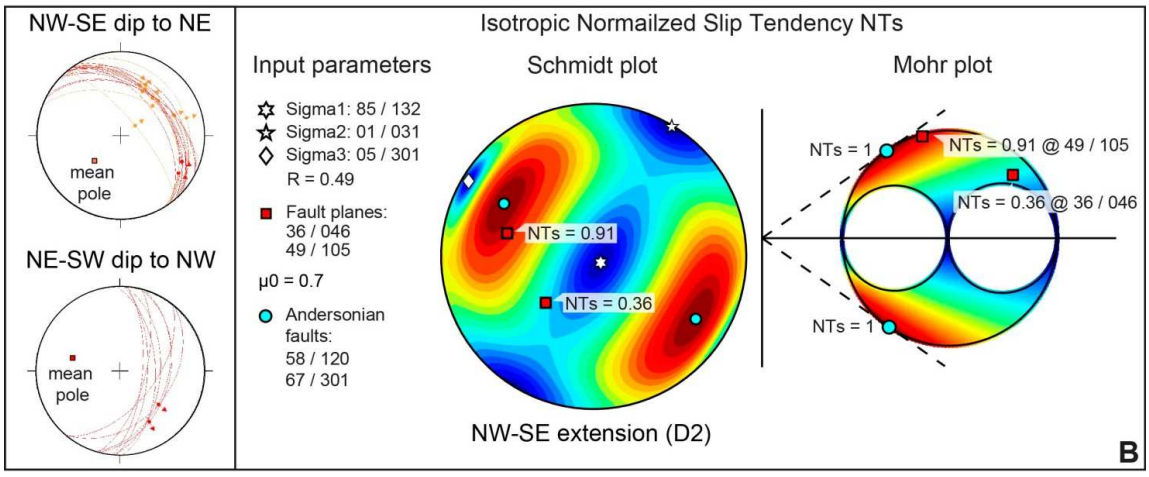

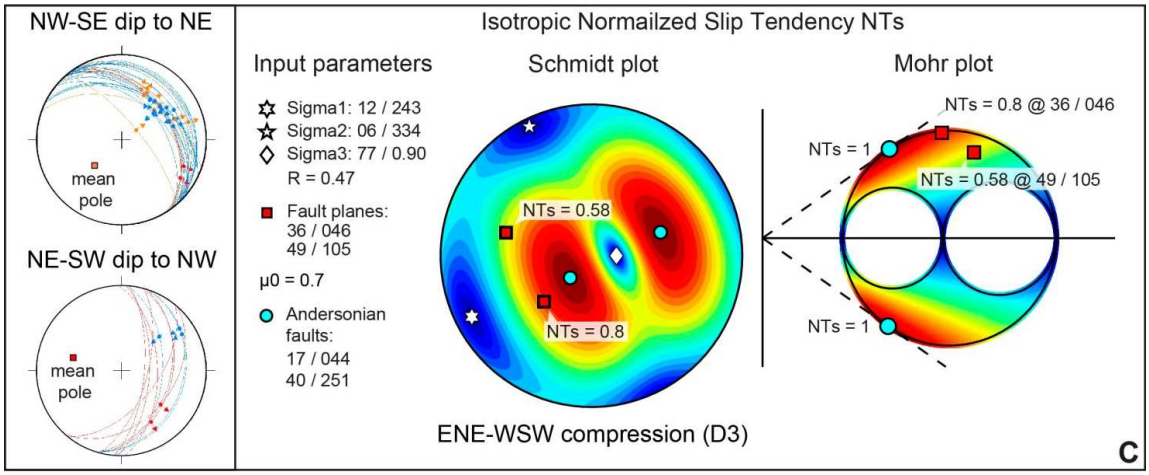

Figure 3.9: *Examples of the normalised slip tendency analysis performed in this study by considering the three conditions expressed in Figure 3.7. For each example, the left square reports the tested fault sets, while the right square shows the input parameters and the*

normalised slip tendency result plotted in the Schmidt and Mohr plot. See the main text for detailed explanation of the examples for: (A) Estimation of the lower bound to the friction coefficient along inherited NE dipping faults in phyllite, (B) Estimation of the friction coefficient along inherited NE dipping faults in gneiss and (C) Estimation of the upper bound to the friction coefficient along inherited NE and SE dipping faults in gneiss.

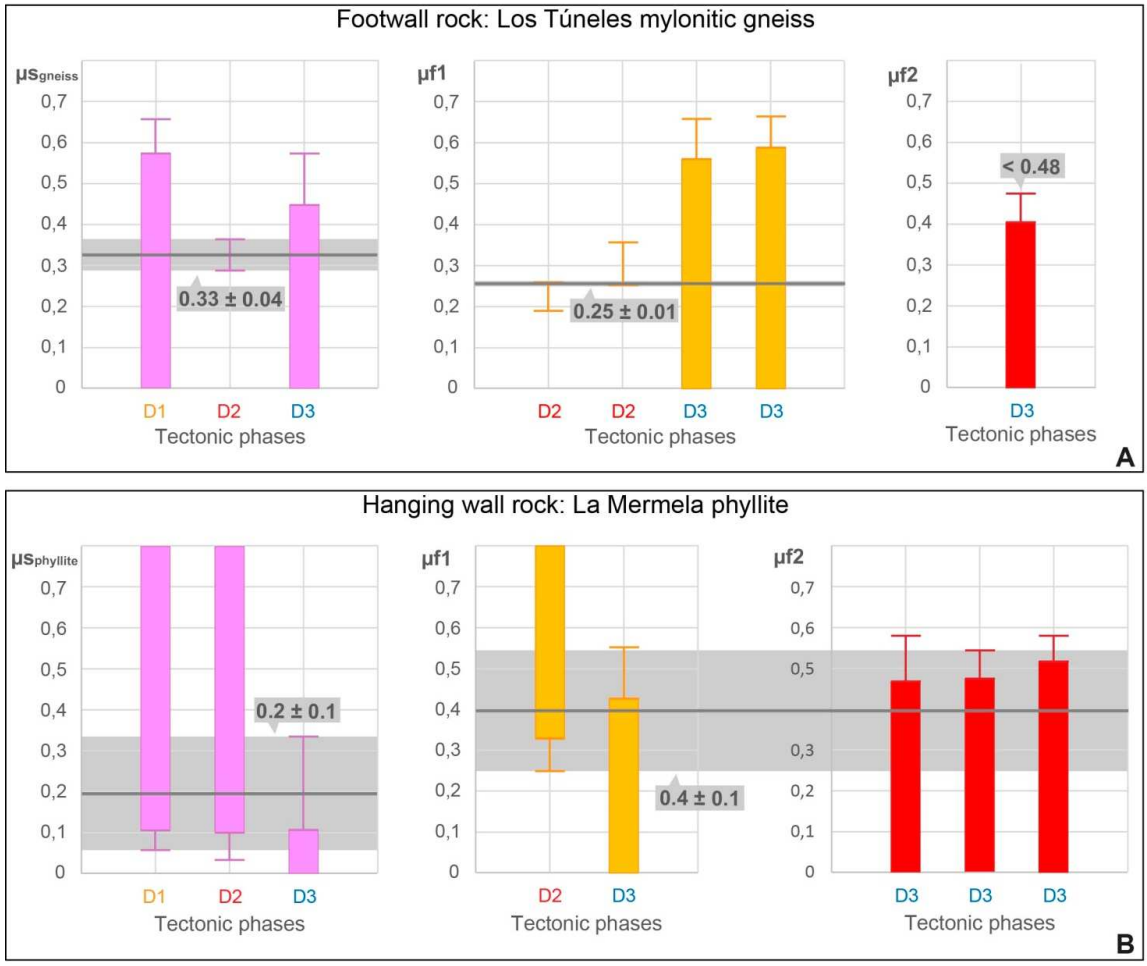

Figure 3.10: *Histograms summarizing the estimate of the friction coefficient value along pre-existing faults (μf) and foliation planes (μs) calculated for gneiss (A) and phyllite (B) on the basis of the normalised slip tendency analysis results. Histogram bars (with associated error bars) descending from the top of the diagram represent estimate of friction coefficient lower bounds, while histogram bars ascending from the diagram bottom express friction coefficient upper bounds. When only the error bar is reported the value of the friction coefficient has been estimated (± error). Dark grey lines represent the general inferred μf or μs values, which are associated to an error represented by light grey bands.*

7 Discussion

The general low values of the estimated friction coefficient for slip along foliations (μs) and along pre-existing faults (μf) in phyllosilicate-bearing rocks account for an absolute weakness mechanism (Rice, 1992), as failure along these inherited mechanical discontinuities develops at lower differential stresses than those required to reach the Andersonian failure envelope.

Additionally, it is noteworthy that our results match well the extremely low friction coefficients (μ=0.2–0.4) for slip parallel to the foliation in phyllosilicate-rich rocks determined in previous studies (see Bistacchi et al., 2012 for a review of mechanical anisotropy data of foliated rocks). The estimated friction coefficient for slip along the mylonitic foliation in gneiss, $\mu s_{gneiss} \approx 0.33 \pm 0.04$ and $\approx 0.25 \pm 0.01$ (considering inherited faults exploiting the mylonitic foliation), is in agreement with the values estimated by Bolognesi and Bistacchi (2015) for the reactivated mylonitic foliation of the Simplon Line in the Western Alps (i.e., 0.25 ± 0.1); while the estimated friction coefficient for slip along the phyllite foliation planes ($\mu s_{phyllite} \approx 0.2 \pm 0.1$) is slightly lower than those derived for the same rock type from laboratory experiments (e.g., ca. 0.35 in Donath 1972). We estimated the friction coefficient for slip along pre-existing gouge-bearing faults across foliation to be lower than ~ 0.48, for the mylonitic gneiss, and equal to 0.4 ± 0.1 for the phyllite. These values are coherently lower than the friction coefficient for fracturing across the foliation (ca. 0.65) resulting from laboratory experiments on phyllites (e.g., Donath 1972) and gneisses (e.g., Agliardi et al., 2014). Moreover, these results are in agreement with the frictional properties outlined by a wealth of experiments on natural fault gouges (e.g., $\mu \approx 0.2 - 0.4$ for clay-rich fault gouge investigated by Numelin et al., 2007 and $\mu \approx 0.31 - 0.25$ for phyllonite analyzed by Collettini et al., 2009).

The overall consistency between the friction coefficient values derived from our slip tendency analysis and from laboratory experiments allows some useful considerations as

to the extrapolation potential of laboratory data. The internal friction coefficients retrieved by laboratory experiments are found to be indeed representative also for the mechanical behaviour of inherited discontinuities at a regional scale. In addition, the slip tendency approach applied here allows to derive results that account for the variability associated to the mechanical complexities typically present at a regional scale (i.e., 10^4-10^3 m), as it is based on the combination of mesoscale characterization of brittle failure modes and paleostress analysis. On the other hand, for the slip tendency approach to be possible, it is necessary to have well-constrained paleostress inversion results (i.e., Traforti et al, Chapter 2), which is not always possible.

8 Conclusions

In this contribution, we have studied the effects of the intrinsic mechanical anisotropy of phyllosilicate bearing rocks, which can be ascribed to the presence of pervasive metamorphic foliations and inherited gouge bearing faults. To this purpose, we have considered the polyphase brittle deformation history of the La Mermela Fault Zone (Sierras de Córdoba, Central Argentina), which from the Early Triassic onwards encompasses three well-constrained brittle deformational events, each of which resulted in strain increments accommodated by the formation of neo-formed faults or, predominantly, by the reactivation of inherited discontinuities.

We analyzed the hanging wall and the footwall of the La Mermela Fault Zone (mylonitic gneisses and phyllites, respectively) aiming at characterizing the style of brittle deformation accommodated by the different lithologies during the polyphase deformation. For each deformation phase, we conceptualized a “field-scale triaxial experiment” by considering the corresponding paleostress field and we derived the friction coefficient for

slip along the foliations (μs) and along pre-existing faults (μf) by applying a stress model based on the normalized slip tendency (NTs) analysis (Lisle and Srivastava, 2004).

Applying this analysis to the multiple deformation phases of the La Mermela Fault Zone we were able to estimate: (i) the friction coefficient for slip along the gneiss mylonitic foliation (μs_{gneiss}) to be between values of ~ 0.33 ± 0.04 and 0.25 ± 0.01 (considering inherited faults exploiting the mylonitic foliation); (ii) the friction coefficient for slip along phyllite foliation ($\mu s_{phyllite}$) to be ~ 0.2 ± 0.1 and (iii) the friction coefficient for slip along pre-existing gouge bearing faults cutting across the foliation (μf) to be lower than 0.48 for mylonitic gneiss and equal to 0.4 ± 0.1 for phyllite. Given that these values are in agreement with the mechanical anisotropy data obtained independently from laboratory deformation tests, the normalised slip tendency analysis, integrated with detailed meso- and micro-structural observations, can be considered a reliable method to investigate and constrain the weakness of pre-existing anisotropies at a regional scale (10^4-10^3 m), which, in turn, represents a first-order factor steering the strength and deformation style of crustal blocks and complex faults.

Acknowledgments

Patricia Alvarado and the seismotectonics re 415 search group of the University of San Juan (AR) and CIGEOBIO-CONICET are warmly thanked for logistics and technical support during our stay in Argentina. In particular, we are grateful to Agostina Lia Venerdini, Yamila Dubokivic and Gustavo Ortiz for the assistance provided during the field work. The authors thank L. Tauro and E. Masiero (thin section preparation), F. Zorzi (XRPD analysis). Slip tendency analysis and tensor averaging with bootstapping was performed with applications developed by Andrea Bistacchi (andrea.bistacchi@unimib.it). This research was funded by the Università degli Studi di Padova, Scientific Research funds, part EX 60% 2014-2015 and DOR 2016, and by the European Research Council Consolidator Grant Project (NOFEAR) No 614705.

References

Agliardi, F., Zanchetta, S., Crosta, G. B., 2014. Fabric controls on the brittle failure of folded gneiss and schist. Tectonophysics 637, 150–162, doi:10.1016/j.tecto.2014.10.006.

Angelier, J., 1990. Inversion of field data in fault tectonics to obtain the regional stress. III. A new rapid direct inversion method by analytical means. Geophysical Journal International 103, 363–376.

Attewell, P.B., Sandford, M. R., 1974. Intrinsic shear strength of a brittle, anisotropic rock I: experimental and mechanical interpretation. International Journal of Rock Mechanics and Mining Science & Geomechanics Abstracts 11, 423–430.

Bell, F.G., Coulthard, J.M., 1997. A survey of some geotechnical properties of the Tees Laminated Clay of central Middlesbrough, North East England. Engineering Geology 48, 117–133.

Bellahsen, N., Sebrier, M., Siame, L., 2016. Crustal shortening at the Sierra Pie de Palo (Sierras Pampeanas, Argentina): near-surface basement folding and thrusting. Geological Magazine 153(5–6), 992–1012, doi:10.1017/S0016756816000467.

Bense, F.A., Wemmer, K., Löbens, S., Siegesmund, S., 2013a. Fault gouge analyses: K–Ar illite dating, clay mineralogy and tectonic significance–a study from the Sierras Pampeanas, Argentina. International Journal of Earth Sciences 103, 189–218, doi:10.1007/s00531-013-0956-7.

Bense, F. A., Löbens, S., Dunkl, I., Wemmer, K., Siegesmund, S., 2013b, Is the exhumation of the Sierras Pampeanas only related to Neogene flat-slab subduction? Implications from a multi-thermochronological approach. Journal of South American Earth Sciences 48, 123–144, doi:10.1016/j.jsames.2013.09.002.

Bistacchi, A., Massironi, M., Menegon, L., Bolognesi, F., Donghi, V., 2012. On the nucleation of non-Andersonian faults along phyllosilicate-rich mylonite belts. Geol. Soc. Lond. Spec. Publ. 367, 185-199, doi:10.1144/SP367.13.

Bolognesi, F., 2014. Brittle deformation in phyllosilicate-rich mylonites: implication for failure modes, mechanical anisotropy, and fault weakness. Ph.D. thesis, University of Milano Bicocca.

Bolognesi, F., Bistacchi, A., 2016. Weakness and mechanical anisotropy of phyllosilicate-rich cataclasites developed after mylonites of a low-angle normal fault (Simplon Line, Western Alps). Journal of Structural Geology 83, 1–12, doi:10.1016/j.jsg.2015.11.009.

Bonalumi, A., Martino, R., Baldo, E., Zarco, J., Sfragulla, J., Carignano, C., Kraemer, P., Escayola, M., Tauber, A., 1999. Hoja Geológica 3166-IV, Villa Dolores, Provincias de Córdoba, La Rioja y San Luis. Instituto de Geología y Recursos Minerales, Servicio Geológico Minero Argentino, Buenos Aires, Boletín 250, 123.

Collettini, C., Niemeijer, A., Viti,C., Marone,C., 2009. Fault zone fabric and fault weakness. Nature 462, 907–911.

Crider, J. G., 2015. The initiation of brittle faults in crystalline rock. Journal of Structural Geology 77, 159–174.

Donath, F. A., 1961. Experimental study of shear failure in anisotropic rocks. Geological Society of America Bulletin 72, 985–990.

Donath, F. A., 1972. Effects of cohesion and granularity on deformational behavior of anisotropic rocks. Geological Society of America Memoirs 135, 95–128.

Duveau, G., Shao, J. F., Henry, J. P., 1998. Assessment of some failure criteria for strongly anisotropic materials. Mechanics of Cohesive-Frictional Materials 3, 1–26.

Gordillo, C., 1984. Migmatitas cordieríticas de las Sierras de Córdoba; condiciones físicas de la migmatización. Academia Nacional de Ciencias, Córdoba, 68, 1–40.

Guereschi, A.B., Martino, R.D., 2014. Las migmatitas de las Sierras de Córdoba. In: Martino, R.D., Guereschi, A.B. (Ed.) Geología y Recursos Naturales de la Provincia de Córdoba. Relatorio del 19º Congreso Geológico Argentino, Asociación Geológica Argentina, Córdoba, 67–94.

Holdsworth, R.E., van Diggelen, E.W.E., Spiers, C.J., de Bresser, J.H.P., Walker, R.J., Bowen, L., 2011. Fault rocks from the SAFOD core samples: Implications for weakening at shallow depths along the San Andreas Fault, California. Journal of Structural Geology 33, 132-144, doi:10.1016/j.jsg.2010.11.010.

Hünicken, M., Pensa, M., 1980. Estratigrafía y tectónica de las sedimentitas neopaleozoicas (Fm. Chancaní) y de las filitas (Fm. La Mermela) del borde occidental de las Sierras de Pocho y Guasapampa. Actas Academia Nacional de Ciencias, Córdoba, 53, 255–286.

Jaeger, J.C., Cook, N.G.W., Zimmerman, R.W., 2007. Fundamentals of Rock Mechanics, fourth ed. Wiley-Blackwell.

Knight, R.D., Klassen, R.A., Hunt, P., 2002. Mineralogy of fine-grained sediment by energy-dispersive spectrometry (EDS) image analysis - A methodology. Environmental Geology 42(1), 32–40, doi:10.1007/s00254-002-0538-7.

Kronenberg, A.K., Kirby, S.H., Pinkston, J., 1990. Basal slip and mechanical anisotropy of biotite. Journal of Geophysical Research 95, 19257, doi:10.1029/JB095iB12p19257.

Lisle, R.J., Srivastava, D.C., 2004. Test of the frictional reactivation theory for faults and validity of fault-slip analysis. Geology 32, 569, doi:10.1130/ G20408.1.

Mariani, E., Brodie, K.H., Rutter, E.H., 2006. Experimental deformation of muscovite shear zones at high temperatures under hydrothermal conditions and the strength of phyllosilicate-bearing faults in nature. Journal of Structural Geology 28, 1569–158, doi:10.1016/j.jsg.2006.06.009

Martino, R.D., 2003. Las fajas de deformación dúctil de las Sierras Pampeanas de Córdoba: Una reseña general. Revista de la Asociación Geológica Argentina 58, 549–571.

Martino, R. D., Guereschi, A. B., Caro Montero, A., 2016. Reactivation, inversion and basement faulting and thrusting in the Sierras Pampeanas of Córdoba (Argentina) during Andean flat-slab deformation. Geological Magazine, 1–30, doi:10.1017/S0016756816000339.

Massironi, M., Bistacchi, A., Menegon, L., 2011. Misoriented faults in exhumed metamorphic complexes: rule or exception? Earth and Planetary Science Letters 307, 233-239, doi:10.1016/j-.epsl.2011.04.041.

McCabe, W.M., Koerner, R. M. 1975. High pressure shear strength investigation of an anisotropic mica schist rock. International Journal of Rock Mechanics and Mining Science & Geomechanics Abstracts 12, 219–228.

Moore, D. E., Lockner, D. A., 2004. Crystallographic controls on the frictional behavior of dry and water-saturated sheet structure minerals. Journal of Geophysical Research 109, B03401.

Mpodozis, C., Ramos, V.A., 1990. The Andes of Chile and Argentina. In: Ericksen, G.E., Canas Pinochet, M.T., Reinemud, J.A. (Ed.), Geology of the Andes and its Relation to Hydrocarbon and Mineral Resources. Earth Science Series 11, 59–90.

Morris, A.P., Ferrill, D.A., Henderson, D.B., 1996. Slip-tendency analysis and fault reactivation. Geology 24, 275, doi.org/10.1130/0091-7613(1996)

Numelin, J., Marone, C., Kirby, E., 2007. Frictional properties of natural fault gouge from a low-angle normal fault, Panamint Valley, California. Tectonics 26, TC2004. doi:10.1029/2005TC001916.

Petruk, W., 1989. Image analysis of minerals. In: Petruck, W. (Ed.), Short course on image analysis applied to mineral and earth sciences. Mineralogical Association of Canada, Ottawa, 6–18.

Ramos, V.A., Kay, S. M., 1991. Triassic rifting and associated basalts in the Cuyo basin, central Argentina. In: Harmon, R.S., Rapela, C.W. (Ed.), Andean Magmatism and its Tectonic Setting Geological Society of America, Special Papers 265, 79–91.

Ramos, V. A., Cristallini, E. O., Perez, D. J., 2002. The Pampean flat- slab of the Central Andes. Journal of South American Earth Sciences 15, 59–78.

Rapela, C.W., Pankhurst, R. J., Casquet, C., Baldo, E. G., Saavedra, J., Galindo, C., Fanning, C. M., 1998. The Pampean orogeny of the southern proto-Andes: Cambrian continental collision in the Sierras de Córdoba. Geological Society of London, Special Publication 142, 181–218.

Rice, J.R., 1992. Fault stress states, pore pressure distributions, and the weakness of the San Andreas Fault. In: Wong, T. (Ed.), Fault Mechanics and Transport Properties of Rocks. Academic Press, San Diego 475–503.

Salfity, J.A., Gorustovich, S.A., 1984. Paleogeografıa del Grupo Paganzo (Paleozoico Superior). Revista de la Asociación Geológica Argentina 38, 437–453.

Schmidt, C.J., Astini, R.A., Costa, C.H., Gardini, C.E., Kraemer, P.E., 1995. Cretaceous rifting, alluvial fan sedimentation, and neogene inversion, Southern Sierras Pampeanas, Argentina. In: Tankard, A.J., Suarez, R., Welsink, H.J. (Ed.). Petroleum Basins of South America. AAPG Memoir 62, 341–358.

Shea, W.T., Kronenberg, A.K., 1993. Strength and anisotropy of foliated rocks with varied mica contents. Journal of Structural Geology 15, 1097-1121. http://dx.doi.org/10.1016/ 0191-8141(93)90158-7.

Sibson, R.H., 1985. A note on fault reactivation. Journal of Structural Geology 7, 751-754. http:// dx.doi.org/10.1016/0191-8141(85)90150-6.

Simpson, C., Whitmeyer, S., De Paor, D.G., Gromet, L. P., Miro, R., Krol, M. A., Short, H., 2001. Sequential ductile through brittle reactivation of major fault zones along the accretionary margin of Gondwana in Central Argentina. Geological Society of London, Special Publication 186.

Simpson, C., Law, R. D., Gromet, L. P., Miro, R., Northrup, C. J., 2003. Paleozoic deformation in the Sierras de Córdoba and Sierra de Las Minas, eastern Sierras Pampeanas, Argentina. Journal of South American Earth Sciences 15, 749–764.

Sims, J., Ireland, T.R., Camacho, A., Lyons, P., Pieters, P.E., Skirrow, R., Stuart-Smith, P., Miro, R., 1998. U–Pb, Th–Pb and Ar–Ar geochronology from the southern Sierras Pampeanas, Argentina: implications for the Paleozoic tectonic evolution of the western Gondwana margin. Geological Society of London, Special Publication 142, 259–281.

Steenken, A., Wemmer, K., Martino, R.D., López de Luchi, M.G., Guereschi, A., Siegesmund, S., 2010. Post-Pampean cooling and the uplift of the Sierras Pampeanas in the west of Córdoba (Central Argentina). Neues Jahrbuch Fur Geologie Und Palaontologie-Abhandlungen 256(2), 235–255, doi:10.1127/0077-7749/2010/0094.

Traforti, A., Zampieri, D., Massironi, M., Bistacchi, A., Viola, G., (Chapter 2). Unravelling polyphase brittle deformation histories - Part I: A critical approach to paleostress inversion within lithologically heterogeneous terranes: The example of the Sierras de Córdoba (Argentina). Journal of Structural Geology.

Uliana, M.A., Biddle, K.T., Cerdan, J., 1989. Mesozoic extension and the formation of Argentine sedimentary basins. In: Tankard, A.J., Balkwill, H.R. (Ed.), Extensional Tectonics and the Stratigraphy of the North Atlantic Margins. AAPG Memoir 46, 599–614.

Van Diggelen, E.W.E., De Bresser, J.H.P., Peach, C.J., Spiers, C.J., 2010. High shear strain behaviour of synthetic muscovite fault gouges under hydrothermal conditions. Journal of Structural Geology 32, 1685-1700. http://dx.doi.org/10.1016/ j.jsg.2009.08.020.

Vigny, C., Rudloff, A., Ruegg, J., Madariaga, R., Campos, J., Alvarez, M., 2009. Upper plate deformation measured by GPS in the Coquimbo Gap, Chile. Physics of the Earth and Planetary Interiors 175, 86–95.

Walsh, J.B., Brace, W. F., 1964. A fracture criterion for brittle anisotropic rock. Journal of Geophysical Research 69, 3449–3456.

Whitmeyer, S.J., Simpson, C., 2003. High strain-rate deformation fabrics characterize a kilometers-thick Paleozoic fault zone in the eastern Sierras Pampeanas, central Argentina. Journal of Structural Geology 25, 909–922.

Whitmeyer, S.J., 2008. Dating fault fabrics using modern techniques of $^{40}Ar/^{39}Ar$ thermochronology: evidence for Paleozoic deformation in the Eastern Sierras Pampeanas, Argentina. In: De Paor, D. (Ed.), Making Sense of Shear. Journal of the Virtual Explorer 30, paper 3, doi:10.3809/jvirtex.2008.00207.

Yáñez, G. A., Ranero, C. R., Von Huene, R., Díaz, J., 2001. Magnetic anomaly interpretation across the southern central Andes (32°–34° S): The role of the Juan Fernández Ridge in the late Tertiary evolution of the margin. Journal of Geophysical Research 106(B4), 6325–45.

4. VNIR-SWIR spectral characterization of comminuted carbonate fault rocks

A. Traforti[a], C. Carli[b], M. Demurtas[a], G. Mari[a], M. Massironi[a], Di Toro Giulio[a]

[a]Dipartimento di Geoscienze, Università degli Studi di Padova, via Gradenigo, 6, 35131 Padova, Italy.

[b]Inaf-IAPS, Viale Fosso del Cavaliere Tor Vergata, 00133 Roma, Italy.

Abstract

The reflectance spectrum in the VNIR and SWIR spectral ranges have been extensively used to obtain several information about a surface from remote sensed data. Electronic and molecular absorption can be correlate with mineral chemistry and mineral associations on a specific surface. Moreover, variation in grain size (i.e., both the size of rock components and the size of particulates) affect the spectrum information in terms of spectral shape (e.g., slope), band strength and reflectance values. Investigating the effects of grains size on spectral signature can give information about the different geological processes modifying the Earth and other planetary surfaces. In this study we analyze the variations in fault rock spectral signatures highlighting a correlation with the grain size reduction associated to fault zone development. For this purpose we consider the Vado di Corno Fault Zone (VCFZ), an extensional fault cutting through a dolomitized carbonate sequence in the Italian Central Apennines. This represents a mature fault zone affecting host rock bearing a homogeneous composition and thus provides a suitable condition to evaluate the spectral signatures variation solely due to fault-related comminution processes.

We performed VNIR and SWIR reflectance analysis of fifteen rock samples collected at increasing distances from the VCFZ core, showing similar content of calcite and dolomite but different grain size. Bidirectional reflectance spectra were acquired on both crushed rock powders (reduced at 11 particle fractions between < 50 μm and < 800 μm) and on intact fault zone rock slabs. The spectral analysis of the crushed and intact rock slabs revealed that with increasing grain size: (i) reflectance decreases; (ii) main absorption band depths increase (i.e., absorption bands at ca. 1400, 1900 and 2300 nm) and (iii) VNIR and SWIR spectrum slopes increase. Therefore, the grain size variations resulting from fault zone evolution influences systematically the absorption feature characteristics of fault rock spectral signatures. Hence the remote sensing analysis at high spatial resolution can be

potentially applied in the VNIR-SWIR spectral range to identify the distribution and extent of fault core and damage zone domains.

1 Introduction

Reflectance spectroscopy in the visible-near infrared (VNIR, 0.4-1.0 μm) and shortwave infrared (SWIR, 1.0-2.5 μm) is a common technique used for remote sensing investigation of Earth and other planetary surfaces. The VNIR and SWIR spectral ranges present prominent absorption features related to both electronic and molecular (i.e., vibrational) absorption processes (e.g., Clark, 1990; 1999; Gaffey et al., 1993; Hapke, 1993). The spectral characteristics of these features vary depending on composition and physical properties (e.g., grain size, roughness) of the sensed materials. The characterization of the spectral variability related to rock texture, especially in terms of grain size (i.e., both the size of rock components and the size of particulates), commonly allows to obtain a wide range of information about the different geological processes modifying the Earth and other planetary surfaces (e.g., Crown and Pieters 1987; Cooper and Mustard 1999; Milana, 2000; Nolin and Dozier, 2000; Okin and Painter, 2004; Ghrefat et al., 2007; Carli et al., 2015). A wealth of experimental studies established that grain size affects the spectral characteristics of particulate materials (e.g., Hunt and Vincent 1968; Crown and Pieters 1987; Gaffey et al., 1993; Harloff and Arnold 2001; Craig et al., 2007, 2008; Zaini et al, 2012). The more evident effect is the decrease in the spectral reflectance with increasing grain size of particles (e.g., Adams and Filice, 1967; Ross et al., 1969; Gaffey et al., 1993; Hapke, 1993; Craig et al., 2007) that is due to the increasing contribution of first surface scattering relative to volume scattering. Particle size is also important in defining the strength of absorption features, in fact each absorption band shows an optimal particle size that maximizes its band depth (e.g., Gaffey et al., 1993; Hapke, 1993; Harloff and Arnold 2001). The effects of grain size on the reflectance spectrum in the VNIR and SWIR spectral ranges have been extensively used in modelling grain size variations, for example to recognize snow/ice deposits on the Earth (Painter et al., 1998, 2009; Nolin and Dozier, 2000), to identify different surface deposits on different planetary environments (e.g., Crown and Pieters 1987; Cooper and Mustard 1999) and to investigate grain size variations related to diverse transport processes on Earth (Shipman and Adams, 1987; Blount et al., 1990; Paisley et al., 1991; Milana, 2000; Okin and

Painter, 2004; Ghrefat et al., 2007). Despite these extensive remote sensing applications, the variation of the VNIR-SWIR spectral characteristics with the grain size has never been exploited to investigate the grain size reduction associated to fault zones and comminution processes.

Fault zones develop through increasing levels of strain localization leading to the development of characteristic fault zone architecture, which consists of a fault core, where most of the displacement is accumulated, surrounded by a pervasively deformed damage zone (e.g., Caine et al., 1996; Childs et al., 2009; Faulkner et al., 2010). The fault core is characterized by intense comminution and includes fault products reduced at variable clast size: gouges, ultracataclasites, cataclasites and breccias (Sibson, 1977). The damage zone includes rocks at the fault zone margins where fracturing, veining and faulting is relatively intense with respect to the regional background (Chester et al., 1993; Caine et al., 1996; Wibberley et al., 2008; Bistacchi et al. 2010). The common approach used for the characterization of crustal-scale fault zone architecture is based on the meso- to micro-scale detailed field analysis of exhumed fault zones (Billi et al., 2003; Faulkner et al., 2003; Tesei et al., 2013; Fondriest et al. 2012; Demurtas et al., 2016). Remote sensing studies aimed at identifying fault zones are mainly based on the detection lineament features (Bistacchi et al., 2000; Kavak and Inan, 2002; Masoud et al., 2011) or fault-related mineralisation (i.e., Massironi et al., 2008), but remote sensing analysis aimed at characterizing the distribution of variably comminuted fault zone rocks has never been given.

The objective of the present study is to investigate how the grain size reduction associated to fault zone development produces reflectance variations in rock and mineral spectral signatures. The more suitable condition to achieve this goal is given by considering mature fault zone (i.e., presenting a significant structural thickness, Chambon et al., 2006) affecting host rock bearing a simple and homogeneous composition. This allows to evaluate the spectral signatures variation solely due to fault-related comminution processes. In this view, we performed VNIR and SWIR reflectance analysis of a set of fifteen rock samples

collected at increasing distances from the fault core of the Vado di Corno Fault Zone (VCFZ, Campo Imperatore Fault System), an extensional fault cutting through a dolomitized carbonate sequence in the Italian Central Apennines (*Figure 4.1*). The selected samples show similar content of calcite and dolomite but different grain size. Consequently, differences in the spectral signature of the fault rocks should not be ascribed to mineralogical composition, but only to the variations in grain size related to fault comminution processes.

2 Vado di Corno fault zone

The Vado di Corno Fault Zone (VCFZ) is an active extensional fault in the Italian Central Apennines that belongs to the larger Campo Imperatore Fault System (CIFS; *Figure 4.1*). The VCFZ was exhumed from ~2 km depth and accommodated a normal throw of ~2 km since the Early-Pleistocene (Agosta and Kirschner, 2003). In the study area, the VCFZ is developed principally within the Lower Jurassic Calcare Massiccio Fm. (e.g., Adamoli et al., 2003, 2012), which consists of an up to 600 m thick limestone sequence. The occurrence of dolostones in the Calcare Massiccio Fm. is frequent and it is largely ubiquitous in the studied outcrops, where two dolostone facies were recognized (Demurtas et al., 2016): (i) dolomicrite to dolomitic packstone-wackestones with preserved original microfabric and (ii) crystalline dolostones with coarse crystal/grain size. The two facies are interpreted as the product of distinct events of dolomitization (different both for timing and intensity). A major dolomitization pulse was triggered by contractional tectonism occurred in the area in the Middle to Late Pliocene (Demurtas et al., 2016). In fact, the footwall of the VCFZ is affected by a pre-existing shallow-dipping thrust that juxtaposes the Lower Jurassic Calcare Massiccio Fm. onto the Middle Jurassic Verde Ammonitico Fm. (e.g., Adamoli et al., 2012). Secondary dolostones pervasively exploited the thrust damage zones, being synchronous to or postdating the contractional event (Demurtas et al., 2016), and are systematically crushed within fault rocks associated with the Quaternary Vado di Corno master fault, indicating that dolomitization preceded the extensional faulting. This is an important factor

to be accounted as the dolomitization related to the presence of the Pliocene thrust have influenced both the intensity of deformation and the width of the footwall damage zone (Demurtas et al., 2016).

We analysed the VCFZ at northern margin of the Campo Imperatore intramontane basin (*Figure 4.1*), where the fault zone outcrops almost continuously for ca. 5 km, with an extremely good exposure ensured by several creeks affected by fast erosion and badland topography. At the base of the badlands, the master fault juxtaposes cataclastic dolostones in the footwall with Quaternary deposits in the hanging wall, through a polished fault slip surface that shows an average attitude of N209/54° (dip azimuth/dip angle) and average pitch of 80° to the E (Demurtas et al., 2016). The master fault is associated with a ca. 40 m thick cataclastic fault core affecting the footwall block, in which the principal slip zone consists of a ca. 20 cm thick cataclastic layer characterized by cohesive injections of ultracataclasites (up to two-centimeter-thick) (*Figure 4.2*A). A detailed characterization of the internal structure of the VCFZ is provided by Demurtas et al. 2016, which evidenced the presence of five main structural units: (*i*) Low Strain Damage Zone (LSDZ) including relatively poorly deformed rock volumes, where sedimentary features of the host rocks are well recognizable and joints are the most abundant deformation features; (*ii*) High Strain Damage Zone (HSDZ), which consists of fractured rock volumes with significantly higher fracture density/intensity with respect to the LSDZ; (*iii*) Breccia Unit (BU) consisting of cohesive crush breccias (Sibson, 1977) with evidence of pervasive secondary dolomitization and dolomite veining strictly related to presence of the pre-existing Pliocene thrust; (*iv*) Cataclastic Unit 1 (CU1) including protocataclasites and cataclasites, where the original fabric of the protolith is still recognizable and (*v*) Cataclastic Unit 2 (CU2) that consists of white fine-grained (average grain size <1-2 mm) calcite cemented ultracataclasite. The structural unit classification proposed for the VCFZ by Demurtas et al., 2016 drove the choice of the sampling sites of this study.

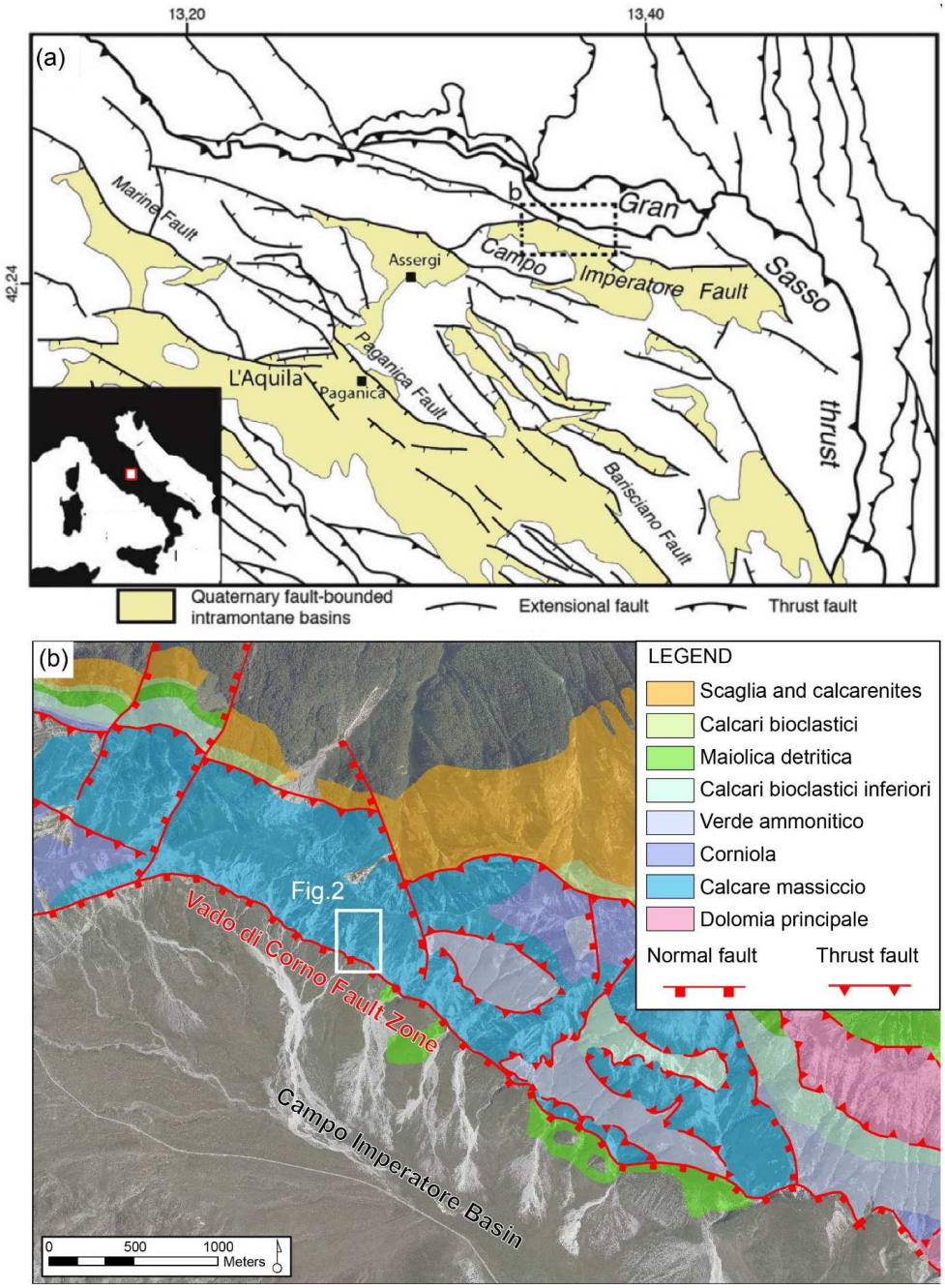

***Figure 4.1**: Geological setting of the Campo Imperatore area. (a) Structural map of the Gran Sasso area (modified after Storti et al., 2013). (b) Geological map of the study area modified after Demurtas et al., 2016. The map represents a simplified scheme of the published Foglio 349 "Gran Sasso d'Italia" (Ispra, 2012). Quaternary colluvial deposits of the Campo Imperatore intramontane basin correspond to the non-colored areas.*

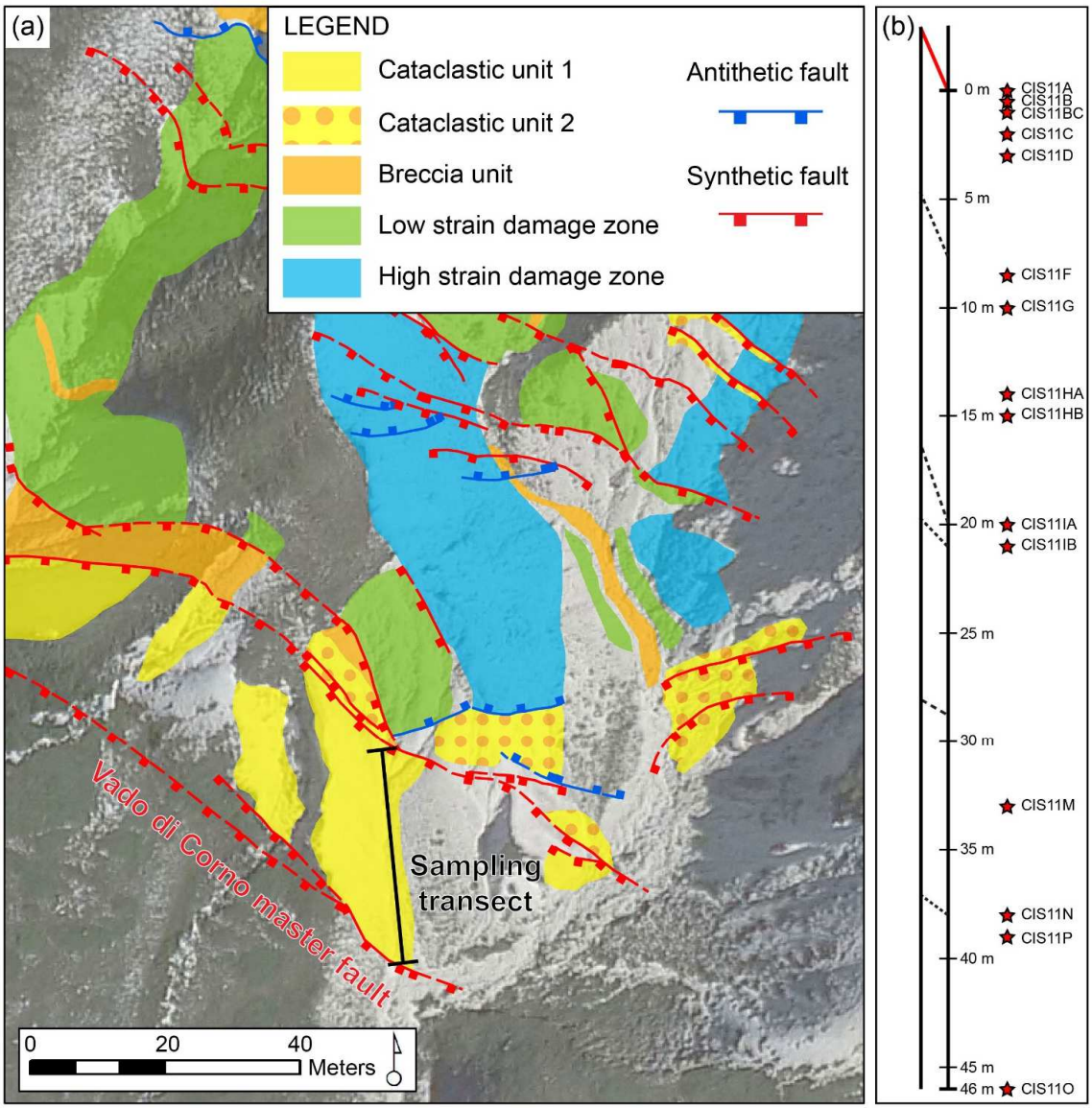

***Figure 4.2**: (a) Structural map of the study area (modified from Demurtas et al., 2016) and location of the sampling transect. The structural map shows the principal fault strands and the distribution of the five structural units defined by Demurtas et al., 2016. The selected sampling transect is located in the footwall of VCFZ and belongs to the fault core. (b) Distribution of the collected samples along the considered sampling transect. Location and direction of master fault (red line) and minor faults (black dashed line) are indicated on the side. The sampling transect strikes N 174°.*

2.1 Sample collection and characterization

We collected fifteen samples along a selected transect, which strikes N 174° and starts from the master fault of the VCFZ (*Figure 4.2*). The sampling sites were chosen at increasing distance from the master fault in the exposed footwall (*Figure 4.2*) based on texitural characteristics distinguishable in the field (i.e., clast/matrix proportion, color of non-weathered rocks and relative abundance of veins). All the selected samples belong to the core of VCFZ (i.e., corresponding to CU1 and CU2 structural units defined in Demurtas et al., 2016) and can be placed in the "cataclasite series" defined by Sibson (1977) on the basis of volumetric matrix content (10-50% for a protocataclasite, 50-90% for a cataclasite and 90-100% for an ultracataclasite).

Microstructural observations and mineral phase identification were conducted on polished thin sections using transmitted-light optical microscopy (OM), scanning electron microscopy (SEM) and energy dispersive spectroscopy (EDS) at the SEM, while mineral composition was determined by semi-quantitative X-ray powder diffraction analysis (XRPD). On the basis of Sibson (1977) the sampled fault rocks have been divided into four classes: (*i*) ultracataclasite; (*ii*) cataclasite; (*iii*) protoclataclasite and (*iv*) protoclataclasite with pervasive veins. Ultracataclasites are characterized by few fine-grained dolostone clasts (size < 10-20 µm) with angular to sub-rounded shape immersed in abundant matrix (*Figure 4.3*A and *Figure 4.3B*), which consists of angular dolostone grains (size < 5-10 µm) frequently cemented by calcite (*Figure 4.3B*). Ultracataclasite hand samples are white in color and associated with the slip zone of the VCFZ master fault (consisting of centimeter-thick, cohesive injections) or localized along the high slip zone of minor faults within the VCFZ core and damage zone. Cataclasites consist of angular to sub-rounded dolostone clasts (size < 1 cm) immersed in a matrix of angular dolostone grains with size below 10 µm down to 1 µm (*Figure 4.3C*). Extended areas of calcite cement with polygonal crystals of 10-20 µm in size occur locally filling pores in the dolomite matrix (*Figure 4.3D*).

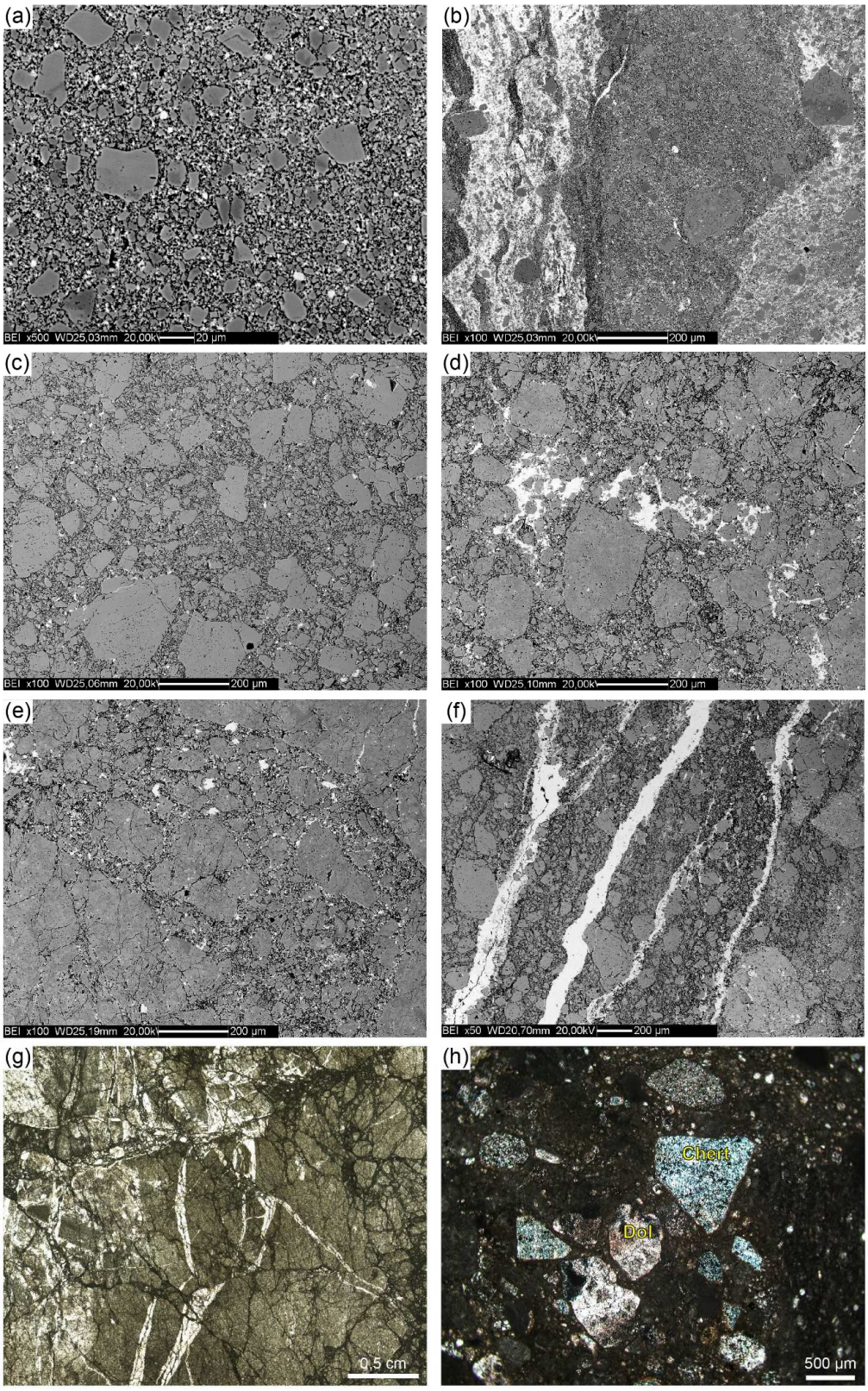
(a)
BEI x500 WD25,03mm 20,00kV 20 µm
(b)
BEI x100 WD25,03mm 20,00kV 200 µm
(c)
BEI x100 WD25,06mm 20,00kV 200 µm
(d)
BEI x100 WD25,10mm 20,00kV 200 µm
(e)
BEI x100 WD25,19mm 20,00kV 200 µm
(f)
BEI x50 WD20,70mm 20,00kV 200 µm
(g)
0,5 cm
(h)
Chert
Dol
500 µm

Figure 4.3*: Microstructural observations of the VCFZ samples. (a) Fine-grained dolostone clasts with angular to sub-rounded shape immersed in a fine and abundant matrix of ultracataclasite sample (BSE-SEM image). (b) Ultracataclasite sample displays a foliated fabric consisting of alternating bands of fragmented dolomite clasts and sheared calcite matrix (BSE-SEM image). (c) Cataclasite sample showing angular to sub-rounded dolostone clasts immersed in a matrix of angular dolostone grains (BSE-SEM image). (d) Calcite cement locally filling pores in the dolomite matrix of a catalcasite sample (BSE-SEM image). (e) Fractured protocataclasite clasts with narrow cataclastic bands (BSE-SEM image). (f) Cataclasite cut by a pervasive network of calcite-bearing veins. (g) Protoclataclasite with pervasive veins (OM image). (h) Micro-crystalline chert in CIS11A sample collected within the core of the VCFZ master fault (OM image).*

Additionally, some cataclasites and ultracataclasites display a foliated fabric that consists of alternating bands of fragmented dolomite clasts and sheared calcite matrix (*Figure 4.3B*). Protocataclasites consist of clasts of cm-to tens of cm in size, which are pervasively fractured in-situ down to the millimeter scale (in-situ shattering sensu Brune, 2001). The presence of matrix is scarce and limited to narrow cataclastic bands (*Figure 4.3E*). Ultracataclasites, cataclasites and protocataclasites are characterized by veins filled by calcite with variable average crystals size (e.g., up to 10-50 μm for ultracataclasites) (*Figure 4.3F*). In particular, protocataclasites appear to be cut by a pervasive network of dolomite- and calcite-bearing veins (maximum aperture 1 cm) sealing the entire fragmented rock volume (*Figure 4.3G*). Most of the veins show a lateral continuity up to few tens of centimetres, irregular shape and complex cross-cutting relationships among different vein sets.

Table 4.1 reports for each sample: the sampling distance (i.e., meters from the master fault measured along the sampling transect), the fault rock classification and the bulk mineralogical composition determined by means of semi-quantitative XRPD analysis. The analyzed samples show a constant proportion of calcite and dolomite (i.e., about 1-10 wt% of calcite and 99-90 wt% of dolomite) yielding an overall homogeneous composition. Sample CIS11A represents an exception to this homogeneity as it contains quartz (5 wt %) and shows a higher content of calcite (34 wt %). In fact, CIS11A was collected within the

core of the VCFZ master fault and show in OM micro-crystalline chert (*Figure 4.3H*) and fine-grained iron oxides, which have been interpreted as the result of a mixing within the slipping zone of quaternary materials derived from the hanging wall (Demurtas et al., 2016). For this reason, in the following the results deriving from CIS11A sample will not be considered. Additionally, CIS11D contains Fe-rich dolomite coherently to what has been observed in BSE-SEM images for the same sample. In fact, CIS11D shows zonation of dolomite crystals (*Figure 4.3E*), which yield Fe-rich composition in their inner portions (EDS-SEM analysis).

Sample	Distance from master fault (m)	Fault zone rock classification	Dolomite (wt%)	Ca-Dolomite (wt%)	Fe-Dolomite (wt%)	Calcite (wt%)	Quartz (wt%)
CIS11A	0	Cataclasite-Ultracataclasite	61	-	-	34	5
CIS11B	0,5	Cataclasite	67	29	-	4	-
CIS11BC	1	Cataclasite	62	33	-	5	-
CIS11C	2	Cataclasite	98	-	-	2	-
CIS11D	3	Protocataclasite	31	30	36	3	-
CIS11F	8,5	Protocataclasite	43	51	-	6	-
CIS11G	10	Protocataclasite with pervasive veins	63	35	-	2	-
CIS11HA	14	Protocataclasite with pervasive veins	48	51	-	1	-
CIS11HB	15	Protocataclasite with pervasive veins	35	62	-	3	-
CIS11IA	20	Protocataclasite	97	-	-	3	-
CIS11IB	21	Protocataclasite	65	33	-	2	-
CIS11M	33	Cataclasite	99	-	-	1	-
CIS11N	38	Ultracataclasite	49	37	-	14	-
CIS11P	39	Protocataclasite		96	-	4	-
CIS11O	46	Protocataclasite with pervasive veins	30	67	-	3	-

***Table 4.1**: Characterization of the samples collected in the VCFZ footwall. The table reports for each sample: the sampling distance (i.e., meters from the master fault measured along the transect), the fault rock classification and the bulk mineralogical composition determined by means of semi-quantitative XRPD analysis.*

2.1.1 Clast size distribution analysis (CSD)

In order to give an estimate of the clast size variation characterizing the collected fault rock samples, a two-dimensional clast size distribution (CSD) analysis was performed on high-resolution back scattered electron (BSE) SEM images acquired at different magnification (i.e., 100X, 500X, 1000X). The BSE-SEM images were converted into binary images (*Figure 4.4*) and the clast dimensions were determined using Image SXM 199 software. The studied fault zone rocks consist of dolostone clasts within a dolomitic matrix and secondary calcite cement and veins, resulting in a high clast interconnectivity in the binary images (i.e., clast-bridging) that makes difficult the automatic recognition of clasts by Image SXM 199 software. To avoid this problem, clasts were visually separated before clast dimension determination. Clast size was expressed as equivalent diameter (d_{eq}), which represents the diameter of a circle with the same area of the clast (Marone and Scholz, 1989). The obtained CSDs were assumed to be homogeneous for all the acquired magnifications. Therefore, in order to make the results obtained at different magnifications comparable, the number of clasts retrieved at the high magnifications (i.e., 500X and 1000X) was multiplied for a scale factor equal to the number of 500X frames (or 1000X frames) contained in a 100X images. The obtained results can thus be plotted in a unique diagram and were reported both as log(N) – log(d_{eq}) plots and clast-size distribution curves (*Figure 4.4A and Figure 4.4B*). The former were obtained by combining size-frequency data over the whole particle dimension range and plotting the cumulative number of clasts larger than a given diameter d_{eq} (N) in a log(N) – log(d_{eq}) diagram (e.g., Monzawa and Otsuki, 2003; Fondriest et al., 2012). The clast-size distribution curves were obtained plotting in a semi-logarithmic diagram the d_{eq} (x axis) against the cumulative area of clast larger than a given d_{eq} expressed in percentage (y axis).

We report the CSD analysis performed on samples CIS11N (ultracataclasite), CIS11C (cataclasite), CIS11D (protocataclasite).

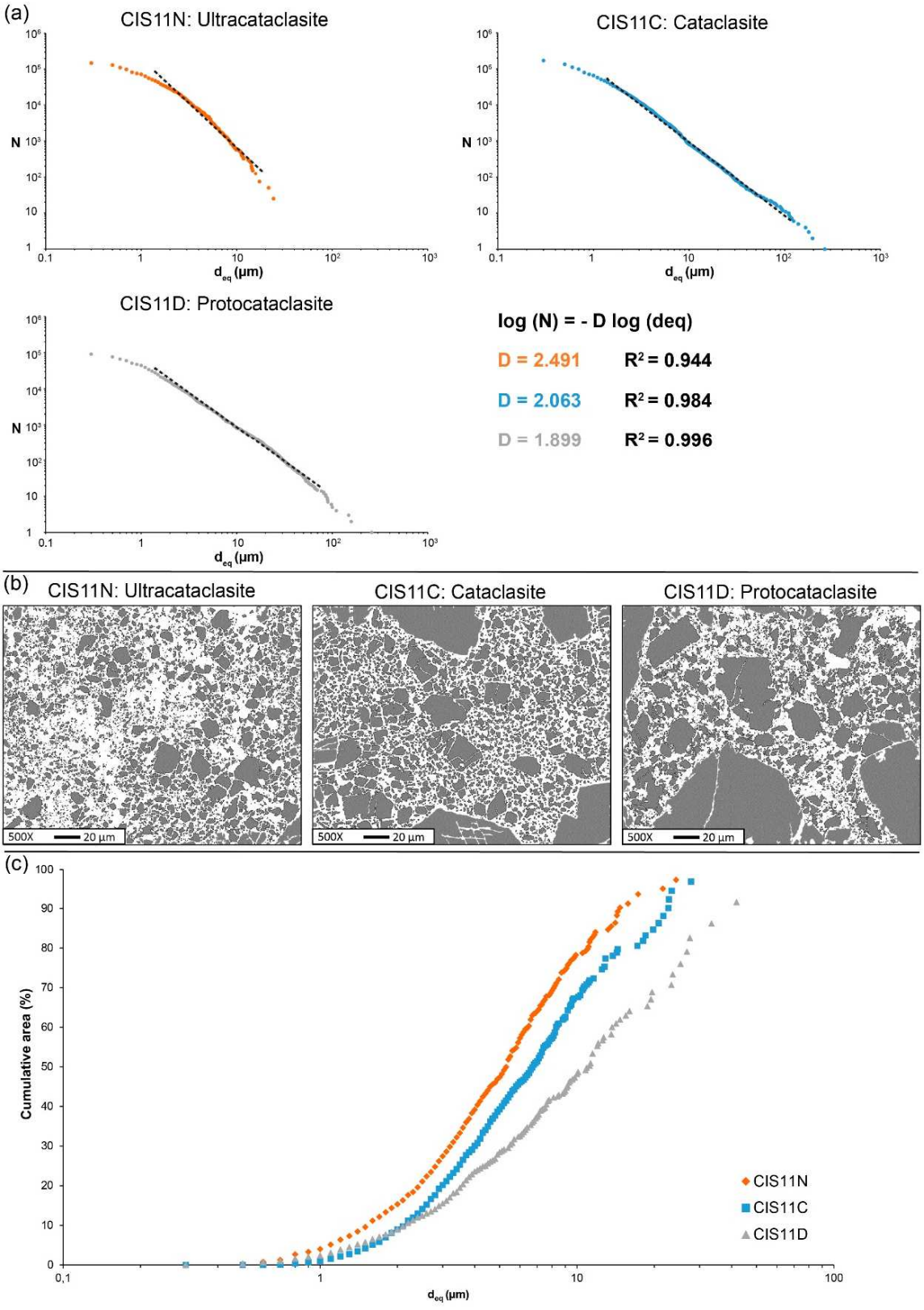
(a)
CIS11N: Ultracataclasite
CIS11C: Cataclasite
CIS11D: Protocataclasite
N
d_{eq} (µm)
log (N) = - D log (deq)
D = 2.491 R^2 = 0.944
D = 2.063 R^2 = 0.984
D = 1.899 R^2 = 0.996
(b)
CIS11N: Ultracataclasite
CIS11C: Cataclasite
CIS11D: Protocataclasite
500X
20 µm
(c)
Cumulative area (%)
d_{eq} (µm)
CIS11N
CIS11C
CIS11D

Figure 4.4*: Clasts size distributions (CSDs) of samples CIS11N (ultracataclasite), CIS11C (cataclasite) and CIS11D (protocataclasite). (a) log(N) – log(deq) diagram obtained for each sample. All the curves are well described by a power-law distribution with fractal dimensions D that increase with increasing grain size. See Section 2 for discussion. R represents the correlation coefficient expressing the strength of the power-law relationship in the selected fractal range. (b) BSE-SEM images acquired at 500X magnification for samples CIS11N (ultracataclasite), CIS11C (cataclasite) and CIS11D (protocataclasite) and converted into binary images for the automatic recognition of clasts. (c) Clast-size distribution curves obtained from the images reported in (b). See Section 2 for discussion.*

Protocataclasites with pervasive veins were not considered during CSD analysis because the vein network prevents the automatic recognition of clasts by Image SXM 199 software, whereas protocataclasite sample was analysed only on the cataclastic bands due to the sampling limits determined by the size of the analysed images.

Figure 4.4A reports the log(N) – log(d_{eq}) diagram obtained for each sample. The lower limits of the obtained CSDs correspond to the lower cut off diameter defined for the analysis, whereas the upper limits of the CSDs are determined by the size of the analysed images ("censoring effect"). Going beyond these effects at the data tails, all the CSD curves follow a linear trend that can be described by a power-law relationship: $N \approx d^{-D}$ (i.e., $\log(N) \approx -D\log(d)$), where D is the fractal dimension (Turcotte, 1986). For sample CIS11N (ultracataclasite) the segment fitting the CSD linear trend shows a higher slope with respect to CIS11C sample (cataclasite), where the cataclasis is less pronounced implying a greater number of larger clasts. The same relationship is confirmed considering CIS11C and CIS11D (protocataclasite) samples. As the analyzed CSDs cover a small dimensional range (three orders of magnitude), we can use the D values only to quantify the relative differences between the studied fault rock samples. The fractal dimensions D are: 2.491 for ultracataclasite (CIS11N), 2.063 for cataclasite (CIS11C) and 1.899 for protocataclasite (CIS11D). The D value decreases going from the ultracataclasite to the protocataclasite samples and thus with increasing distance from the fault core, as revealed by previous studies (i.e., fractal dimension of natural fault rocks increases as comminution proceeds: e.g., Monzawa and Otsuki, 2003; Muto et al., 2015). The CSD results are consistent with

previous literature and account for an increasing grain size going from fault rock samples belonging to ultracataclasite class toward samples classified as protocataclasite.

Figure 4.4B displays the clast-size distribution curves obtained for CIS11N (ultracataclasite), CIS11C (cataclasite), CIS11D (protocataclasite) on BSE-SEM images acquired at the same magnification (i.e., 500X). The clast-size distribution curves are shifted towards larger clast diameters going from ultacataclasite to protocataclasite samples, confirming what has been stated for log(N) – log(d_{eq}) diagrams.

3 Spectroscopic analysis

3.1 Sample preparation

Fault rock samples for bidirectional reflectance spectrum acquisition were crushed using a steel jaws-crusher and then pulverize in a mortar grinder. The powders were dry-sieved at 11 particle sizes between 0 and 800 μm (i.e., < 50, 75-50, 75-100, 100-125, 125-150, 150-180, 180-200, 200-224, 224-250, 250-500, 500-800 μm). Furthermore, intact fault zone rock slabs were prepared from the same samples by cutting slabs with a thickness of about 1.4 cm using a diamond saw. For each specimen, the two basal surfaces were horizontally evened out with a grinding wheel in order to remove the roughness connected to the saw cut and to ensure that the slab surfaces would not be tilted relative to the focal plane of the spectrometer during the spectroscopic measurements. We also took careful that slabs do not show a mirror-like surface.

3.2 Spectroscopic measurement and spectral absorption features analysis

Bidirectional reflectance spectra were acquired on dry samples, at room temperature and normal atmospheric pressure with a Field-Pro Spectrometer mounted on a goniometer (Istituto di Astrofisica e Planetologie Spaziali, Inaf-IAPS, Roma). The source used was a Quartz Tungsten Halogen lamp with an illuminated spot area of ca. 0.5 cm^2 and incidence and emission angles of 30˚ and 0˚ respectively. The calibration of the spectrometer was

performed with Spectralon® optical standard (registered trademark of Labsphere, Inc.). The spectra were measured in the 350 – 2500 nm range with 1 nm spectral sampling and a spectral resolution of 3 nm in the VIS and up to 10–12 nm in the NIR. An identical viewing geometry and probe to sample distance were maintained for the spectral acquisition on both powdered and rock slab samples. The measurements on powdered samples were repeated three times for each particle size, in order to account for reflectance variations due to experimental errors and to have a more detailed statistics.

The influence of grain size reduction on acquired VNIR SWIR spectra is described in terms of reflectance, absorption band position, band depth and spectral slope. The spectral parameter variations were determined using the software Origin ®. Continuum removed spectra are, in general, determined considering the continuum line as the straight-line segments that join the reflectance maxima in the spectrum (Clark and Roush, 1984). Here we observed how, by considering a spline joining the reflectance maxima, the continuum optimally described the envelope of the spectrum, thus we preferred to apply a spline for all the cases using the function present in the Origin ® software. Moreover, to avoid noise influence on band absorption parameters, we applied a smoothing function base on a Fast Fourier Transform (FFT) algorithm using ten data points. This smoothing function has been applied to each average spectrum without significant effects on the diagnostic band minimum positions. The band depth was calculated as the ratio between the reflectance at the band center and the reflectance of the continuum at the band center (Clark and Roush, 1984), whereas the spectral slope was qualitatively evaluated in the VIS (i.e., wavelengths < 750 nm) and NIR-SWIR (i.e., wavelengths >750 nm) spectral ranges by normalizing the reflectance spectrum at 750 nm. In addition, the spectral slope in the VIS was calculated as the ratio between the spectral reflectance at 650 nm and spectral reflectance at 450 nm.

The considered absorption bands characterizing the analyzed spectra are showed in *Figure 4.5*. These are overtone absorptions that can be attributable to OH^-, H_2O and CO_3^{2-} vibrations (e.g., Clark et al., 1990; Clark, 1999), in particular: (*i*) "*Band a*" indicates the

asymmetric absorption band at ca. 1400 nm due to vibrational absorption of OH^-, (*ii*) "*Band b*" represents the asymmetric narrow absorption band at ca. 1900 nm due to vibrational absorption of H_2O, (*iii*) "*Band c*" indicates the asymmetric narrow absorption band at ca. 2300 nm due to overtones of internal vibrational processes of CO_3^{2-} carbonate ion and (*iv*) "*Band d*" the absorption band at ca. 2500 nm due to overtones and combination tones of internal vibrational processes of carbonate ion. *Band d* displays only its left side band shoulder due to the acquired spectral range (i.e., 350 – 2500 nm) and it is affected by higher noise due to both lamp characteristics and detector sensitivity.

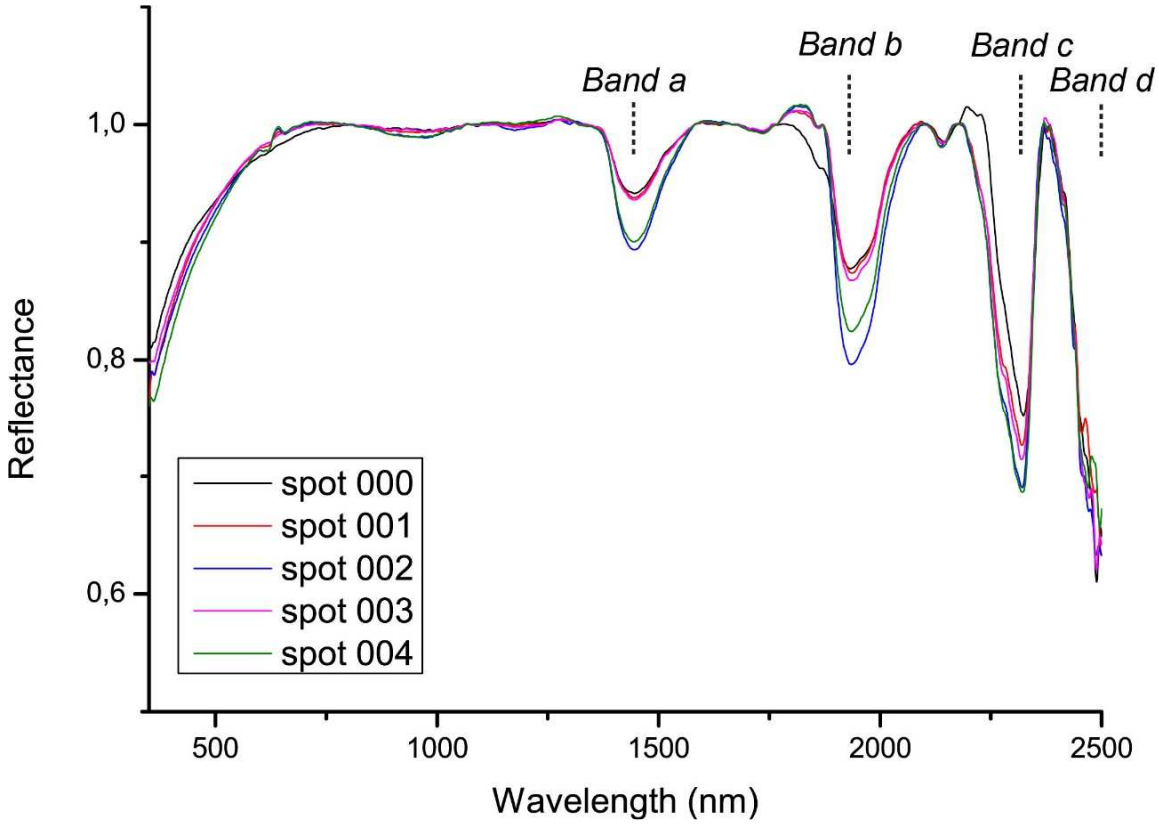

***Figure 4.5**: Main absorption bands characterizing the continuum removed spectra acquired on CIS11B sample. The reflectance spectra were acquired on the intact slab surface and the associated measurment spots are reported in Figure 9B. Band a (1400 nm) is due to the typical vibrational absorption of OH^-. Band b (1900 nm) is related to the diagnostic vibrational absorption of H_2O. Band c (2300 nm) is due to overtones of internal vibrational processes of carbonate ion. Band d (2500 nm) is associated with overtones and combination tones of internal vibrational processes of carbonate ion.*

For each absorption band we evaluated the position of the band center as the wavelength corresponding to the reflectance minimum of the continuum-removed spectrum and the absorption band depth as the distance between the minimum and the continuum line. The spectral slope in the VIS (i.e., wavelengths < 750 nm) and NIR-SWIR (i.e., wavelengths >750 nm) ranges has been qualitatively evaluated by normalizing the analyzed spectra at 750 nm.

4 Results

4.1 Spectral characteristic of powders

Figure 4.6 (A-D) reports the reflectance spectra for the 11 particle sizes obtained by crushing samples CIS11N (ultracataclasite), CIS11C (cataclasite), CIS11D (protocataclasite) and CIS11O (protocataclasite with pervasive veins), each of which is representative of the related fault rock class defined in this study. All the measured spectra show the sample diagnostic absorption features reported in *Figure 4.5* (i.e., *band a*, *b*, *c*, *d*). As expected from the optical theory, the spectral reflectance decreases with increasing particle size for each sample.

Figure 4.6(E-F) reports the reflectance spectra for the 11 particle sizes obtained for samples CIS11N, CIS11C, CIS11D and CIS11O normalized at 750 nm showing how the spectral slope in the VIS (i.e., wavelengths < 750 nm) and NIR-SWIR (i.e., wavelengths >750 nm) spectral ranges increase with increasing particle size. This aspect was further analyzed in the VIS, where no diagnostic absorption bands are present. *Figure 4.7* reports the VIS spectral slopes calculated as the ratio between the spectral reflectance at 650 nm and spectral reflectance at 450 nm. For each fault rock sample, *Figure 4.7* shows how the spectral slope in the VIS range increases with increasing particle size. This trend is particularly evident for the protocataclasite (CIS11D and CIS11O) and cataclasite (CIS11C) samples, but it is not systematically observable for the ultracataclasite (CIS11N) sample.

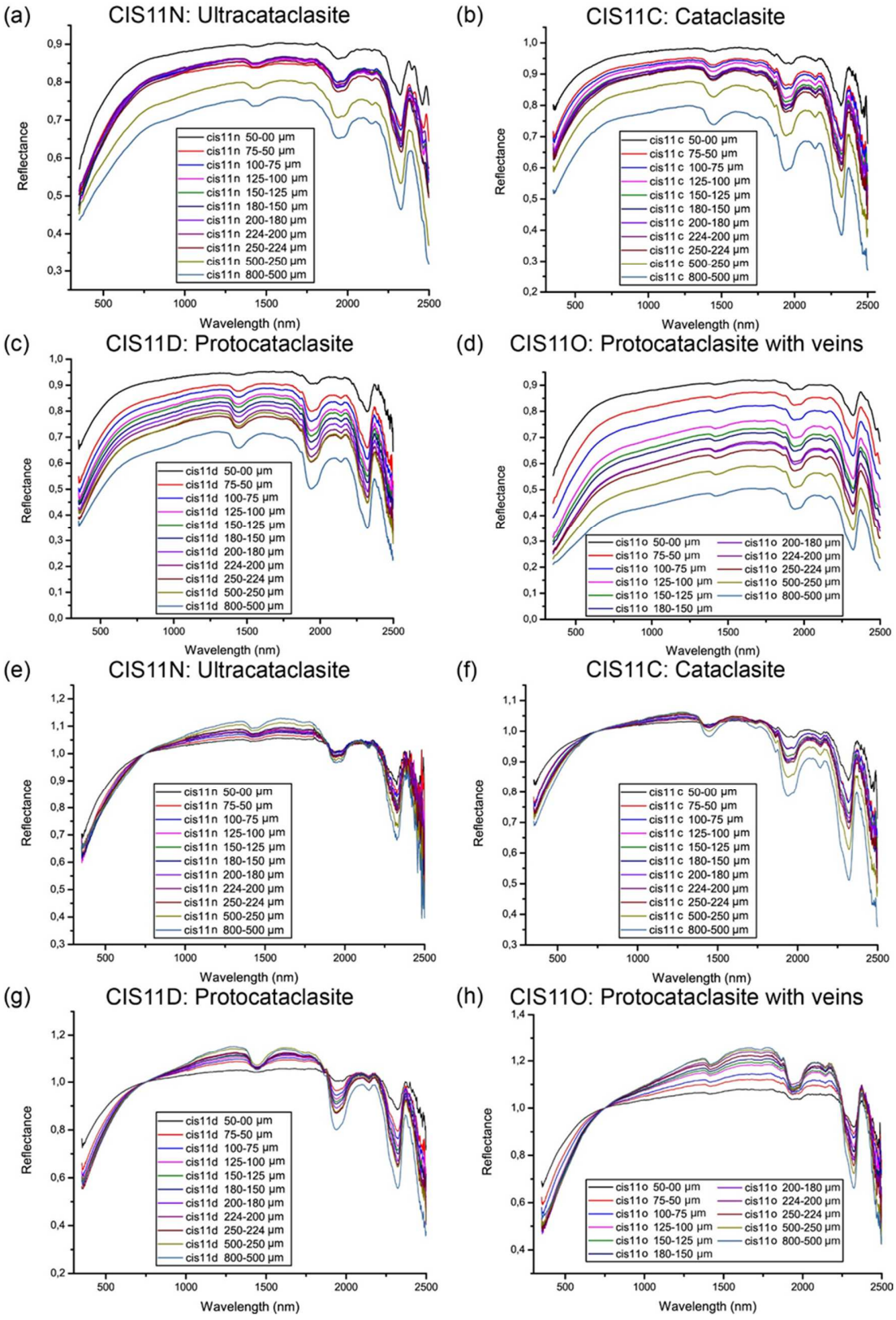
(a)
CIS11N: Ultracataclasite
Reflectance
Wavelength (nm)
cis11n 50-00 µm
cis11n 75-50 µm
cis11n 100-75 µm
cis11n 125-100 µm
cis11n 150-125 µm
cis11n 180-150 µm
cis11n 200-180 µm
cis11n 224-200 µm
cis11n 250-224 µm
cis11n 500-250 µm
cis11n 800-500 µm
(b)
CIS11C: Cataclasite
Reflectance
Wavelength (nm)
cis11c 50-00 µm
cis11c 75-50 µm
cis11c 100-75 µm
cis11c 125-100 µm
cis11c 150-125 µm
cis11c 180-150 µm
cis11c 200-180 µm
cis11c 224-200 µm
cis11c 250-224 µm
cis11c 500-250 µm
cis11c 800-500 µm
(c)
CIS11D: Protocataclasite
Reflectance
Wavelength (nm)
cis11d 50-00 µm
cis11d 75-50 µm
cis11d 100-75 µm
cis11d 125-100 µm
cis11d 150-125 µm
cis11d 180-150 µm
cis11d 200-180 µm
cis11d 224-200 µm
cis11d 250-224 µm
cis11d 500-250 µm
cis11d 800-500 µm
(d)
CIS11O: Protocataclasite with veins
Reflectance
Wavelength (nm)
cis11o 50-00 µm
cis11o 75-50 µm
cis11o 100-75 µm
cis11o 125-100 µm
cis11o 150-125 µm
cis11o 180-150 µm
cis11o 200-180 µm
cis11o 224-200 µm
cis11o 250-224 µm
cis11o 500-250 µm
cis11o 800-500 µm
(e)
CIS11N: Ultracataclasite
Reflectance
Wavelength (nm)
cis11n 50-00 µm
cis11n 75-50 µm
cis11n 100-75 µm
cis11n 125-100 µm
cis11n 150-125 µm
cis11n 180-150 µm
cis11n 200-180 µm
cis11n 224-200 µm
cis11n 250-224 µm
cis11n 500-250 µm
cis11n 800-500 µm
(f)
CIS11C: Cataclasite
Reflectance
Wavelength (nm)
cis11c 50-00 µm
cis11c 75-50 µm
cis11c 100-75 µm
cis11c 125-100 µm
cis11c 150-125 µm
cis11c 180-150 µm
cis11c 200-180 µm
cis11c 224-200 µm
cis11c 250-224 µm
cis11c 500-250 µm
cis11c 800-500 µm
(g)
CIS11D: Protocataclasite
Reflectance
Wavelength (nm)
cis11d 50-00 µm
cis11d 75-50 µm
cis11d 100-75 µm
cis11d 125-100 µm
cis11d 150-125 µm
cis11d 180-150 µm
cis11d 200-180 µm
cis11d 224-200 µm
cis11d 250-224 µm
cis11d 500-250 µm
cis11d 800-500 µm
(h)
CIS11O: Protocataclasite with veins
Reflectance
Wavelength (nm)
cis11o 50-00 µm
cis11o 75-50 µm
cis11o 100-75 µm
cis11o 125-100 µm
cis11o 150-125 µm
cis11o 180-150 µm
cis11o 200-180 µm
cis11o 224-200 µm
cis11o 250-224 µm
cis11o 500-250 µm
cis11o 800-500 µm

***Figure 4.6**: Reflectance spectra of powdered fault rock samples for the 11 particle size fractions ranging between < 50 µm and < 800 µm: (a) CIS11N (ultracataclasite); (b) CIS11C (cataclasite); (c) CIS11D (protocataclasite) and (d) CIS11O (protocataclasite with pervasive veins). Note how the spectral reflectance decreases with increasing particle size for each sample. (e-h) Reflectance spectra of the 11 particle sizes obtained for samples CIS11N, CIS11C, CIS11D and CIS11O and normalized at 750 nm to enphasize how the slope in the VIS (wavelengths < 750 nm) and NIR-SWIR (wavelengths >750 nm) spectral ranges increase with increasing particle size.*

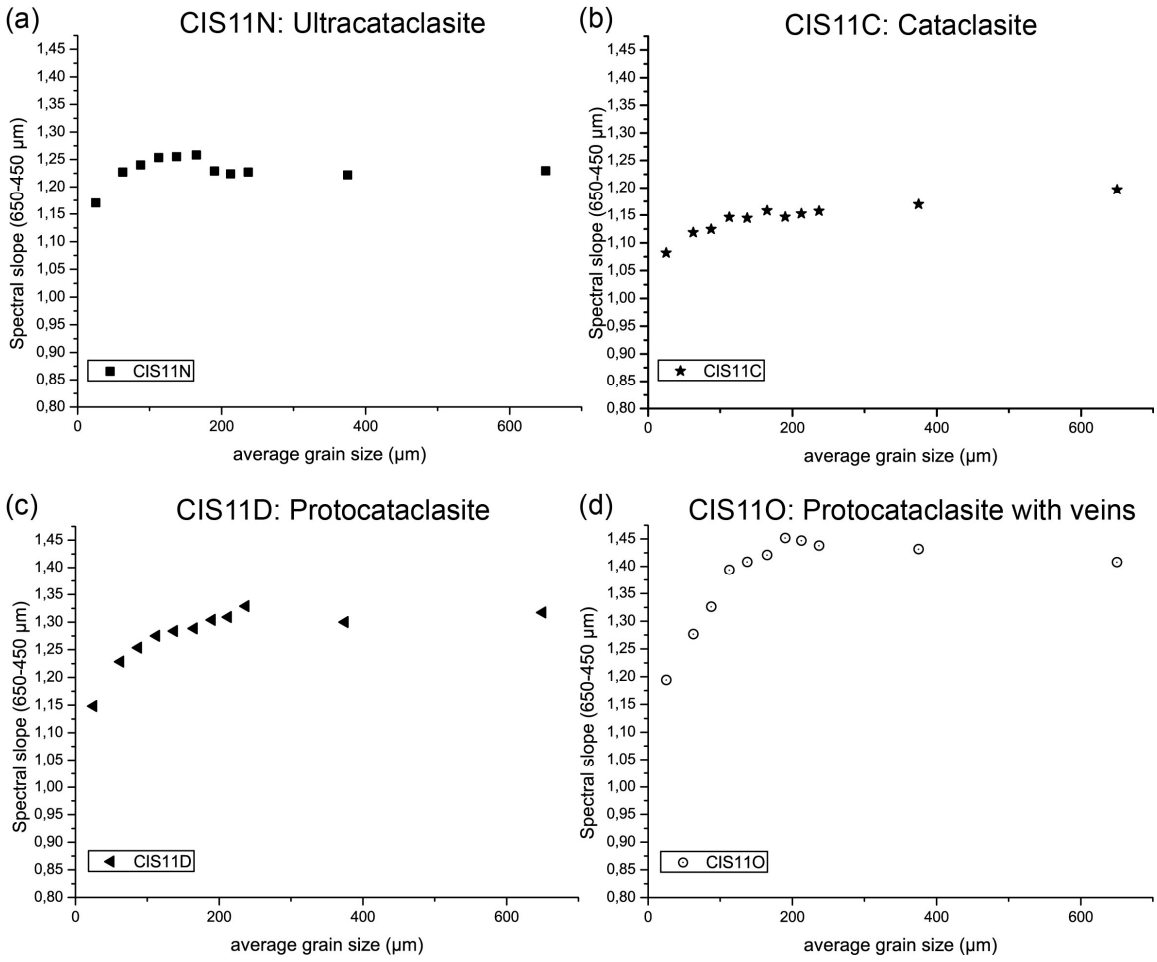

***Figure 4.7**: Spectral slope in the VIS range calculated for the 11 particle size fractions of samples: (a) CIS11N (ultracataclasite); (b) CIS11C (cataclasite); (c) CIS11D (protocataclasite) and (d) CIS11O (protocataclasite with pervasive veins). The values of the spectral slope (calculated as the ratio between the spectral reflectance at 650 nm and spectral reflectance at 450 nm) increase with increasing particle size.*

In particular, by increasing the particle size, the increment of the VIS spectral slope is progresivelly higher going from cataclasite to protocataclasite samples. Worth of note is the convergence of slope values among all the samples at thinner particle sizes (i.e. ultracataclasite-cataclasite clast size).

Figure 4.8 (A-D) shows the continuum removed spectra from which absorption band depths and band minimum positions were derived. In particular, *Table 4.2* shows that no significant shifting in the band absolute minimum positions are observed varying the particle size, but for each sample the considered absorption band depths (*band a*, *b* and *c*) increase with increasing particle size (*Figure 4.9*).

In *Figure 4.9*, it should be stressed how, among the different samples, the depths for *band a*, *b* and *c* show an increasing trend going from ultracataclasite (CIS11N) to cataclasite (CIS11D) and to protocataclasite (CIS11D) reflecting the original grain size reduction associated to fault comminution processes. This effect is not appreciable for the very fine powder fractions (i.e., 0-50 μm), because cataclasite and protocataclasite samples, once powdered at finer particle sizes, do not preserve their original texture and reach approximately the ultracataclasite clast size. Sample CIS110 (protocataclasite with pervasive veins) shows weaker absorptions for the band depths associated with the vibrational absorptions of OH^- and H_2O (*band a* and *b* respectively), suggesting for CIS11O, which shows dolomitic pervasive veins, a lower water content with respect to CIS11D sample (i.e., protocataclasite). By contrast for the carbonate band (2300 nm), CIS11O shows absorption band depths that are coherent with the protocataclasite (CIS11D) values. Moreover, the carbonate band depth variation with particle size for the four fault rock samples (*Figure 4.9C*) shows a convergence between protocataclasite (CIS11D) and cataclasite (CIS11C) at the largest grain sizes (500-800 μm). A potential explanation for this effect is that the analyzed cataclasite sample might derive from the comminution of a vein-bearing photolith. The veins are characterized by a low content of fluid inclusions and impurities yielding stronger absorptions for the carbonate band (2300 nm). This would

explain the anomalously high band depth value for CIS11C (*Figure 4.9C*). It should be also noted how the large particle fractions (i.e., 250-500 µm and 500-800 µm) were investigated by considering wide size ranges (i.e., of 250 and 300 µm), whereas the finer particles (i.e., < 250 µm) were sieved at tigher size intervals (i.e., of 25-30 µm). This implies that inhomogeneous size distributions are possible at the larger particle sizes, influencing the band depth.

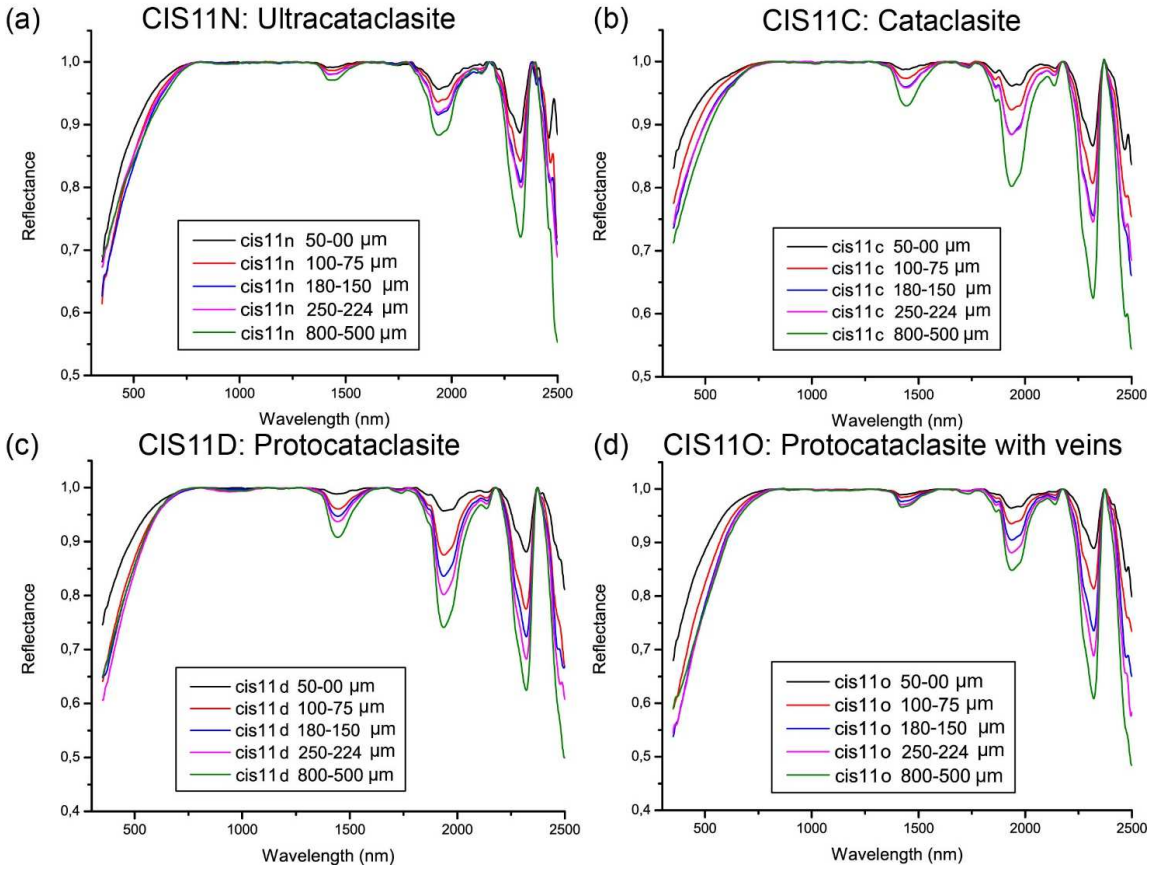

***Figure 4.8**: Continuum removed spectra of powdered fault rock samples (for simplicity we plot the spectra of five particle fractions): (a) CIS11N (ultracataclasite); (b) CIS11C (cataclasite); (c) CIS11D (protocataclasite) and (d) CIS11O (protocataclasite with pervasive veins).*

		1400 nm		1900 nm		2300 nm	
	Grain size (µm)	Band position (nm)	Band depth	Band position (nm)	Band depth	Band position (nm)	Band depth
CIS11N	00 - 50	1414	0,0087	1941	0,0437	2322	0,1131
	50 - 75	1439	0,0113	1943	0,0572	2325	0,1492
	75 - 100	1429	0,0135	1936	0,0638	2325	0,1581
	100 - 125	1434	0,0157	1937	0,0738	2324	0,1708
	125 - 150	1423	0,0185	1930	0,0732	2328	0,1836
	150 - 180	1427	0,0196	1937	0,0842	2326	0,1921
	180 - 200	1425	0,0178	1931	0,0753	2326	0,1877
	200 - 224	1422	0,0180	1928	0,0727	2328	0,1884
	224 - 250	1424	0,0202	1938	0,0805	2328	0,2001
	250 - 500	1424	0,0253	1938	0,1018	2324	0,2336
	500 - 800	1446	0,0289	1939	0,1168	2326	0,2792
CIS11C	00 - 50	1427	0,0125	1938	0,0385	2317	0,1336
	50 - 75	1448	0,0258	1937	0,0731	2319	0,1901
	75 - 100	1442	0,0268	1937	0,0763	2317	0,1931
	100 - 125	1439	0,0338	1936	0,0986	2319	0,2203
	125 - 150	1441	0,0336	1937	0,0966	2319	0,2178
	150 - 180	1439	0,0400	1937	0,1154	2319	0,2443
	180 - 200	1445	0,0354	1937	0,1024	2319	0,2270
	200 - 224	1446	0,0379	1937	0,1105	2318	0,2365
	224 - 250	1442	0,0416	1936	0,1158	2319	0,2545
	250 - 500	1445	0,0533	1938	0,1539	2319	0,2975
	500 - 800	1444	0,0701	1937	0,1980	2319	0,3754
CIS11D	00 - 50	1437	0,0115	1937	0,0430	2320	0,1189
	50 - 75	1446	0,0315	1938	0,1049	2320	0,1984
	75 - 100	1447	0,0393	1937	0,1247	2320	0,2249
	100 - 125	1444	0,0467	1937	0,1419	2321	0,2486
	125 - 150	1444	0,0505	1937	0,1544	2320	0,2620
	150 - 180	1445	0,0530	1937	0,1640	2321	0,2761
	180 - 200	1444	0,0576	1938	0,1789	2321	0,2960
	200 - 224	1446	0,0657	1937	0,1932	2321	0,3073
	224 - 250	1445	0,0628	1937	0,1981	2321	0,3177
	250 - 500	1443	0,0710	1937	0,2079	2321	0,3150
	500 - 800	1444	0,0920	1937	0,2588	2321	0,3758
CIS11O	00 - 50	1417	0,0107	1935	0,0357	2321	0,1109
	50 - 75	1421	0,0141	1936	0,0535	2322	0,1576
	75 - 100	1420	0,0156	1936	0,0647	2321	0,1863
	100 - 125	1421	0,0200	1937	0,0838	2322	0,2368
	125 - 150	1421	0,0218	1938	0,0914	2322	0,2535
	150 - 180	1421	0,0233	1937	0,0952	2321	0,2648
	180 - 200	1424	0,0279	1938	0,1143	2322	0,2923
	200 - 224	1422	0,0286	1934	0,1079	2321	0,2880
	224 - 250	1422	0,0296	1937	0,1189	2321	0,3115
	250 - 500	1423	0,0348	1938	0,1324	2321	0,3414
	500 - 800	1423	0,034	1938	0,1518	2321	0,3915

***Table 4.2**: Absorption band depths and band minimum positions calculated from the continuum removed spectra of powdered samples: CIS11N (ultracataclasite); CIS11C (cataclasite); CIS11D (protocataclasite) and CIS11O (protocataclasite with pervasive veins).*

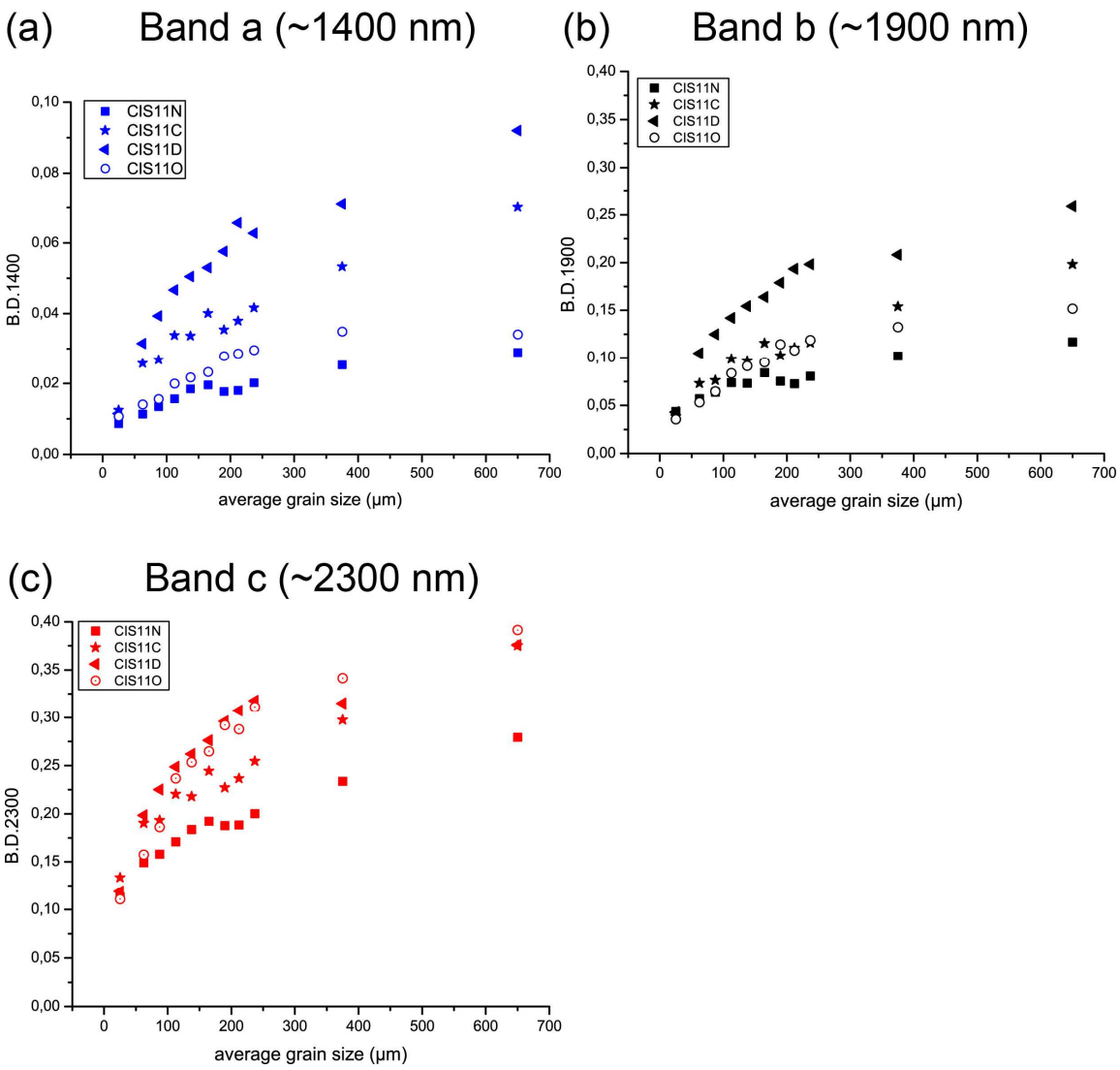

***Figure 4.9**: Band depth variations with increasing particle size for band a, band b and band c calculated from the continuum removed spectra of powdered samples: CIS11N (ultracataclasite); CIS11C (cataclasite); CIS11D (protocataclasite) and CIS11O (protocataclasite with pervasive veins). The depth of band a, b and c increases with increasing particle size for each sample. Additionally, the absorption band depth increases from ultracataclastite up to protocataclastite reflecting the original grain size reduction associated to fault comminution processes.*

4.2 Spectral characteristic of slabs

On the surface of each fault rock slab several reflectance spectra were acquired in order to investigate the spectral feature variability associated with different texitural characteristics (i.e., clast/matrix proportion, clast size and relative abundance of veins). In particular, for cataclasite samples (CIS11C and CIS11B) the selected measurement spots included: (i) portions characterized by prevalent matrix and clasts up to 1-2 mm in size, (ii) portions occupied by clasts up to 1 cm in size and (iii) areas at the transition between the former conditions. Similarly, the measured spots for protoclasite (CIS11D) were acquired on portions showing intense to moderate cataclasis (thus with a high to moderate matrix content) along with portions belonging to large unfractured clasts (up to 1 dm in size). The same criterion was employed for spots measured on protocataclasite with pervasive veins (CIS11O), for which portions belonging to large veins or at vein-protocataclasite trasitions were also acquired. By contrast, the high homogeneity of ultracataclasite (CIS11N) allows to choose measurement spots without any particular constraints. For simplicity, *Figure 4.10* displays only some of the representative spectrum measurement spots acquired on the slab surface. All the measured spectra show the diagnostic absorption features reported in *Figure 4.5* (i.e., *band a*, *b*, *c*, *d*), similarly to what has been observed for powdered fault rock samples (*Figure 4.6*). Nevertheless, it should be noted how the variation in spectral feature characteristics with the clast size is less systematic compared to the one observed for the powdered fault rock spectra. This is due to the intrinsic heterogeneities preserved in intact fault rock samples. As a result, for fault rock slabs the influence of clast size reduction on reflectance spectra might be not always straightforward. For each cataclasite sample (i.e., CIS11C and CIS11B), the spectral reflectance decreases with increasing clast size since spectra acquired in portions with prevalent matrix present higher reflectance with respect to the spectra acquired in clast-bearing areas (*Figure 4.10B and Figure 4.10C*). On the other hand, this relation is not always detectable considering ultracataclasite (*Figure 4.10A*) and protocataclasite samples (*Figure 4.10D and Figure 4.10E*). In fact, ultracataclasite samples

are highly homogeneous in terms of grain size, whereas protocataclasite samples show in some cases very complex texture with highly variable grain sizes.

Continuum removed spectra were generated to evaluate the variations in band absolute minimum positions and in absorption band depths. In particular, *Figure 4.11* reports the variations in band absolute minimum positions and in absorption band depths for cataclasite and protocataclasite samples (CIS11C and CIS11D respectively). These samples have been reported as an example, because they are representative of those fault rock classes that bear the higher clast size variability (i.e., clasts with different sizes are detectable in the hand specimen by visual check) and thus they might be potentially associated with the higher variability in terms of spectral feature characteristics.

For each of the considered samples, *Figure 4.11* shows that no significant shifting in band minimum positions has been found by considering the continuum removed spectrum derived from different measurement spots (i.e., different clast/matrix proportion and clast sizes). This aspect confirms the compositional homogeneity within the spot independently from the different clast/matrix ratios. Moreover, it should be noted how, for each absorption bands, the band depths associated with matrix-bearing measurement spots (red symbols in *Figure 4.11*) are lower than the band depths associated with clast-bearing measurement spots (blue symbols in *Figure 4.11*). This result is coherent to what has been observed for powdered fault rock samples in *Figure 4.9*. Similarly, *Figure 4.12* reports the reflectance spectra normalized at 750 nm for CIS11C and CIS11D fault rock slabs in order to evaluate the spectral slope variations. The spectral slope in the VIS (i.e., wavelengths < 750 nm) and NIR-SWIR (i.e., wavelengths >750 nm) spectral ranges increase with increasing clast size, similarly to what has been observed for powdered fault rock samples (*Figure 4.6* E-H, and *Figure 4.7*), but with a less-pronounced increase.

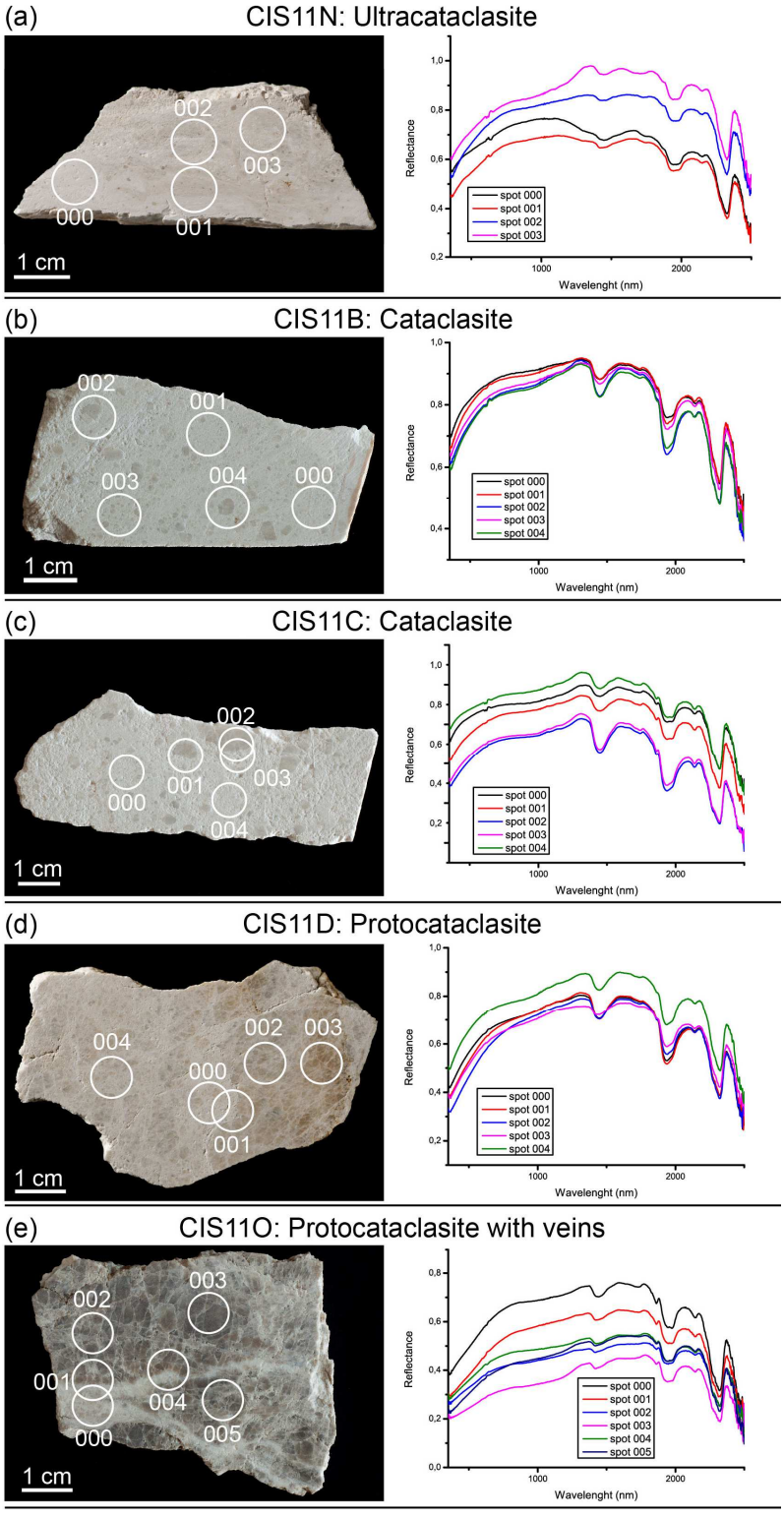
(a)
CIS11N: Ultracataclasite
002
003
000
001
1 cm
Reflectance
Wavelenght (nm)
spot 000
spot 001
spot 002
spot 003
(b)
CIS11B: Cataclasite
002
001
003
004
000
1 cm
spot 004
(c)
CIS11C: Cataclasite
(d)
CIS11D: Protocataclasite
(e)
CIS11O: Protocataclasite with veins
005

Figure 4.10*: Reflectance spectra acquired on the slab surface of samples: (a) CIS11N (ultracataclasite); (b) CIS11B (cataclasite); (c) CIS11C (cataclasite); CIS11D (protocataclasite) and CIS11O (protocataclasite with pervasive veins). For each sample, we report the position of some of the acquired spots and the reflectance spectrum associated with each spot. The measurement spots were selected in order to investigate the spectral feature variability associated with different texitural characteristics (i.e., clast/matrix proportion, clast size and relative abundance of veins).*

Errore. L'origine riferimento non è stata trovata. summarizes the differences in spectral feature characteristics existing between fault rock samples with different clast size: CIS11N (ultracataclasite), CIS11C (cataclasite) and CIS11D (protocataclasite). We exclude from this comparative evaluation sample CIS11O (protocataclasite with pervasive veins) because, due to the veining, this sample shows a particularly complex texture and a highly unpredictable response not necessarily related to grain size. For each sample we average those spectra that appear to be comparable because resulting from measurement spots with similar texitural characteristics (e.g., spots 000 and 004 for CIS11C sample because classified as matrix-bearing spots, *Figure 4.10*).

Errore. L'origine riferimento non è stata trovata.*A* displays the average spectra normalized at 750 nm, showing how the spectral slope in the VIS (i.e., wavelengths < 750 nm) and NIR-SWIR (i.e., wavelengths >750 nm) spectral ranges for matrix-bearing spots in cataclasite samples (000 and 004 spots of CIS11C sample, *Figure 4.10C*) is lower than the spectral slope observed for protocataclasite (CIS11D) and for clast-bearing spots in cataclasite samples (002 and 003 spots of CIS11C sample, *Figure 4.10C*), whereas CIS11N sample shows a more flattened average spectrum in term of spectral slopes. As illustrated for *Figure 4.12*, the variation in the spectral slopes is not well pronounced and systematic as observed for powdered fault rock samples (*Figure 4.6E-H* and *Figure 4.7*).

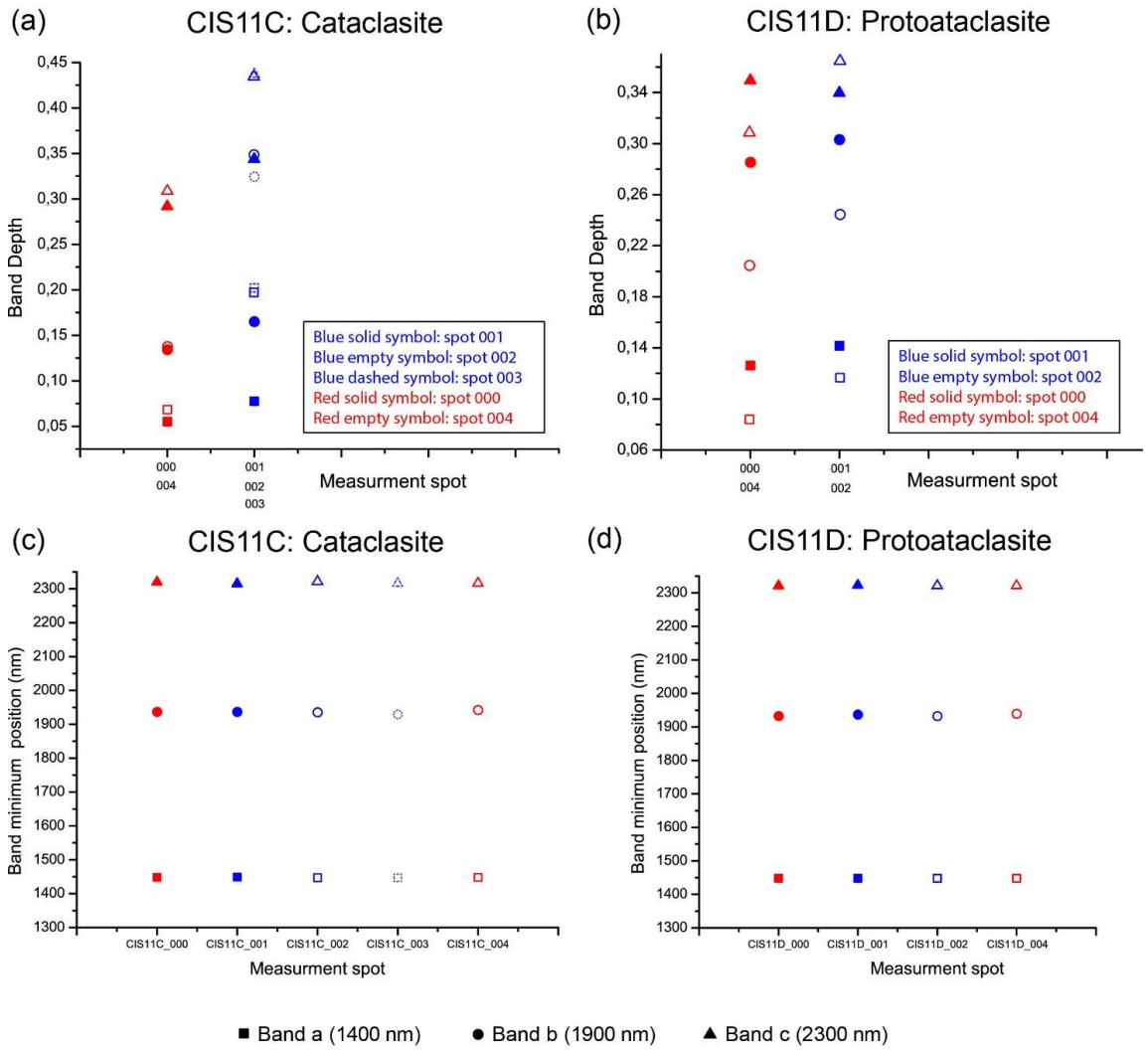

***Figure 4.11**: Absorption band depths (A, B) and band minimum positions (C, D) calculated from the continuum removed spectra of the slab surface of samples CIS11C (cataclasite) and CIS11D (protocataclasite). Red symbols indicate matrix-bearing spots whereas blue symbols represent clast-bearing spots as displayed in figure 4.10. Solid, empty or dashed symbols are refered to specific measurmet spots as indicated in the legend.*

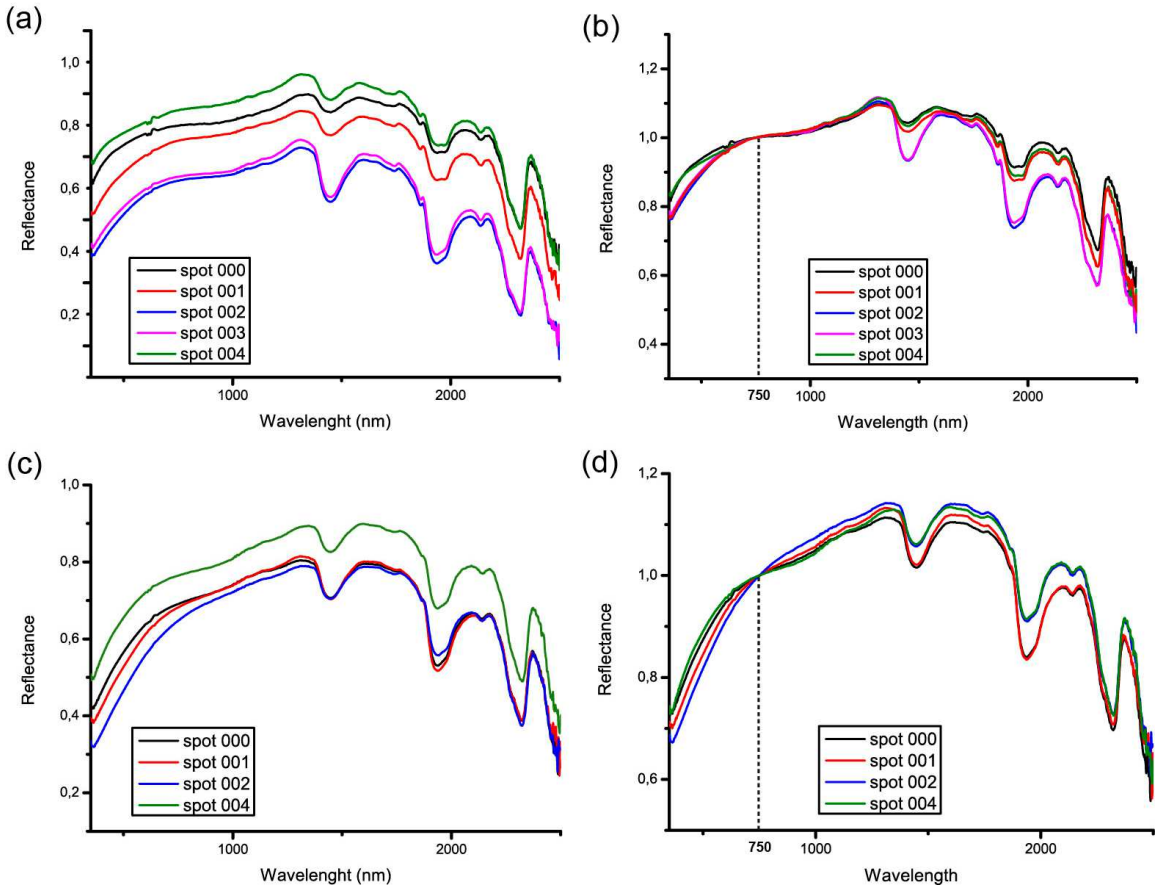

***Figure 4.12**: Reflectance spectra acquired on the slab surface of sample CIS11C (a) that have been normalized at 750 nm (b) in order to evaluate the spectral slope variations associated with different clast/matrix proportion in the measurement spots. Reflectance spectra acquired on the slab surface of sample CIS11D (c) that have been normalized at 750 nm (d) in order to evaluate the spectral slope variations associated with different clast/matrix proportion in the measurement spots.*

Figure 4.13B shows the continuum removed average spectra of the considered fault rock samples, from which band absolute minimum positions and absorption band depths (*Figure 4.13C*) can be derived. Band minimum position for the different absorption features does not shows significant shifting comparing the different samples (see table in *Figure 4.13*). The average spectrum for CIS11N sample (ultracataclasite) shows absorption band depths (***Errore. L'origine riferimento non è stata trovata.**C*), which are slightly smaller or comparable to those of CIS11C mean spectrum (cataclasite) resulting from the average of

matrix-bearing measurement spots (i.e., 000 and 004 spots, *Figure 4.10C*). In addition, the mean spectrum of CIS11C sample, which derives from the average of clast-bearing measurement spots (i.e., 002 and 003 spots, *Figure 4.10C*), shows absorption band depths that are coherently higher than those of CIS11N ultracataclasite and CIS11C cataclasite matrix-bearing average spectra (***Errore. L'origine riferimento non è stata trovata.****C*). Similarly, the average spectrum of CIS11D sample (protocataclasite) displays absorption band depths which are higher than those of CIS11N ultracataclasite and CIS11C cataclasite matrix-bearing average spectra, but lower than those of CIS11C cataclasite clast-bearing average spectrum (***Errore. L'origine riferimento non è stata trovata.****C*). This because the measurement spots on protocataclasite samples include pervasively fractured clasts and narrow cataclastic bands bearing an higher comminution intensity with respect to intact clasts in cataclasite samples (i.e., 002 and 003 clast-bearing measurement spots).

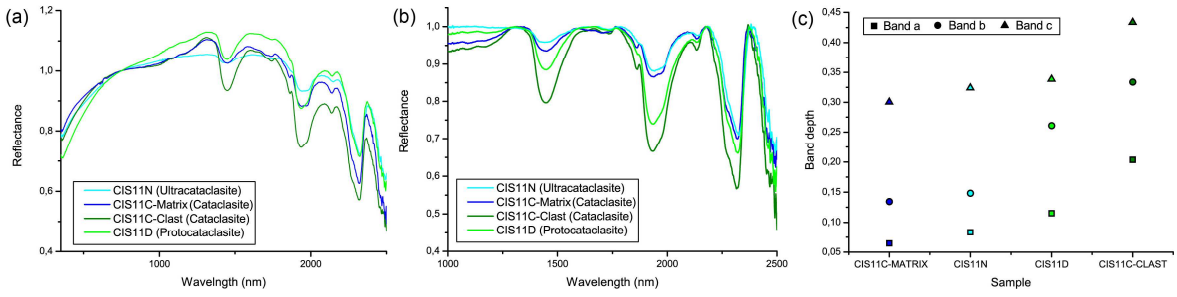

Sample	Band a (1400 nm)		Band b (1900 nm)		Band c (2300 nm)	
	Band position (nm)	Band depth	Band position (nm)	Band depth	Band position (nm)	Band depth
CIS11C (matrix spots)	1448	0,0647	1936	0,1345	2320	0,3002
CIS11N	1422	0,0835	1943	0,1484	2325	0,3241
CIS11D	1448	0,1151	1936	0,2608	2322	0,3386
CIS11C (clast spots)	1447	0,2037	1935	0,3337	2316	0,4335

Figure 4.13: *Comparison between reflectance spectra of different fault rock slabs. (a) Average reflectance spectra (we average those spectra that appear to be comparable because resulting from measurement spots with similar texitural characteristics) normalized at 750 nm. (b) Continuum removed average spectra. (c) Band depths (bands a, b, c) obtained from continuum removed average spectra. Table at the bottom reports the absolute band minimum positions and the band depths obtained from continuum removed average spectra for band a, b and c.*

5 Discussion on fault comminution effects on spectral response

The results of our spectral features analysis are in agreement with what expected from the optical theory (e.g., Adams and Filice, 1967; Hunt and Vincent 1968; Ross et al., 1969; Crown and Pieters 1987; Gaffey et al., 1993; Hapke, 1993; Harloff and Arnold 2001; Craig et al., 2007, 2008; Zaini et al, 2012). The variation in grain size influences the spectral characteristics in the VNIR and SWIR wavelength ranges, particularly in terms of reflectance, depth of absorption bands and spectral slope. Samples with small grain size provide more interfaces to the light during its optical path into the sample, increasing the amount of light being scattered out and thus showing high reflectance. This is in agreement to the observed increment of spectral reflectance with decreasing grain size (i.e., the size of clasts for slab samples and the size of particulates for powdered samples) outlined for powdered fault zone rocks and particularly evident for cataclasite sample slabs (*Figure 4.6A-D, Figure 4.10* and *Figure 12*). Samples with coarse grain size absorb more electromagnetic radiation penetrating to the grain surface than fine grain size samples and, as a result, the depth of absorption bands increases with increasing grain size (e.g., Harloff and Arnold 2001). For each absorption feature, the existence of an optimal particle size that maximizes its band depth is well stated in many studies regarding in particular crystal field absorptions (e.g., Gaffey et al., 1993; Hapke, 1993; Harloff and Arnold 2001). In this study, *Figure 4.9, Figure 4.11* and ***Errore. L'origine riferimento non è stata trovata.****D* show how the depth of the overtone *band a*, *b* and *c*, for both powdered and intact fault zone rocks, increases with increasing grain size (e.g., Crowley 1986), thus considering particle size from < 50 µm up to 800 µm (in the case of powdered samples) and matrix-bearing vs clast-bearing measurement spots for slab samples. Moreover, the performed spectral absorption features analysis outlines how, in general, the spectral slope increases with increasing grain size (*Figure 4.6E-H, Figure 4.7, Figure 4.12B, D* and ***Errore. L'origine riferimento non è stata trovata.****A*), in accordance with results from previous studies (e.g., Starukhina and Shkuratov 1996; Harloff and Arnold 2001). Finally, the position of both carbonate absorption bands in the SWIR region (*band c* and *d*) appears invariant to grain size fraction for powdered and

intact fault rock samples (*Table 4.2*, *Figure 4.11* and table within ***Errore. L'origine riferimento non è stata trovata.***), confirming results reported in previous studies (Gaffey, 1986; Van der Meer, 1995; Zaini et al., 2012). This is also valid for the position of OH^- and H_2O vibrational absorption bands (*band a* and *b*).

6 Evaluation and discussion of remote sensing potential for fault zone detection

Our reflectance spectroscopy analysis demonstrates how the grain size reduction resulting from fault zone evolution produces variations in spectral parameters of fault zone rocks. Therefore the remote sensing analysis in the VNIR-SWIR spectral range can be potentially applied to identify the spatial distribution and extent of fault core and damage zone domains. In the followings we critically discuss the potential of remote sensing techniques in the identification of fault zone domains considering the employment of different products: high spatial resolution multispectral satellite images (e.g., DigitalGlobe Worldview-3 satellite) and low altitude remote sensing hyperspectral sensor images (e.g., Headwall's Hyperspec® VNIR-SWIR sensor).

6.1 High spatial resolution multispectral satellite: Worldview-3

Worldview-3 satellite provides images with improved spatial and spectral resolution (*Table 4.3*), which might result adequate for the identification of fault zones yielding an extent comparable to the one of the VCFZ. In particular, Worldview-3 data have 8 SWIR bands with a spatial resolution of 3.70 m/pixel (*Table 4.3*). The reflectance spectra acquired with the Field-Pro Spectrometer (both on powdered and intact fault zone rocks) were resampled to Worldview-3 spectral resolution (see *Table 4.3*) in order to investigate if the effects of grain size reduction on the analyzed absorption features are still recognizable in the resampled spectra (*Figure 4.14* and *Figure 4.15*) and therefore, if fault rocks with different comminution degree can be potentially identified applying remote sensing analysis on Worldview-3 images. *Figure 4.14* and *Figure 4.15* (respectively for powder and slab samples) displays how the resampled spectra can be evaluated only in terms of spectral

slope, because the Worldview-3 spectral resolution does not allow to resolve the variations in the absorption band depths observed in the laboratory spectra. The variations in spectral slope of the resampled spectra have been evaluated by the calculation of different Band Ratios (BR) in the VNIR and SWIR spectral ranges: (i) BR 6/1; (ii) BR 11/8; (iii) BR 11/13 and (iv) BR 14/16. As a result, the value of the band ratios tends to decrease with decreasing grain size.

Sensor Bands (spectral range, nm)	8 Multispectral			
	Coastal:	400 - 450 nm	Red:	630 - 690 nm
	Blue:	450 - 510 nm	Red Edge:	705 - 745 nm
	Green:	510 - 580 nm	Near-IR1:	770 - 895 nm
	Yellow:	585 - 625 nm	Near-IR2:	860 - 1040 nm
	8 SWIR Bands			
	SWIR-1	1195 - 1225 nm	SWIR-5	2145 - 2185 nm
	SWIR-2	1550 - 1590 nm	SWIR-6	2185 - 2225 nm
	SWIR-3	1640 - 1680 nm	SWIR-7	2235 - 2285 nm
	SWIR-4	1710 - 1750 nm	SWIR-8	2295 - 2365 nm
Spatial resolution (m)	Multispectral Nadir	1,24 m		
	SWIR Nadir	3,70 m		

***Table 4.3**: Specific parameters for Worldview 3 satellite.*

This is particularly evident in the case of BR 14/16, which represents the slope of *band c* left side shoulder, and it is also confirmed by comparing the band ratio values obtained from different fault rock slabs (e.g., BR 14/16 tends to decrease from protocataclasite/clast bearing measurement spots to ultracataclasite/matrix bearing measurement spots, *Figure 4.16*). The other band ratios interest wider portions of the spectral range that are characterized by multiple absorption features, thus it is not possible to provide an univocal interpretation for these BR values (i.e., due to the superimposition of grain size effects either on absorption bands or spectral slope). However, as shown in *Figure 4.14* and *Figure 4.15,* proper band ratio analysis can be potentially able to spectrally identify fault zone domains.

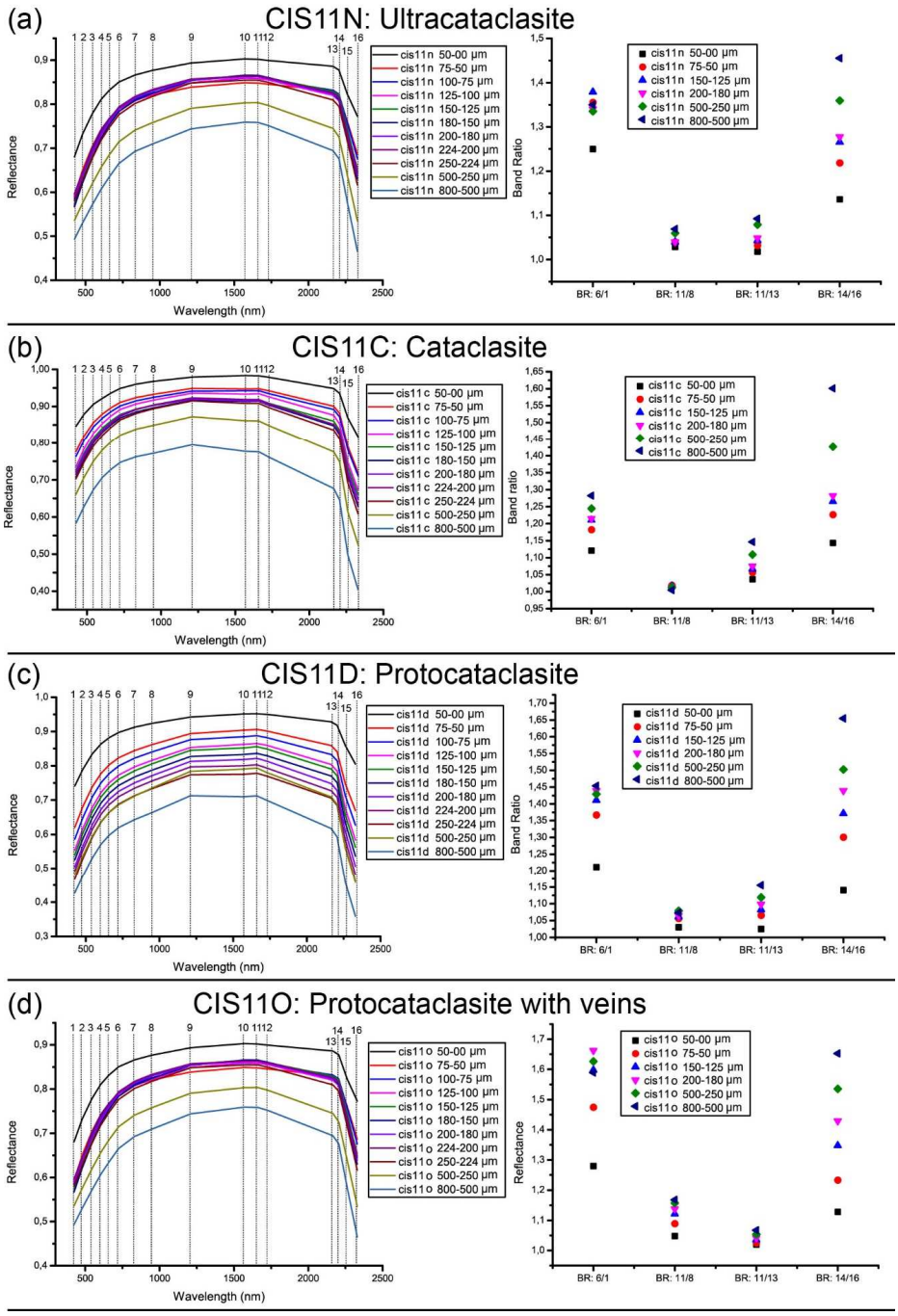

***Figure 4.14**: Reflectance spectra acquired on the 11 particle size fractions for each powdered fault rock samples (CIS11N, CIS11B, CIS11C, CIS11D and CIS11O) and resampled at the spectral resolution of Worldview-3 sensors. In addition, for each sample, we report the Band Ratios (BR) calculated to evaluate the variations in spectral slope of the resampled spectra (for simplicity we plot the BR for the spectra of six particle fractions).*

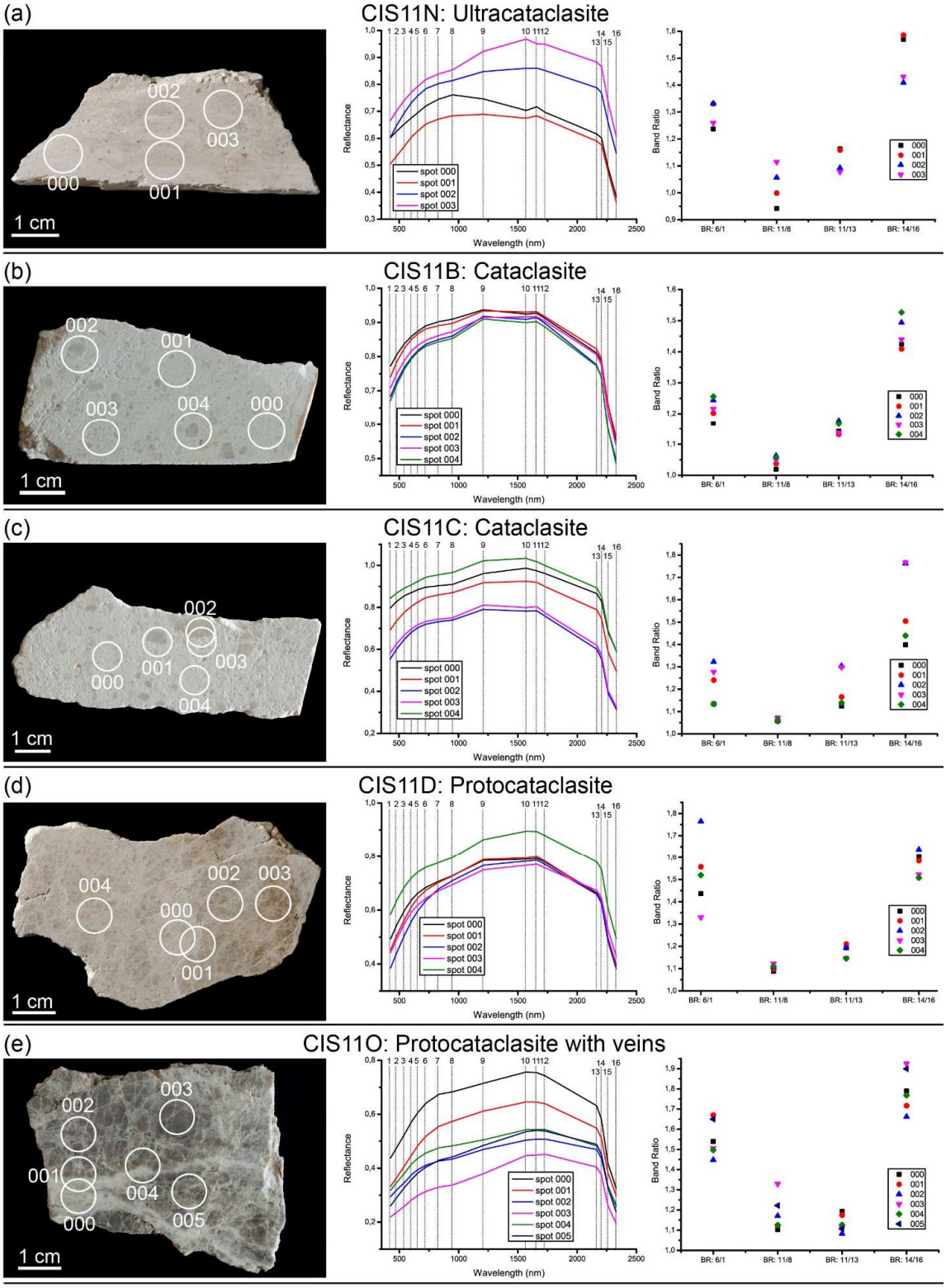
(a)
CIS11N: Ultracataclasite
002
003
000
001
1 cm
Reflectance
Wavelength (nm)
spot 000
spot 001
spot 002
spot 003
Band Ratio
BR: 6/1
BR: 11/8
BR: 11/13
BR: 14/16
(b)
CIS11B: Cataclasite
002
001
003
004
000
1 cm
spot 004
(c)
CIS11C: Cataclasite
002
001
003
000
004
1 cm
(d)
CIS11D: Protocataclasite
004
002
003
000
001
1 cm
(e)
CIS11O: Protocataclasite with veins
003
002
001
004
000
005
1 cm
spot 005

***Figure 4.15**: Reflectance spectra acquired on the slab surface of fault rock samples (CIS11N, CIS11B, CIS11C, CIS11D and CIS11O) and resampled at the spectral resolution of Worldview-3 sensors. In addition, for each sample, we report the Band Ratios (BR) calculated to evaluate the variations in spectral slope of the resampled spectra.*

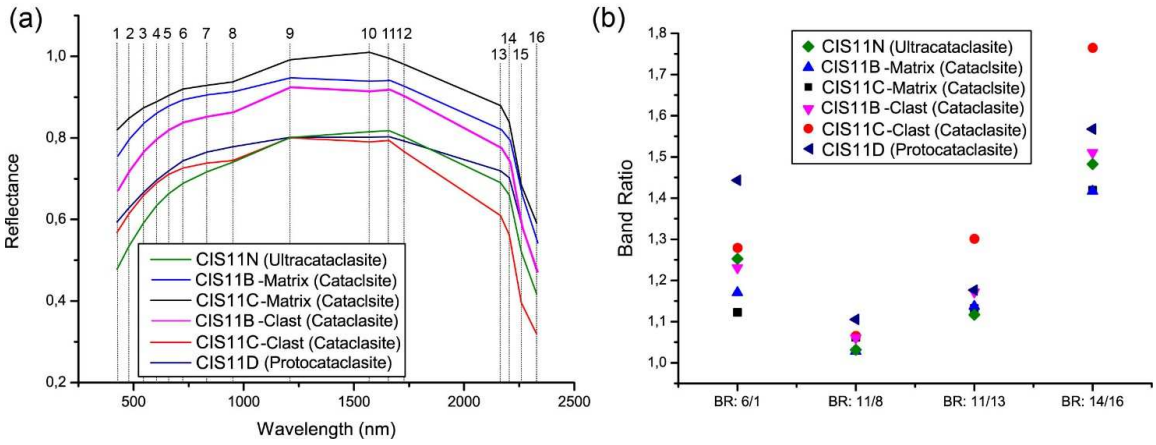

***Figure 4.16**: Comparison between reflectance spectra of different fault rock slabs resampled at the spectral resolution of Worldview-3 sensors. (a) Average reflectance spectra of fault rock slabs resampled at the spectral resolution of Worldview-3 sensors. (b) Band Ratios (BR) calculated to evaluate the variations in spectral slope of the resampled average spectra.*

In any case, it should be noted how Worldview-3 satellite images suffer of some shortcomings for applications aimed at identifying fault rock distribution. In particular, the absorption processes due to Earth atmosphere and the possible cloud coverage are limiting factors, common to any satellite optical imager looking at Earth surface. Finally, most of the high spatial resolution satellites available for the investigation of the earth surface have a commercial character that implies high product costs or subjection to several government regulations (e.g., while *Worldview-3 satellite* provides 3.7 m 8-band SWIR data, it can only be delivered at 7.5 m/pixel of resolution according to current US government regulations). This might prevent detection of fault zones whose thickness is generally of few tens of meters; for example, the VCFZ core is represented by a ca. 40 m thick band lining the master fault.

6.2 Low altitude hyperspectral sensor: Hyperspec® VNIR-SWIR sensor

Among the recently grown low altitude remote sensing sensors, the Hyperspec® VNIR-SWIR sensor (Headwall Photonics production) represents a dual camera suitable for aircraft and UAV acquisitions. Hyperspec® VNIR-SWIR covers the 400-2500 nm spectral range with 271 bands in the VNIR (400-1000 nm) and 267 bands in the SWIR (900-2500 nm), while the low acquisition altitude ensure a high spatial resolution (*Table 4.4*).

Dual-Sensor VNIR-SWIR Package		
Spectral Range	VNIR (400-1000nm)	SWIR (900-2500nm)
Spectral Bands	271	267
Dispersion per pixel (nm/pixel)	2.2	6

Table 4.4*: Specific parameters for Dual-sensor Hyperspec® VNIR-SWIR Package (Headwall Photonics production).*

Figure 4.17 displays the spectra of an intact fault rock slab (i.e., CIS11B cataclasite sample) resampled at the Hyperspec® VNIR-SWIR sensor spectral resolution (*Table 4.4*). The Hyperspec® VNIR-SWIR sensor allows the full resolution of spectral feature parameters because of its high spectral resolution, comparable to the one of the Field-Pro Spectrometer used in this study. Therefore, Hyperspec® VNIR-SWIR sensor images might show a high potential for the remote sensing identification of fault zone rock domains, especially because the spectra acquired in the laboratory can be used as reference spectra during the application of supervised classification procedures (e.g., Spectral Angle Mapper classification, Kruse et al., 1993) aimed at mapping fault rock with different grain sizes.

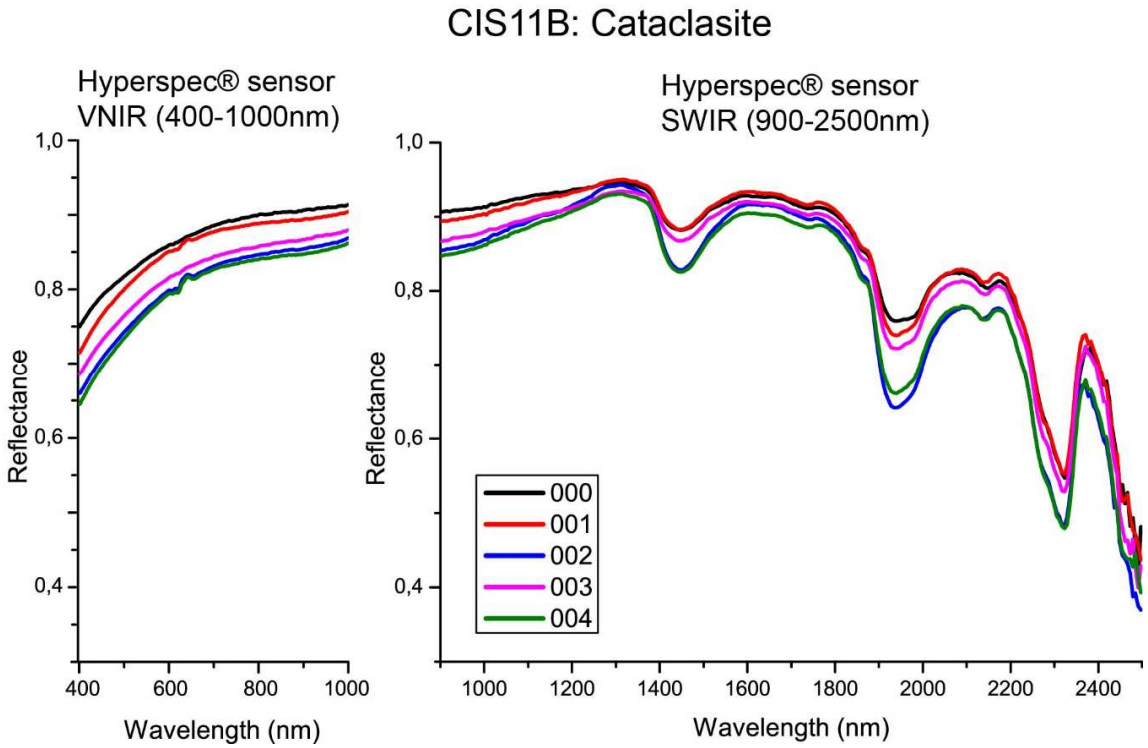

***Figure 4.17**: Spectra of CIS11B fault rock slab resampled at the Hyperspec® VNIR-SWIR sensor spectral resolution.*

7 Conclusions

The spectral features analysis performed on fault rock samples (i.e., ultracataclasite, cataclasite and protocataclasite) collected at increasing distances from the Vado di Corno Fault Zone core demonstrates how the variation in grain size due to fault zone evolution influences the absorption feature characteristics in the VNIR and SWIR wavelength ranges. The analysed samples bear a homogeneous and constant composition (i.e., semi-quantitative XRPD analysis), hence the observed spectral feature variations are spectrally superimposed on constant compositional information (i.e., absorption features) and are solely ascribable to grain size reduction due to fault development. In particular, spectral reflectance, depth of absorption bands and spectral slope vary systematically with the grain size considering the spectra of both crushed and intact fault rock slabs. The spectral analysis of crushed fault rocks revealed that with increasing grain size: (i) reflectance decreases; (ii)

main absorption band depths increase (i.e., absorption bands at ca. 1400 nm, 1900 nm and 2300 nm) and (iii) spectral slopes evaluated in the VIS (i.e., wavelengths < 750 nm) range increase. These spectral parameters vary systematically according to the different particle fractions obtained by crushing fault rock samples, but their variations also reflect the original grain size reduction associated to fault comminution processes (i.e., considering each particle sizes individually, the band depth of the observed absorption features shows an increasing trend going from ultracataclasite to protocataclasite samples). The spectral feature characteristics of fault rock slabs vary coherently to the ones of the powdered samples, although less systematically because of the intrinsic heterogeneities preserved in intact fault rock slabs. In particular, the spectral analysis shows how for each fault rock slabs the main absorption band depths increase with increasing clast size both within the same slab surface (i.e., by comparing matrix-bearing and clast-bearing measurement spots) and between fault rock samples showing different clast sizes (i.e., ultracataclasite, cataclasite and protocataclasite samples).

These results outline for the first time the correlation between the variations in fault zone rock spectral parameters and the grain size reduction resulting from fault-related comminution processes. As a consequence, relying on this correlation, the remote sensing analysis in the VNIR-SWIR spectral range can be potentially applied to identify the spatial distribution and extent of fault core and damage zone domains. The potential of remote sensing techniques in the identification of fault zone domains have been critically evaluated by considering the employment of different high spatial resolution products: multispectral satellite images (e.g., DigitalGlobe Worldview-3 satellite) and low altitude remote sensing hyperspectral sensor images (e.g., Headwall's Hyperspec® VNIR-SWIR sensor). The reflectance spectra acquired in the laboratory have been resampled to the spectral resolution of the considered products. The Worldview-3 spectral resolution does not allow resolving the absorption band depth variations observed in the laboratory spectra, but the variation in the spectral characteristics due to the fault-related comminution processes can be evaluated in terms of spectral slope by applying proper band ratios. By contrast, the

considered hyperspectral sensor bears a spectral resolution that is comparable to the one of laboratory spectrometer. Therefore, the low altitude remote sensing hyperspectral sensor shows a high potential for the remote sensing identification of fault zone domains. In this view, the laboratory spectra could be successfully used as end member spectra in a supervised classification procedure (e.g., Spectral Angle Mapper classification) on hyperspectral images.

References

Adamoli, L., Calamita, F., Pelorosso, M., 2003. Itinerario No 2-Gran Sasso d'Italia: dai Prati di Tivo ai Prati di Tivo attraverso il ghiacciaio del Calderone, il Corno Grande, Campo Pericoli e la Val Maone. In: Guide Geologiche Regionali, Abruzzo: 102-112, BE-MA ed., Lodi (MI).

Adamoli, L., Calamita, F., Pizzi, A., 2012. Note Illustrative del Foglio 349 "G. Sasso" della Carta Geologica d'Italia alla scala 1: 50.000. ISPRA, Roma.

Adams, J.B., Filice, A.L., 1967. Spectral reflectance 0.4 to 2:0 µm of silicate rock powders. Journal of Geophysical Research 72, 5705–571

Agosta, F., Kirschner, D., 2003. Fluid conduits in carbonate-hosted seismogenic normal faults of central Italy. Journal of Geophysical Research 108 (B4), 2221, doi: 10.1029/2002JB002013.

Billi, A., Salvini, F., Storti, F., 2003. The damage zone-fault core transition in carbonate rocks: implications for fault growth, structure and permeability. Journal of Structural Geology 25 (11), 1779–1794.

Bistacchi, A., Massironi, M., 2000. Post-nappe brittle tectonics and kinematic evolution of the northwestern Alps: an integrated approach. Tectonophysics 327, 267–292.

Bistacchi, A., Massironi, M., Menegon, L., 2010. Three-dimensional characterization of a crustal-scale fault zone: The Pusteria and Sprechenstein fault system (Eastern Alps). Journal of Structural Geology 32, 2022–2041, doi: 10.1016/j.jsg.2010.06.003.

Blount, G., Smith, M.O., Adams, J.B., Greeley, R., Christensen, P.R., 1990. Regional Aeolian dynamics and sand mixing in the Gran Desierto: evidence from Landsat Thematic Mapper images. Journal of Geophysical Research 95, 15463–15482.

Brune, J.N., 2001. Fault normal dynamic loading and unloading: an explanation for ''non-gouge''rock powder and lack of fault-parallel shear bands along the San Andreas fault. Eos Trans. American Geophysical Union 82 (47). Fall Meet. Suppl., Abstract S22B-0655.

Caine, J.S., Evans, J.P., Forster, C.B., 1996. Fault zone architecture and permeability structure. Geology 24, 1025–1028.

Carli, C., Serventi, G., Sgavetti, M., 2015. VNIR spectral characteristics of terrestrial igneous effusive rocks: Mineralogical composition and the influence of texture. In: Platz, T., Massironi, M., Byrne, P.K., Hiesinger, H. (Eds.), Volcanism and Tectonism Across the

Inner Solar System, vol. 401. Geological Society, London, Special Publications, 139–158, doi:http://dx.doi.org/10.1144/SP401.19

Chambon, G., Schmittbuhl, J., Corfdir, A., Orellana, N., Diraison, M., Géraud, Y., 2006. The thickness of faults: From laboratory experiments to field scale observations. Tectonophysics 426, 77–94, doi: 10.1016/j.tecto.2006.02.014.

Chester, F.M., Evans, J.P., Biegel, R.L., 1993. Internal structure and weakening mechanisms of the San Andreas fault. Journal Geophysical Research 98, 771–786.

Childs, C., Manzocchi, T., Walsh, J.J., Bonson, C.G., Nicol, A., Schöpfer, M.P., 2009. A geometric model of fault zone and fault rock thickness variations. Journal of Structural Geology 31 (2), 117–127.

Clark, R.N., & Roush, T.L., 1984. Reflectance spectroscopy - Quantitative analysis techniques for remote sensing applications. Journal Geophysical Research 89, 6329–6340, doi:10.1029/JB089iB07p06329.

Clark, R.N., King, T.V.V., Klejwa, M., Swayze, G.A., Vergo, N., 1990. High spectral resolution reflectance spectroscopy of minerals. Journal of Geophysical Research 95 (89), 12653, doi:10.1029/JB095iB08p12653

Clark, R.N., 1999. Spectroscopy of rocks and minerals and principles of spectroscopy. In: Rencz, A.N. (Ed.), Manual of Remote Sensing, Volume 3, Remote Sensing for Earth Science. John Wiley and Sons, New York, 3–58.

Cooper, C., Mustard, J., 1999. Effects of Very Fine Particle Size on Reflectance Spectra of Smectite and Palagonitic Soil. Icarus, 142, 557–570, doi:10.1006/icar.1999.6221

Craig, M.A., Cloutis, E.A., Bailey, D.T., 2007. The effects of grain size, < 45–1000 μm, on the reflectance spectrum of planetary analogs from 0.35–2.5 μm. Lunar and Planetary Science 38. Abstract 1356.

Craig, M., Cloutis, E., 2008. The effects of grain size, < 10 μm-4.75 mm, on the reflectance spectrum of planetary analogs from 0.35-2.5 μm. Lunar and Planetary Science 39. Abstract 2082.

Crown, D.A., Pieters, C.M., 1987. Spectral properties of plagioclase and pyroxene mixtures and the interpretation of lunar soil spectra. Icarus 72, 492–506.

Crowley, J.K., 1986. Visible and near-infrared spectra of carbonate rocks: Reflectance variations related to petrographic texture and impurities. Journal of Geophysical Research 91, 5001–5012, doi:10.1029/JB091iB05p05001.

Demurtas, M., Fondriest, M., Balsamo, F., Clemenzi, L., Storti, F., Bistacchi, A., Di Toro, G., 2016. Structure of a normal seismogenic fault zone in carbonates: The Vado di Corno Fault, Campo Imperatore, Central Apennines (Italy). Journal of Structural Geology, 90(August), 185–206. doi:10.1016/j.jsg.2016.08.004

Faulkner, D., Jackson, C., Lunn, R., Schlische, R., Shipton, Z., Wibberley, C., Withjack, M., 2010. A review of recend development concerning the structure, mechanics and fluid flow properties of fault zones. Journal of Structural Geology 32 (11), 1557–1575.

Faulkner, D.R., Lewis, A.C., Rutter, E.H., 2003. On the internal structure and mechanics of large strike-slip fault zones: field observations of the Carboneras fault in southeastern Spain. Tectonophysics 367 (3), 235–251, doi:10.1016/S0040-1951(03)00134-3

Fondriest, M., Smith, S.A.F., Di Toro, G., Zampieri, D., Mittempergher, S., 2012. Fault zone structure and seismic slip localization in dolostones, an example from the Southern Alps, Italy. Journal of Structural Geology 45, 52–67, doi:10.1016/j.jsg.2012.06.014

Gaffey, S.J., 1986. Spectral reflectance of carbonate minerals in the visible and near infrared (0.35–2.55 microns): Calcite, aragonite, and dolomite. American Mineralogist, 71, 151–162.

Gaffey, M.J., McFadden, L.A., Nash, D., Pieters, C.M., 1993. Ultravio-let, visible, and near-infrared spectroscopy: Laboratory spectra of geologic materials. In: Pieters, C.M., Englert, P. J. (Eds.), Remote Geochemical Analysis: Elemental and Mineralogical Composition. Cambridge University Press, Cambridge, 43–78.

Ghrefat, H.A., Goodell, P.C., Hubbard, B.E., Langford, R.P., Aldouri, R.E., 2007. Modeling grain size variations of aeolian gypsum deposits at White Sands, New Mexico, using AVIRIS imagery. Geomorphology, 88, 57–68, doi:10.1016/j.geomorph.2006.10.013

Hapke, B., 1993. Theory of Reflectance and Emittance Spectroscopy. Cambridge University Press, Cambridge.

Harloff, J., Arnold, G., 2001. Near-infrared reflectance spectroscopy of bulk analog materials for planetary crust. Planetary and Space Science, 49, 191–211. doi:10.1016/S0032-0633(00)00132-X

Hunt, G.R., Vincent, R.K., 1968. The behavior of spectral features in the infrared emission from particulate surfaces of various grain sizes. Journal of Geophysical Research, 73, 6039–6046, doi:10.1029/JB073i018p06039.

Kavak, K.S., Inan, S., 2002. Enhancement Facilities of SPOT XS Imagery in Remote Sensing Geology: An Example from the Sivas Tertiary Basin (Central Anatolia/Turkey). International Journal of Remote Sensing, 23 (4), 701–710.

Kruse, F.A., Lefkoff, A.B., Boardman, J.W., Heidebrecht, K.B., Shapiro, A.T., Barloon, P.J., Goetz, A.F.H., 1993. The Spectral Image-Processing System (Sips)-interactive visualization and analysis of imaging spectrometer data. Remote Sensing of Environment 44, 145–163.

Marone, C., Scholz, C., 1989. Particle-size distribution and microstructures within simulated gouge. Journal of Structural Geology 11, 799–814.

Masoud, A.A., Koike, K., 2011. Auto-detection and integration of tectonically significant lineaments from SRTM DEM and remotely-sensed geophysical data. ISPRS Journal of Photogrammetry and Remote Sensing 66, 818–83.

Massironi, M., Bertoldi, L., Calafa, P., Visonà, D., Bistacchi, A., Giardino, C., Schiavo, A., 2008. Interpretation and processing of ASTER data for geological mapping and granitoids detection in the Saghro massif (eastern Anti-Atlas, Morocco). Geosphere 4, 736–759.

139Milana, J.P., 2000. Characterization of alluvial bajada facies distribution using TM imagery: Sedimentology 47, 741–760, doi:10.1046/j.1365-3091.2000.00297.x.

Monzawa, N., Otsuki, K., 2003. Comminution and fluidization of granular fault materials: implications for fault slip behavior. Tectonophysics 367, 127–143.

Muto, J., Nakatani, T., Nishikawa, O., Nagahama, H., 2015. Fractal particle size distribution of pulverized fault rocks as a function of distance from the fault core. Geophysical Research Letters 42(10), 3811–3819, doi:10.1002/2015GL064026.

Nolin, A.W., Dozier, J., 2000. A Hyperspectral Method for Remotely Sensing the Grain Size of Snow. Remote Sensing of Environment 216, 207–216.

Okin, G.S., Painter, T.H., 2004. Effect of grain size on remotely sensed spectral reflectance of sandy desert surfaces. Remote Sensing of Environment 89, 72–280, doi: 10.1016/j.rse.2003.10.008.

Painter, T.M., Roberts, D.A., Green, R.O., Dozier, J., 1998. The effect of grain size on spectral mixture analysis of snow-covered area from AVIRIS data. Remote Sensing of Environment 65, 320–332.

Painter, T.H., Rittger, K., McKenzie, C., Slaughter, P., Davis, R.E., Dozier, J., 2009. Retrieval of subpixel snow covered area, grain size, and albedo from MODIS. Remote Sensing of Environment 113, 868–879, doi:10.1016/j.rse.2009.01.001.

Paisley, E.C.I., Lancaster, N., Gaddis, L.R., Greeley, R., 1991. Discrimination of active and inactive sand from remote sensing: Kelso dunes, Mojave Desert, California. Remote Sensing of Environment 37, 153–166.

Ross, H.P., Adler, J.E., Hunt, G.R., 1969. A statistical analysis of the reflectance of igneous rocks from 0.2 to 2.65 μm. Icarus 11, 46–54.

Shipman, H., Adams, J.B., 1987. Detectability of minerals on desert alluvial fans using reflectance spectra. Journal of Geophysical Research 92, 10391–10402.

Sibson, R., 1977. Fault rocks and fault mechanisms, Journal of the Geological Society, London 133, 191–213.

Starukhina, L.V., Shkuratov, Y.G., 1996. Particle size dependence of spectral slope and the depth of absorption bands: implication for lunar soils. Abstracts of the 24th Vernadsky-Brown Microsymposium in Moscow, 90–91

Storti, F., Aldega, L., Balsamo, F., Corrado, S., Del Monaco, F., Di Paolo, L., Mastalerz, M., Monaco, P., Tallini, M., 2013. Evidence for strong middle Pleistocene earthquakes in the epicentral area of the 6 April 2009 L'Aquila seismic event from sediment paleofluidization and overconsolidation. Journal of Geophysical Research 118 (7), 3767–3784.

Tesei, T., Collettini, C., Viti, C., Barchi, M.R., 2013. Fault architecture and deformation mechanisms in exhumed analogues of seismogenic carbonate-bearing thrusts. Journal of Structural Geology 55, 167–181.

Turcotte, D.L., 1986. Fractals and fragmentation. Journal of Geophysical Research 91, 1921–1926.

Van der Meer, F.D. 1995. Spectral reflectance of carbonate mineral mixtures and bidirectional reflectance theory: Quantitative analysis techniques for application in remote sensing. Remote Sensing Reviews, 13, 67–94.

Wibberley, C.A., Yielding, G., Di Toro, G., 2008. Recent advances in the under- standing of fault zone internal structure: a review. Geological Society of London, Special Publications 299 (1), 5–33

Zaini, N., Van Der Meer, F., Van Der Werff, H., 2012. Effect of grain size and mineral mixing on carbonate absorption features in the SWIR and TIR wavelength regions. Remote Sensing 4, 987–1003, doi:10.3390/rs4040987

5. Conclusions

Using a multidisciplinary approach, which includes structural field investigations, stress inversion, normalised slip tendency analysis, spectroscopic measurement and spectral features analysis, the present study focused on three main topics: i) the reconstruction of polyphase brittle tectonic evolution accommodated by fault zones dissecting lithologically heterogeneous rock domains; ii) the estimate of the degree of mechanical anisotropy associated with pre-existing planar discontinuities (metamorphic foliations and inherited faults) steering their brittle reactivation process; iii) the spectral characterization of fault zone rocks aimed at inferring the distribution of fault zone domains by means of remote sensing techniques.

The main results retrieved from this research can be summarized as follows:

i. Polyphase brittle tectonics within lithologically heterogeneous rock domains can be efficiently unrevealed by applying a paleostress inversion analysis that carefully considers each of the analyzed fault zones and the different mechanical behavior of the lithological domains they deform;
ii. application of bootstrapping statistical approach on reduced stress tensors proved to be a useful means of assessing the homogeneity of paleostress inversion results and thus identifying possible local stress perturbation (i.e., necessary to avoid the erroneous identification of tectonic phases);
iii. the brittle regional polyphase deformation history of the Sierras de Córdoba of central Argentina has been unrevealed and tested against existing time and regional constraints. It appears to be dominated by two extensional episodes (σ_3 oriented NE and NW, respectively) spanning the Early Triassic to Early Cretaceous time interval, followed by a compressional paleostress regime (σ_1 oriented ENE), which is compatible with the present-day Andean convergence;
iv. normalised slip tendency analysis, integrated with paleostress reconstructions and detailed meso- and micro-structural observations, can be considered a reliable

method to investigate and constrain the weakness of pre-existing anisotropies directly at a regional scale (10^4-10^3 m).

v. The general low values estimated for friction coefficient for slip along foliations (μs) and along pre-existing faults (μf) account for an absolute weakness mechanism on metamorphic foliations and gouge bearing faults in Sierra de Córdoba basement, as failure along these inherited planar mechanical discontinuities develops at lower differential stresses than those required to reach the Coulomb failure envelope for Andersonian faulting. This is in agreement with the behavior of similar foliated and fault related rocks assessed by previous laboratory experiments, but here it is proved that these results can be extended, although with some caution, to regional scales.

vi. The grain size reduction resulting from fault-related comminution processes on mineralogically homogenous bedrocks (carbonates in this case) influences the spectral signatures of fault rock samples, which absorption feature parameters vary systematically with the grain size in VNIR and SWIR wavelength ranges;

vii. Remote sensing analysis, based on carbonate fault rock reflectance spectrum variabilities due to comminution processes, has a good potential in the identification of the spatial distribution and extent of fault core and damage zone domains, especially if low altitude remote sensing hyperspectral sensor are employed.

Appendix A. Rotational optimization procedure

In this work, stress inversion was performed from the measured field dataset (*Figure A.1* and *Table A.1*) by using the Win Tensor program (Delvaux, 2011) and following a two-step procedure (i.e., application of improved right-dihedron method and subsequently of iterative rotational optimization). During the rotational optimization procedure the stress tensor is tested and further refined by a 4D grid search involving successive rotations of the tensor around the three principal stress axes (σ1, σ2 and σ3) together with an equivalent testing of the stress ratio R. Rotation around each stress axis is aimed at minimizing the value of a specific misfit function. In this work function F5 was used to simultaneously minimise the misfit angle between the observed and modelled slip line on the plane and promote reactivation by minimizing the resolved normal stress and maximizing the resolved shear stress on the plane. The minimum value of the misfit function for each run is determined by taking the minimum of the polynomial regression curve adjusted to the results of each test. The regression curves (i.e., third to sixth columns in *Figure A.2* to *Figure A.6*) are a graphic representation with the rotation angle as abscissa and the value of the misfit function as ordinate, which allow estimating the stability of the obtained stress axis and R values (Delvaux, 2012). The regression curves can exhibit a deep minimum, whose depth is quantified by the Function Variability (e.g., Var: 99 %) that is calculated as the ratio of the difference between the maximum and minimum value of the function relative to the maximum value of the function. The stability of the obtained result can be further assessed by the symmetry of the regression curve, which is expressed by the range of rotation angles for a variability of 5% of the misfit function above its minimal value. A large Function Variability and a good symmetry of the regression curve indicate the stability of the stress result around the tested stress axis.

Station	Geographic Coordinate System: WGS 1984		
	Longitude	Latitude	
COR002	-64,960397	-31,760340	Achala Granite
COR011	-64,911135	-31,779837	
COR012	-65,053546	-31,698531	
COR063	-64,945399	-31,641780	
COR064	-64,944931	-31,634675	
COR065	-64,944795	-31,632749	
COR066	-64,936305	-31,614301	
COR079	-65,015049	-31,828147	
COR082	-65,022794	-31,817248	
COR083	-65,017083	-31,824482	
COR084	-65,017214	-31,824172	
COR085	-65,015180	-31,827718	
COR116	-64,721968	-31,611799	
COR028	-65,391283	-31,374674	Los Túneles mylonitic gneiss
COR030	-65,399700	-31,379493	
COR031	-65,403180	-31,376518	
COR032	-65,403032	-31,376845	
COR042	-65,407105	-31,374366	
COR043	-65,407333	-31,374526	
COR047	-65,406898	-31,372860	
COR023	-65,426969	-31,358338	La Mermela phyllites
COR024	-65,418260	-31,360265	
COR025	-65,414013	-31,365476	
COR026	-65,418046	-31,365227	
COR027	-65,425292	-31,356803	
COR091	-65,423971	-31,356803	
COR092	-65,421437	-31,354519	
COR093	-65,419438	-31,356768	
COR095	-65,417796	-31,357803	
COR096	-65,417689	-31,358659	
COR097	-65,421615	-31,359480	
COR099	-65,418153	-31,364192	
COR060	-64,935249	-32,373793	Tres Arbores Fault Zone
COR120	-64,948557	-32,362173	
COR121	-64,945028	-32,363367	
COR122	-64,941199	-32,365900	

***Table A.1**: Geographic coordinates for all the measurement stations.*

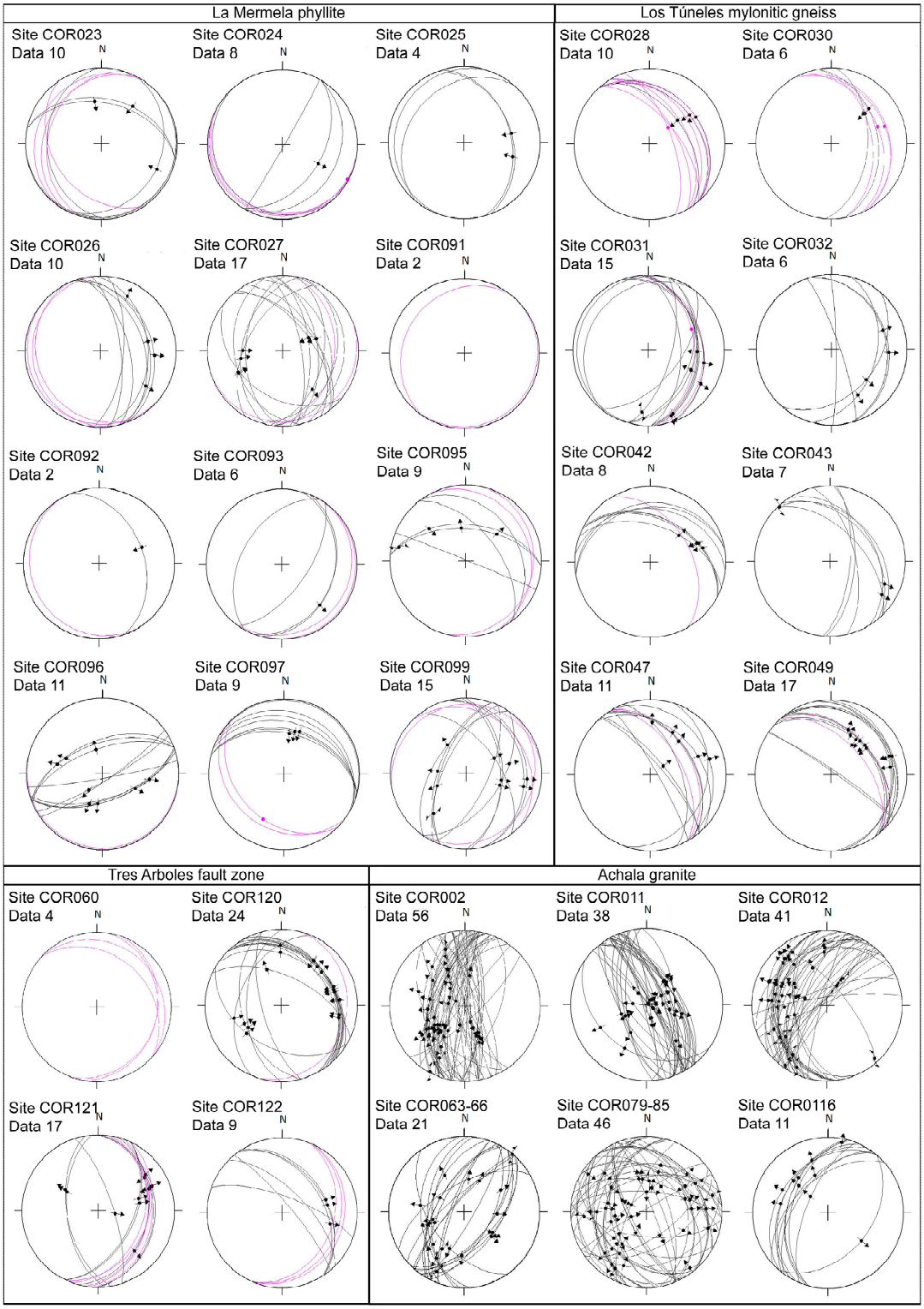

Figure A.1: *Raw fault-slip data from each investigated site. Faults and associated secondary Riedel (R and R') and tension (T) fractures in black, metamorphic foliation in purple.*

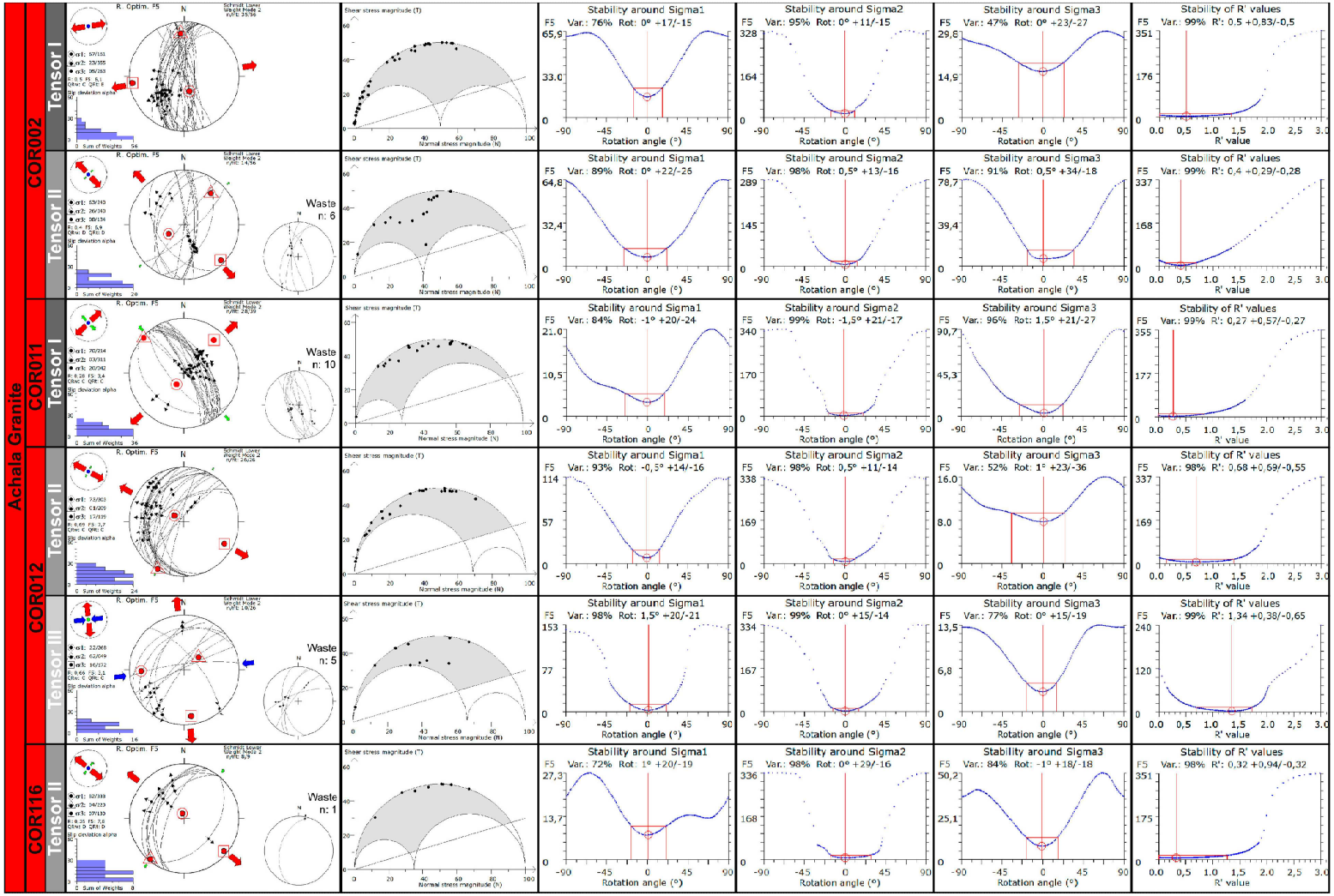

Figure A.2: *Table of the graphic outputs of the stress inversion procedure for the datasets measured at sites COR002, COR011, COR012 and COR116 in the Achala granite.*

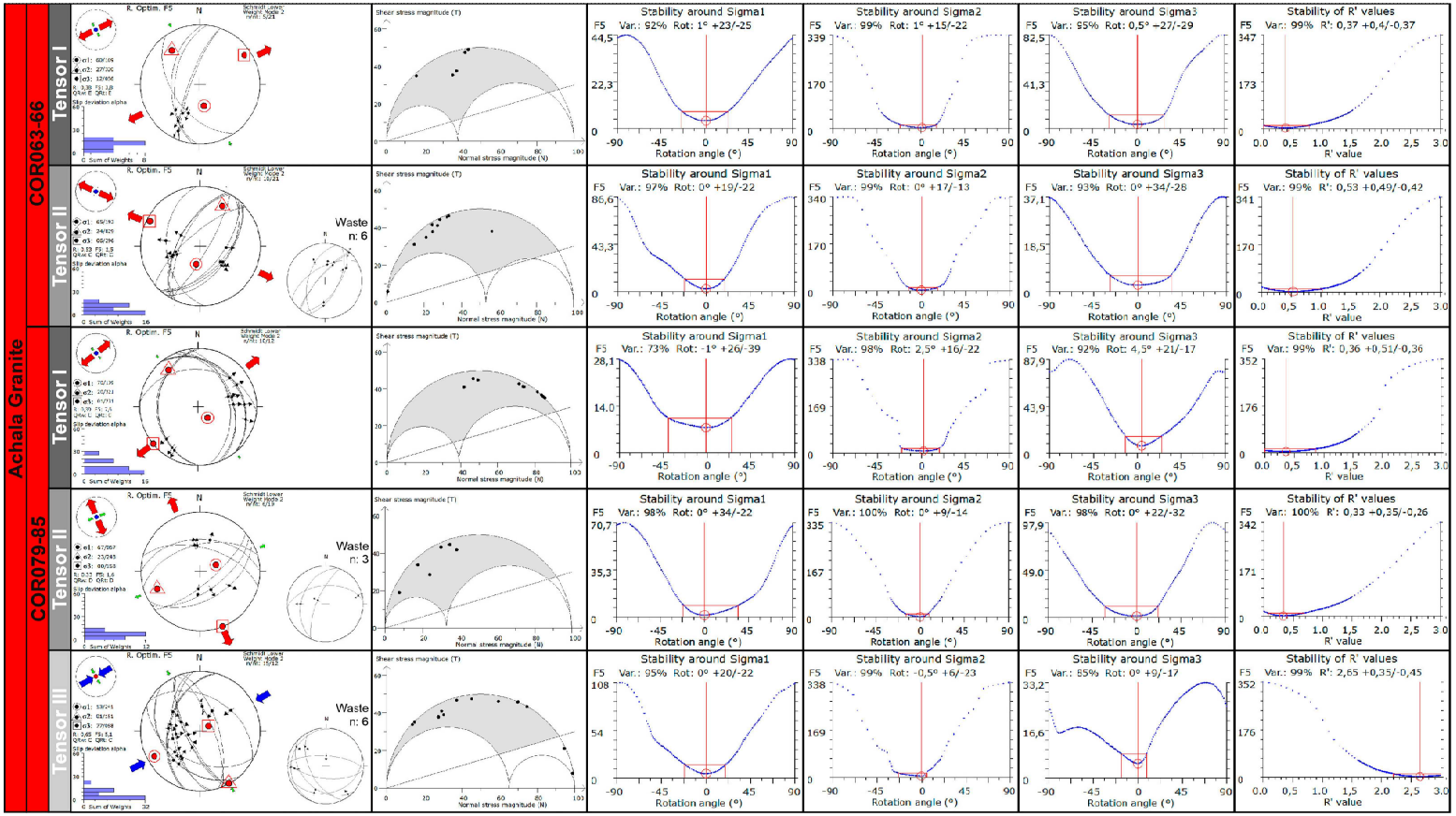

Figure A.3: *Table of the graphic outputs of the stress inversion procedure for the datasets measured at sites COR063-66 and COR079-85 in the Achala granite.*

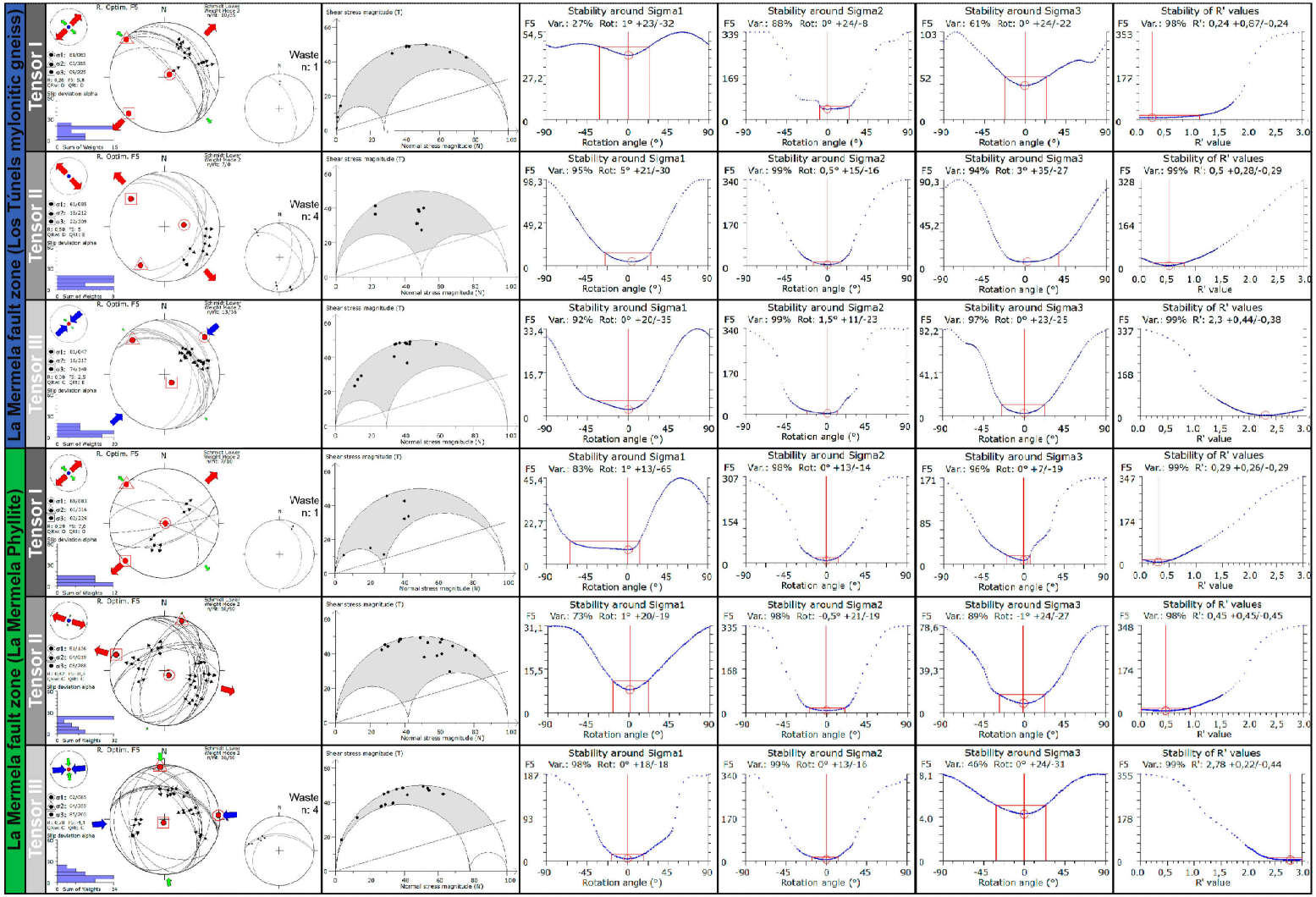

Figure A.4: *Table of the graphic outputs of the stress inversion procedure for merged datasets for the hanging wall and footwall of the La Mermela fult zone (i.e., Los Túneles mylonitic gneiss and La Mermela phyllite, respectively).*

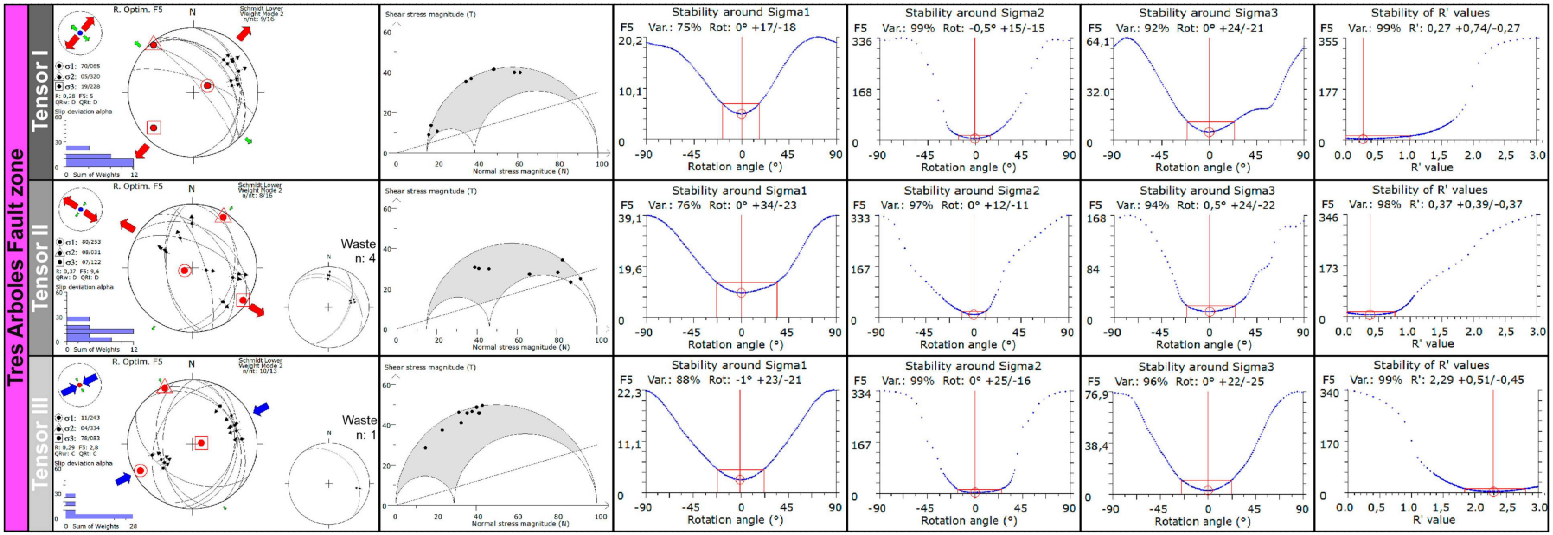

Figure A.5: *Table of the graphic outputs of the stress inversion procedure for the merged dataset of the hanging wall of the Tres Arboles fault zone.*

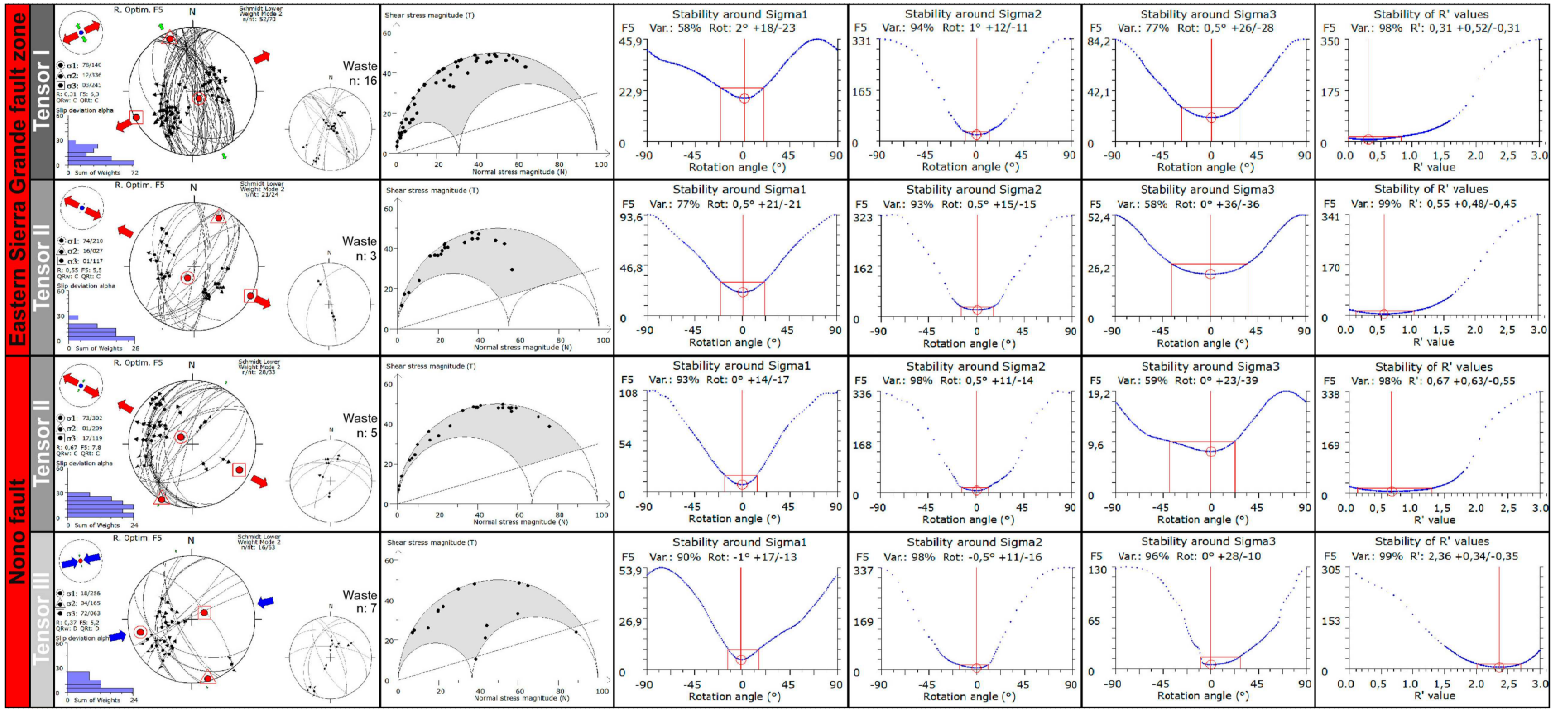

Figure A.6: *Table of the graphic outputs of the stress inversion procedure for the merged datasets from the Achala granite.*

Appendix B. Estimate of phyllosilicate content and interconnectivity

The amount of phyllosilicates for the La Mermela phyllite and the Los Túneles mylonitic gneiss was estimated by applying image analysis techniques on Back Scattered-Scanning Electron Microscope images (BS-SEM), considering representative portions of thin sections of the studied rocks (cut perpendicular to foliation and parallel to stretching lineation). The images have been processed with a low-pass digital filter (kernel size 3x3) using ENVI software, in order to eliminate noise and small patches related to grain boundaries. The different minerals were classified based on their grey scale tones (i.e., density slice tool) and the relative amount of phyllosilicates was calculated as area proportion in pixels (*Figure 3.6*). In order to corroborate the image analysis results, we performed a semi-quantitative X Ray Power Diffraction analysis (XRPD - Rietveld method) on samples COR100 (La Mermela phyllite) and COR042A (Los Túneles mylonitic gneiss). The results are reported in *Table B.1* and expressed in weight percent.

Assuming that the area percent is directly related to volume percent (Petruk 1989), volume percent can be calculated by dividing the weight percent by the mineral specific gravity and normalizing the results (Knight et al, 2002). As a result, the proportional amounts of phyllosilicates retrieved from XRPD (*Table B.1*) and image analysis (*Figure 3.6*) appear to be in agreement for both phyllite and gneiss samples (COR100 and COR042A respectively).

	Quartz (Wt%)	Albite (Wt%)	Oligoclase (Wt%)	Dolomite (Wt%)	Rutile (Wt%)	Goethite (Wt%)	Muscovite (Wt%)	Biotite (Wt%)	Chlorite (Wt%)	Total phyllosilicates (Volume %)
COR100 (phyllites)	34,7	24,8	/	2,7	0,4	/	19,1	2,5	15,8	37,06
COR042A (gneisses)	41,9	/	13,7	/	/	0,8	35,5	7,9	0,2	42,77

Table B.1: *Results of semi-quantitative X ray power diffraction analysis (Rietveld method) on samples COR100 (La Mermela phyllite) and COR042A (Los Túneles mylonitic gneiss). Total phyllosilicate amount (Volume %) calculated as specified in the text.*